Tunable Diode Laser Absorption Spectroscopy of Dusty Plasmas

inaugural dissertation
in fulfilment of the academic grade
doctor rerum naturalium (Dr. rer. nat.)
at the Faculty of Mathematics and Natural Sciences
of Ernst Moritz Arndt University Greifswald

presented by: Hoang Tung Do
born on 27. January 1979
in Thanh Hoa, Vietnam

Greifswald, January 2008

Dean: .....

1. Reviewer: .....

2. Reviewer: .....

Date of defence: .....

Preface

The interest in plasma-particle interactions in dusty plasmas has grown enormously during the last decade. At present, the interest is mainly caused by applied research related to materials science and more recently also with regard to plasma diagnostics. Powder formation has been a critical concern for the microelectronics industry, because dust contamination can severely reduce the yield and performance of fabricated devices. Submicron particles deposited on the surface of process wafers can obscure device regions, cause voids and dislocations, and reduce the adhesion of thin films.

Nowadays, dust particles are not only considered as unwanted pollutants. Positive aspects of dusty plasmas have emerged, and they even turned into production goods. Powders produced by plasma technology have interesting and potentially useful properties, e.g., very small sizes (nanometer to micrometer range), uniform size distribution, and chemical activity. Size, structure, and composition can be tailored to the specific requirements dependent on the desired application. There are several links between dusty plasma physics and materials science. The trend is similar to the well-established plasma surface modification technology, except that now the surface of dust particles is the subject of treatment. In these types of processing, particles are either grown in the plasma or are externally injected for subsequent treatment. In particular, the increased knowledge and ability to control particles in a plasma environment has recently led to new lines of technological research, namely, the tailoring of particles with desired specific surface properties.

Energetic metastables are species involved in the plasma and particle surface modification process. So far, role and effects of metastables in dusty plasmas are not considered in a large extent. There exists a lack in consideration of theses

species in such plasma environment.

Metastable atoms A_m are excited states, which are mainly electron impact formed by excitation of ground state atoms A_g:

$$A_g + e^- \rightarrow A_m + e^-$$

They are called metastable, because, metastable states are not optically coupled to any lower state. The only possible ways for them to disappear are diffusion out of the discharge, and collisions with electrons or other particles. An electron colliding with a ground state argon atom needs to have an energy of at least 11.55 eV (for Ar atom) or 16.62 eV (for Ne atom) to excite it to a metastable state. This energy is relatively high for electrons in rf discharges which have typical kinetic energies around 2 – 3 eV. The number of metastable states is therefore a measure for the number of electrons with such a high energy.

The lifetime of metastable states is much longer than that of resonant states. They therefore collide more frequently with other particles. This particular fact hence makes them important for plasma chemistry and surface modification: the high internal energy they carry with them can be given to other particles in collision enable them to involve in the wanted reaction. The energy of metastable atoms can be also transferred to surfaces to modify their properties.

Once dust is injected in a discharge it collects electrons and the number of free electrons in the discharge becomes smaller. Let us assume that the total power dissipated in a discharge does not change under the influence of dust, which means that the total energy of the electrons remains unchanged. The mean energy per electron in a discharge containing dust is, therefore, higher than in a discharge without dust. Or in other word, the electron temperature increases with the presence of dust particles. The electrons are more likely to excite or ionize atoms and molecules. The excitation to a metastable state, which requires a relatively high electron energy, therefore happens more often in this dusty discharge: the density of metastables hence can increase with the presence of dust.

Tunable diode laser absorption spectroscopy (TDLAS) can support the optimization of industrial plasma processes by permitting highly specific, accurate, and

non-intrusive real-time monitoring of species densities. TDLAS offers significant advantages over conventional spectroscopy. The spectral width of the laser radiation (a few MHz) is much smaller than the width (a few GHz) of the Doppler-broadened absorption profile. Sensitivity and signal to noise ratio are also increased in a TDLAS system because of the use of a high-power coherent source. This improvement in sensitivity provides TDLAS the ability to detect and measure atom temperature and low concentrations.

As mentioned above, a possible way for metastables to disappear is collision with a photon, which carries enough energy to excite it to a resonant state:

$$A_m + h\nu \rightarrow A^*$$

This process can be used to measure the density of the metastables, by means of absorption spectroscopy.

In this work, the investigation of dusty plasma making usage of tunable diode laser spectroscopy (TDLAS) will be described. The study is divided into three main parts; test of the possibility of TDLAS method in measure of plasma species density and temperature, characterization of the plasma, and investigation of the interaction between metastable atoms and dust particles.

The study was managed in the way from easy to difficult. Firstly, the tested target is the Al atom sputtered in Magnetron discharge. We measured the Al density in such system with respect to spatial distribution and plasma condition e.g., pressure, power and gas composition to confirm the possibility of applying this method in the dusty plasma.

Secondly, the plasma was characterized in terms of:

- Dust formation by laser transmitted and scattering methods
- Ion energy distribution function by plasma process monitor
- Mass spectrum evolution by plasma process monitor
- Spatial distribution of metastable atom by TDLAS

And finally, the interaction between metastable atoms with both injected and grown dust particle will be studied using TDLAS which focus on:

- Time evolution of metastable density in a dust forming plasma
- Loss of metastable to dust surface
- Indirect density enhancement of metastable density through the influence of dust particles on the electron temperature.

Symbols

A_g	ground state atom
A_m	metastable atom
A^*	excited atom
b_c	collection impact parameter
$b_{\pi/2}$	impact parameter with the asymptotic orbit angle of $\pi/2$
B	transition probability
D_m	diffusion coefficient
ΔT_n	temperature gradient of neutral gas
Δ_k	line width of spontaneous transition
$\triangle\nu_{1/e}$	full 1/e width
$\Delta\nu_D$	full width at half maximum
E	electric field strength
E_{diss}	dissociation energy
E_{excit}	excitation energy
E_G	gap energy
E_i	ionization energy
E_{kin}	kinetic energy
e^-	electron
ε_0	dielectric permittivity
F_{fr}	neutral drag force
F_{el}	electrostatic force
F_g	gravitational force
f_{ik}	optical oscillator strength of investigated transition
F_{ion}	ion drag force

F_{ion}^{c}	collective force
F_{ion}^{o}	orbit force
F_{th}	thermophoretic force
g	gravitational constant
g_i	statistical weight of lower level
g_k	statistical weight of higher level
$\mathbf{H}$	Havnes parameter
I	transmitted intensity
I_0	incident intensity
$I_a(i)$	absorbed currents by charged particle
$I_e(j)$	emitted currents by charged particle
I_{thr}	threshold current
j_{thr}	threshold current density
k	Boltzmann constant
k_m	rate coefficient for electron impact excitation from ground state to metastable state
κ_z	absorption coefficient
l	absorption length
l_D	diffusion length to dust particle
l_{eff}	diffusion length to chamber wall
l_{sh}	sheath length
λ_0	central wavelength of investigated transition
λ_{D}	Debye length
λ_{Di}	ion Debye length
λ_{mfp}	collisional mean free path between neutral gas atoms and either electrons or ions
Λ	Coulomb logarithm
m_a	atomic mass of interested atom
m_e	electron mass
m_i	ion mass
n_a	density of interested atom
n_d	dust density
n_e	electron density

n_g	background gas density
n_i	ion density
n_m	metastable atom density
n_m^D	metastable density with the presence of dust particles
n_M	density of considered molecule ion
P_m	power per unit area absorbed by dust particles due to the collision of metastable atoms with dust particle surface
P_M	magnetron power
ϕ_p	local plasma potential
ϕ_s	particle surface potential
$\phi(\nu)$	absorption profile
Q	particle charge
r	radius of dust particle
R_c	radius of dust cloud
$\dot{R}_{Al}$	production rate of aluminium atoms
$\dot{R}_+$	rate of argon ions hitting the target
ρ_p	density of the particle material
S_d	particle surface area
σ	cross-section constant
σ_{at}	gas kinetic cross-section for atomic scattering
σ_{n-d}	cross-section of the interaction between neutral and dust particle
T	kinetic temperature
T_e	electron temperature
T_i	ion temperature
T_p	growth period of one dust generation
T_{period}	period length
T_{pulse}	pulse length
T_{trans}	time the plasma needs to reach the $\alpha - \gamma'$ transition
T_{void}	time from the begin of one dust growth to the appearance of dust void
τ_{ab}	optical depth

υ_0	directional velocity
υ_i	mean ion speed
υ_R	relative particle-neutral velocity
υ_{Ti}	mean thermal velocity of ion
W_{FV}	Fermi level of p semiconductor
W_{FC}	Fermi level of n semiconductor
ω_{pi}	ion plasma frequency for a singly charged ion
Y	sputtering yield
Z	charge number on the dust particle

Contents

Chapter 1

Dusty plasma

1.1 Introduction

First scientific studies of electrical discharges were done by *H. Davy* and *M. Faraday* at the beginning of 19^{th} century. However, the term *plasma* was first introduced by *L. Tonks* and *I. Langmuir* in 1929 [1].

Plasmas are often considered as the fourth state of matter. In thermal equilibrium, a substance generally passes from solid state to liquid state by increasing the temperature and subsequently into gas as the temperature increases further. At a sufficiently high temperature, the substance transforms into plasma state where the atoms decompose into freely moving charged particles (electrons and positive ions) (fig. 1.1a).

This state is characterized by a common charged particle density $n_e \approx n_i = n$ where n_e and n_i denote electron and ion densities, respectively and kinetic temperatures $T_e \neq T_i(T)$ which is derived from relation:

$$kT = \frac{1}{2} m v_{\text{p}}^2 \tag{1.1}$$

where T is kinetic temperature, k is Boltzmann constant, m and v_{p} denote mass and the most probable velocity of the particle. According to the equation (1.1), 1 eV is equivalent to 11 604 K. The degree Kelvin (K) is an inconveniently small unit for kinetic temperatures in plasmas. One usually expresses the kinetic

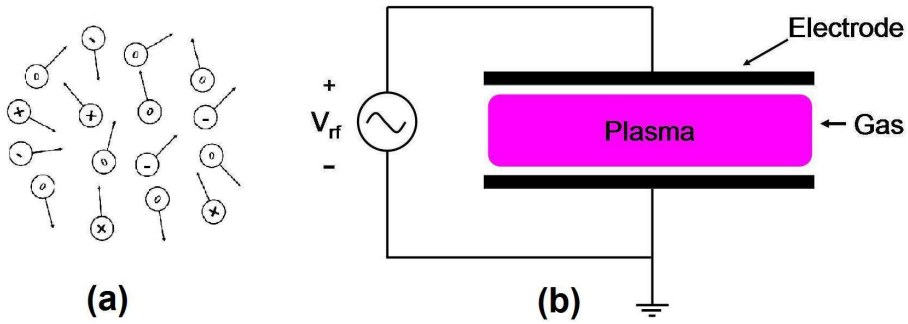

Figure 1.1: Schematic view of (a) a plasma and (b) a discharge.

temperature in electronvolt unit (eV).

Using electrical power is one practical method among many other ways to provide energy for atoms to decompose in order to create a plasma. The electrical discharge consists of a voltage source driving current through a low-pressure gas between two parallel conducting electrodes (fig. 1.1b). The plasma is formed when the gas "breaks down". The discharge is mainly sustained by charged particles, despite the fact that n_i, n_e may be several orders of magnitude lower than the background gas density n_g. The absorbed power is mostly carried by mobile electrons. The ions are heavy and exchange energy in collisions with the background gas. Therefore $T_e \gg T_i$ and the electrons play the central role in ionizing, exciting and dissociating gas to generate the positive ions, excited species, the free radicals, etchant atoms, and deposition precursors.

Dissociation, excitation and ionization occur in plasma, despite the fact that T_e is less than the dissociation energy E_{diss}, the excitation energy E_{excit} and ionization energy E_i of the gas atoms and molecules because electrons have an energy distribution. If $g_e(E)dE$ is the number of electrons per unit volume with energies lying between E and $E + dE$, $g_e(E)$ (see fig. 1.2) is then the energy distribution function of electron. Electrons having energies below E_{diss}, E_{excit} or E_i cannot dissociate, excite or ionize the gas. The dissociation, excitation and ionization are produced by the high-energy tail of the distribution.

In a real plasma the energy distribution of electron may not be Maxwellian.

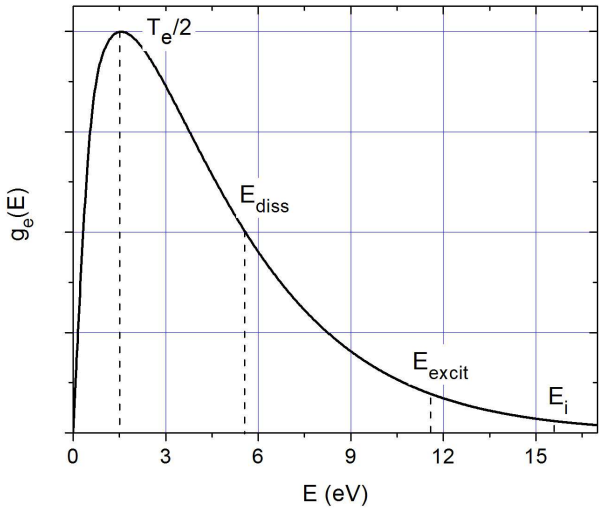

Figure 1.2: Energy distribution function of electron with $T_e = 3$ eV. Dissociation energy of acetylene is taken from [2], and ionization as well as excitation ($1s_5$ level) energies of argon from [3]

The tail distribution might be depressed by electron-neutral collision processes or enhanced by electron heating. A two temperature distribution is sometimes observed, especially for RF discharges, with T_e for the bulk electrons lower than T_h for the energetic electron tail.

Chen defined plasma also as quasi-neutral gas of charged and neutral particles which exhibits collective behavior [4]. In a plasma each charge carrier polarizes its surrounding and thereby reduces the interaction length of Coulomb potential. Ability to screen electric potentials, which are put in plasma, is one of the most important fundamental property of plasma behavior. The characteristic scale of screening or the width of the space charge sheath is determined by so-called Debye length λ_D [5, 6]

$$\lambda_\mathrm{D} = \sqrt{\frac{\varepsilon_0 k T_\mathrm{e}}{n e^2}} \tag{1.2}$$

where ε_0 is dielectric permittivity in vacuum, e is the electron charge. Therefore,

the plasma quasi-neutrality means that *the plasma is quasi-neutral over scale lengths much larger than the Debye length* where one can assume $n_e \approx n_i = n$.

The particles in plasma can be in different quantum states - can be excited or de-excited to and from various energy levels. During these processes photons and subsequently light are produced. Collective behavior means that not only local properties but also plasma conditions in remote regions influence plasma particles.

Dust particles in plasmas were first discovered by *Langmuir* in 1924 [7]. In the last years, the field of complex dust containing so-called dusty plasmas has been rapidly evolving both in cosmic [8 – 12] and in laboratory plasmas [6, 13 – 16] since its rediscovery in plasma processing [14, 17].

The occurrence and role of the charge dust particles in the interstellar space, planetary atmospheres, ring structure, cometary tail, etc. has been intensively investigated in the last decades. *Gould* and coworkers has pointed out that charge grains are important parts in the synthesis processes of molecular species in diffuse nebulae and directly participate in various astrophysical processes [18]. There are also many reports about the complex plasma systems in space environments as in planetary atmospheres and planetary rings [11, 19, 20].

In laboratory conditions, such as colloidal suspensions, charged aerosols, high-pressure ionized gas systems, nucleation catalysts, and many others, fine particles take also an important role. The nano and micrometer particulate powders have been detected in a number of experiments with low-temperature plasma for material synthesis and processing applications. Especially, dust is very common in radio-frequency gas discharges, where fine powders appear in the mixture of chemically active (reactive) gases that generate electronegative radicals [21].

1.2 Particle charging and confinement

1.2.1 Particle charging

One of the most fundamental aspects of dusty plasma is the charging process of the dust particles. Electron and ion bombardments are the usual ways for dust charging in laboratory dusty plasmas. When a dust particle is injected in a plasma it gathers electrons and ions on its surface and becomes negatively charged due to the high mobility of electrons. The steady state charge of dust particles in a plasma depends on whether the dust grains can be considered as being isolated or not. A single grain is isolated. However when more and more particles become immersed in a plasma, the proximity of one particle to another affects the charge on the particles. This is known as the close-packing effect which becomes important when the inter-particle spacing becomes comparable to the plasma Debye length e.g. $\lambda_D \sqrt[3]{n_d} \sim 1$ where n_d is the dust density.

The close-packing effect can also be formulated in terms of the so-called Havnes parameter $\mathbf{H} = Zn_d/n_i$, where Z is the charge number on the dust and n_i is the ion density. Generally, the grains cannot be considered as isolated and the close packing effect must be taken into account if $\mathbf{H} \sim 1$. With relatively high grain density, the charge portion on dust grains has to be taken into consideration in the quasi neutrality relation.

The charging process of dust particles in a plasma is governed by the contribution of all currents enter and leaving the particle surface:

$$\frac{dQ}{dt} = \sum_i I_a(i) + \sum_j I_e(j) \tag{1.3}$$

where Q denotes the particle charge, $I_a(i)$ and $I_e(j)$ are the absorbed and emitted currents by charged particle, respectively. In the stationary state when $dQ/dt = 0$, all the currents are in balance $\sum_i I_a(i) = -\sum_j I_e(j)$ one obtains the equilibrium value of dust charge.

The particle charges to a potential ϕ_s (the grain surface potential); under typical conditions (electron/ion plasma, no photoelectric charging), ϕ_s will be nega-

tive. According to the widely accepted Orbital Motion Limited (OML) approach [19, 22, 23], for Maxwellian electrons and ions with temperature T_e and T_i, respectively, the orbit-limited charging currents for a spherical particle are given by [19]:

$$I_e = -4\pi r^2 e n_e \sqrt{\frac{kT_e}{2\pi m_e}} \exp\left(e\phi_s/kT_e\right) \tag{1.4}$$

$$I_i = 4\pi r^2 e n_i \sqrt{\frac{kT_i}{2\pi m_i}} (1 - e\phi_s/kT_i) \tag{1.5}$$

where r denotes the radius of the dust grain, m_e and m_i are the electron and ion masses. The OML approach is valid when $r \ll \lambda_{Di} \ll \lambda_{mfp}$ where λ_{Di} is the ion Debye length, and λ_{mfp} is the collisional mean free path between neutral gas atoms and either electrons or ions [23].

The surface potential is determined at the floating condition where these two currents are equal:

$$n_e \sqrt{\frac{T_e}{T_i}} \sqrt{\frac{m_i}{m_e}} \exp\left(e\phi_s/kT_e\right) + n_i(1 - e\phi_s/kT_i) = 0 \tag{1.6}$$

The particle charge Q is calculated from the surface potential of the dust grain using the relation of spherical-capacitor model for the dust particle where $Q = eZ = 4\pi\varepsilon_0 r\phi_s$. Therefore,

$$\exp\left(-Z_D\right) = \frac{(1 + \mathbf{H})\,(\tau + Z_D)}{\sqrt{\tau\mu}} \tag{1.7}$$

where $Z_D = (Ze^2)/(rT_e)$, $\tau = T_e/T_i$, and $\mu = m_i/m_e$

In an rf discharge, the dust density is often high enough to yield $\mathbf{H} \gg 1$. For example, for the representative parameters of the experiment of [24] ($n_i \sim 5 \cdot 10^9$ cm^3, $n_d \sim 10^8$ cm^{-3}, and $T_e \sim 2$ eV) the Havnes parameter appears to be approximately 3.2. Hence the particle charge deduced from equation (1.7) can be 60% smaller than the charge of an isolated dust particle under the same condition [23].

1.2.2 Forces acting on dust particle

The heaviest species in a dusty plasma, electrically charged dust grains which typically have a charge to mass ratio quite different from that of electrons and ions, experiences several forces. The overall effect of these forces either trap the particles in the discharge or expels them.

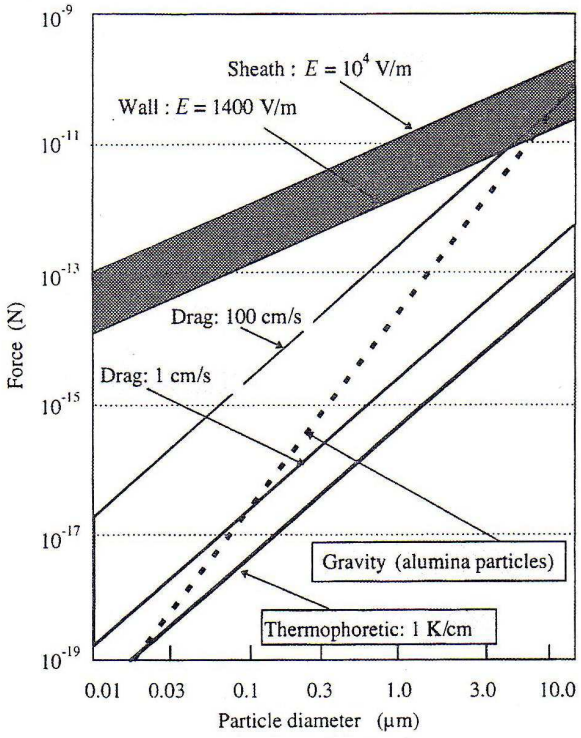

Figure 1.3: Scaling of forces acting on single alumina particle *versus* dust particle diameter with electric field in the range 1.4×10^3 – 10^4 V/m, relative velocities in the range 1 – 100 cm/s, pressure of 2 Pa, and thermal gradient of 1 K/cm [25].

In our case of low temperature rf dusty plasma with the particle radius ranges from some nanometers to few micrometers, two forces are essential for the trapping of the particles:

The **gravitational force** $F_g = \frac{4}{3}\pi r^3 \rho_p g$ where ρ_p denotes the density of the particle material, r its radius, and g the gravitational constant. The gravitational force is mainly important for large particles (> 0.1 μm see figure 1.3).

The **electrostatic force** $F_{el} = QE$, where Q is the effective charge of the negatively charged particle with its surrounding positive cloud (a so called *dressed particle*) and E the electric field strength.

The gravitational force tends to pull out the dust particles, while the electric force pushes these negatively charged particles inward. The balance of these two forces confines the dust particles inside the plasma.

Neutral and ion drag forces and the thermophoretic force are responsible for the losses of dust grains. Both drag forces are caused by differences in momentum transfers from plasma-species on either sides of the dust-particles. The thermophoretic force similarly is caused by temperature gradients in the discharge, which also cause differences in momentum transfers.

The **neutral drag force** or *friction force* results from the momentum transfer between neutral gas and particle which is proportional to the gas pressure. Considering this interaction to be hard sphere, elastic collisions, the neutral drag force is approximated by [26].

$$F_{fr} = n_g \upsilon_R^2 m_n \sigma_{n-d} \tag{1.8}$$

where n_g is the neutral gas density, υ_R is the relative particle-neutral velocity, and σ_{n-d} is the cross-section of the interaction which can be approximated to be πr^2.

The **thermophoretic force** F_{th} originates from the temperature gradient of the neutral gas ΔT_n from the electrode toward the plasma bulk. For a spherical particle F_{th} in a monoatomic gas at low pressure it is given by

$$F_{th} = -3.33(r^2/\sigma_{at})\Delta T_n \tag{1.9}$$

where it was assumed that the mean free path is much greater than the particle radius. σ_{at} is the gas kinetic cross-section for atomic scattering.

The force responsible for the existence of the dust void in the plasma bulk and the aligning of particles in the plasma sheath is the **ion drag force** F_{ion}. This force is caused by the momentum transfer from the positive ion current driven by

the electric field. The ion drag force consists of two components: the collective force F_{ion}^{c} and the orbit force F_{ion}^{o} [26]

$$F_{ion}^{c} = n_i \upsilon_i m_i \upsilon_0 \pi b_c^2 \tag{1.10}$$

where n_i and m_i are the ion density and mass, respectively, $\upsilon_i^2 = (\upsilon_0^2 + \upsilon_{Ti}^2)$ is the mean ion speed that includes the directional (in the electric field) υ_0 and the mean thermal velocity ($\upsilon_{Ti} = (8T_i/\pi m_i)^{1/2}$) components. The collection impact parameter b_c is given by:

$$b_c = r\left[1 - \frac{2e(\phi_p - \phi_s)}{m_i \upsilon_i^2}\right] \tag{1.11}$$

where ϕ_p and ϕ_s are the local plasma and surface potentials, respectively.

The orbit force is based on the OML probe theory and given by:

$$F_{ion}^{o} = 4\pi n_i \upsilon_i m_i \upsilon_0 b_{\pi/2}^2 \Lambda \tag{1.12}$$

where $b_{\pi/2} = eQ/m_i \upsilon_i^2$ is the impact parameter with the asymptotic orbit angle of $\pi/2$ and Λ is the Coulomb logarithm integrated over the interval from b_c to $b_{\pi/2}$.

$$\Lambda = \frac{1}{2} \ln\left(\frac{\lambda_{Di}^2 + b_{\pi/2}^2}{b_c^2 + b_{\pi/2}^2}\right)$$

The contribution of the orbit force is negligible when the collection impact parameter is greater than or equal to the ion Debye length.

The particles levitated in the plasma sheath is often observed aligning in the direction of the ion flow toward the electrode [27]. Theoretical studies suggest that the ion wake field is formed behind (with respect to the ion flow) the dust grain [28, 29]. As known both from numerical simulations and experimental observations [30, 31] the ions from plasma can excite longitudinal plasma oscillations in the sheath region due to their supersonic velocities achieving from the acceleration of the electric field in the presheath [32]. The attractive wake field force

between the particles in the plasma sheath scales with the characteristic length L_s:

$$L_s = \lambda_D \sqrt{M^2 - 1}$$

where $M = v_0/v_s$ is the March number of the ion flow, $v_s = \lambda_D \omega_{pi}$ is the ion sound speed, and $\omega_{pi} = (4\pi n_i e^2/m_i)^{1/2}$ is the ion plasma frequency for a singly charged ion.

The above forces acting on particles critically depend on the ion velocity, particle size and specific position within the discharge. The position of trapped particle is where the sum of these forces acting on the particle vanishes. The scaling of these forces depending on dust particle size is shown in figure (1.3). One can easily find out that micron-size particles are normally located in the plasma sheath where sufficiently strong electric field exists to compensate the gravitational force. Meanwhile for nano-size particles the latter force is negligible which allows the weak field in the plasma bulk to effectively confine the tiny grains.

1.3 Influence of particles on plasma parameters

Beside the electrodes, particles inside plasma serve as additional collecting surfaces of plasma species. Associating with the presence of dust particles in plasma is the significant decrease of electron density.

The complex plasma system itself tends to re-establishing the charge and particle distribution of pristine plasma by self-organization. The dusty plasma system, therefore, changes typically including the increase of electron temperature and consequently the increase of ionization, excitation, and dissociation rates, the ambipolar electric field and charge fluxes to the wall and dust surface. The presence of dust also influence density and temperature profiles of the plasma species, as well as discharge operation regimes and plasma instabilities.

As an example, the equilibrium electron temperature calculated in the capacitively coupled rf plasmas of hydrogen-diluted silane discharge is displayed in figure (1.4). In this calculation, electron temperature rises remarkably from 3.5 eV

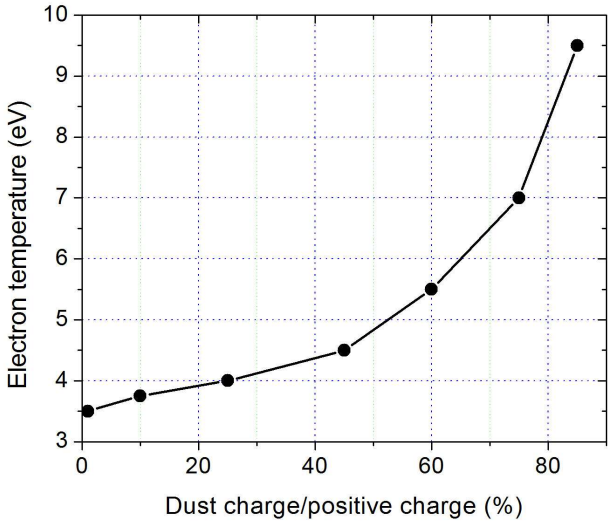

Figure 1.4: Electron temperature vs. dust charge portion (Havnes parameter) [33] for the representative parameters of experiment [34].

to almost 9.5 eV as the charge portion on dust particles increases.

As we shall see later, the metastable density decreases with the presence of dust particle as metastable atoms quench in collision with dust particles (see chapter (6)). However, the metastable density can also increase with the presence of dust particles in dusty plasma with high dust density (see chapter (7)). In this case, the increase of excitation rate exceeds loss rate by quenching resulting in a higher metastable density of dusty plasma comparing to that of pristine plasma.

In an rf pristine plasma, the electron temperature and other plasma parameters are mainly determined by the balance of volume ionization and electron losses on the walls. The electrons within the plasma gain energy from the oscillation of the plasma sheath. This type of plasma sustenance mode is called α or "wave riding" mode. However, in a dust dense plasma, the electron losses on the particle surfaces exceed that on the walls. The electron concentration decreases dramatically and the electron temperature increases to maintain the plasma balance. The sustenance mode in this type of plasma is called γ' mode [35].

1.4 Fine particles and applications

1.4.1 Growth of dust particle in processing plasma

In hydrocarbon containing plasmas a large amount of dust particles is effectively and continuously created and trapped inside the plasma. Dust particle size and density can reach significant values resulting in a recognizable decrease of transmitted laser light and a remarkable increase of scattered laser light [36]. A dust void is subsequently created in the center of the dust cloud under the action of the ion drag force [26] which becomes significant once the dust particle size and density reach critical values. Meanwhile a new dust generation forms in the free space. The new generation grows both in size and number density until it is also pushed out. The particles created in the plasma is mono-dispersed (figure (1.5)).

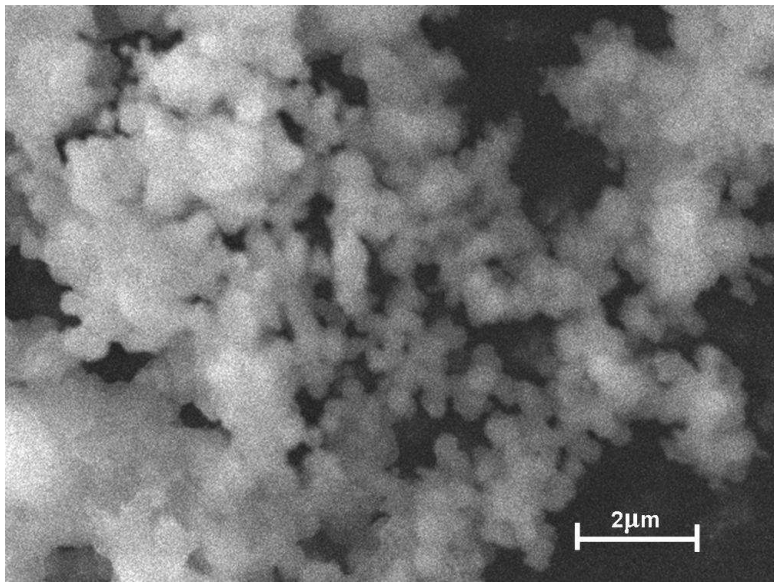

Figure 1.5: SEM picture of carbon particles grown in Ar/C_2H_2 rf plasma. The particles were collected on the chamber wall.

The growing process of a dust generation in a chemically reactive plasma can be divided into three steps [24, 37]: nucleation, agglomeration and accretion. In the nucleation phase the subnanometer/nanometer-sized protoparticles are formed as the result of homogeneous or heterogeneous processes. Later in the

agglomeration step, these protoparticulates after reaching a critical density merge together forming particles with the sizes of the few-tens of a nanometer. Particles of this size quickly acquire a negative electric charge by ion and electron collection which causes the plasma to reorganize. In order to compensate the electron losses, the effective electron temperature increases. This reorganization of the plasma is called a $\alpha - \gamma'$ transition [35]. After this transition the particles accrete neutral and ionic monomers to grow into larger particles until they become large enough to be driven away by the ion drag force. The accretion process is relatively slow, and no new particle is form in the accreting dust cloud. The time evolution of dust grown process therefore is parameterized by 3 characteristic times: T_{trans} - the time the plasma needs to reach the $\alpha - \gamma'$ transition, T_{void} - the time from the begin of one dust growth to the appearance of dust void, and T_p - the growth period of one dust generation (see figure (5.11)).

1.4.2 Applications of nano and micron-sized particles

Powder particles produced by plasma technology have numerous applications due to their many interesting and potentially useful properties [38], eg.,

- Small sizes
- Uniform size distribution, and
- Chemical activity.

As ultra-fine particles can be incorporated into polymetric/ceramic material, they are useful in material engineering, optoelectronic [38], optical, petrochemical, automotive, mineral, and other industries. The advanced nanostructured materials are used as, eg., water repellent, protective, fire resistant and functional coatings [39].

Due to its chemical property, fine powders of about 10 nm-sized particles have been widely used as catalysts for inorganic manufacturing, ultra-fine UV absorbing additive for sunscreens and other outdoor application. The fine particles are

also applicable in textiles, wear-resistant ceramics, inks, pigments, toners, cosmetics, advanced nanostructured and bioactive materials, environmental remediation [40] and pollution control, waste management, as well as various colloidal suspensions for mining, metallurgical, chemical, pharmaceutical industries, and food processing.

Nanoparticles (smaller than 100 nm) have many properties which differ from the bulk material and make them attractive for many new electronic, optical or magnetic applications including quantum dots, luminescent materials, gas sensors, resistors and varistors, conducting and capacitive films, high temperature superconductors, and thermoelectrical, optical, and magnetic materials [41].

Meanwhile, nanoparticles have recently emerged as valuable elements of several technologies aiming to tailor material properties at nano scales and manufacture novel nanoparticle-assembled materials with unique optical, thermal, catalytic, mechanical, structural and other properties and featuring nano-scale surface morphologies and architectures [42].

The useful properties of fine particle mentioned above can be tailored by plasma to specific applications with tools like:

- Magnetron discharges for metal coating [43, 44]
- Processing plasmas for amorphous carbon (a-C:H) films [45]
- Or using metal-organic gas precursor as alternative to sputter-coating process: Few years ago, *Kersten* and coworkers had used ATI ($Al(i\text{-}OC_3H_7)_3$) to deposit Al layer on fluorescent high brightness, high maintenance phosphors to improve their stability and adhesive properties [44]

Due to their special properties, one can make a long list of applications of plasma treated fine particles which includes at least;

- New classes of particle-seeded composite materials [38] using powder particle synthesis in plasmas, for example; embedding the nanometer-sized particle grown in silane discharges into an amorphous silicon matrix can substantially improve the performance of silicon solar cell.

- Improvement of thin film hardness by incorporation of nanocrystallites in hard coating [39]
- Soot and aerosols treatment for environmental remediation [40]
- Surface modification of toner particles [43]
- Enhancement of adhesive, mechanical and protective properties of powder particles for sintering processes in the metallurgy fragmentation of powder mixture in order to sort them [46]
- Coating of lubricant particles [47]
- Application of tailored particles for chemical catalysis
- Production of color pigments for paint industry
- Improvement of anti-corrosion properties of fluorescent particles [48]

In particular, dusty plasmas offer an unusual conditions for the processing of various surfaces and particle due to the highly efficient chemistry that can be achieved as a results of the enhancement of the electron energy [49]. The complex plasmas can be even more efficient as compared to electronegative gases in term of chemically reactive radical production and be suitable for various thin film technologies.

Chapter 2

Tunable diode laser

2.1 Operation and characteristics

Tunable diode laser are developed primarily for applications in precise measurements [50], sensing, in coherent communication systems, as well as in wavelength division multiplexing technology. Wavelength tunable lasers are very desirable for increasing the capacity, functionality, specialty, and flexibility of current and next generation all-optical devices and networks.

2.1.1 Operation principle

A diode laser is a semiconductor diode which emits laser radiation when it is correctly coupled to power source. In principle, the laser is just a simple p-n transition (figure (2.1)). The carrier transport in such a diode takes place primarily in the valence band of the p-doped part with holes and the conduction band of the n-doped part with electrons. The difference between the maximum energy in the valence band and the minimum energy in the conduction band is the gap energy E_G (figure (2.2)).

When p and n conductors are brought into contact, after a very short time (ps), the majority charge carriers diffuse across the junction and recombine instantly leaving the p-n junction region without charge carriers - the p-n transition region is then so-called the depletion zone. The charges on both sides of the depletion region generate an electric field across the region, this field opposes the diffusion

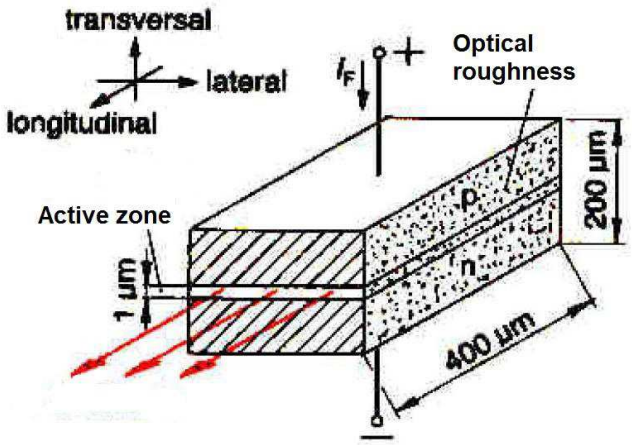

Figure 2.1: Homojunction laser diode.

of holes into the n region and of electrons into the p region. An energy barrier is produced and the Fermi level is lined up (figure (2.3 a)), the height of energy barrier is called barrier voltage.

If a voltage is applied to the junction such that the p part is positive and the n part is negative, the two Fermi levels become misaligned (see figure (2.3 b)). The majority carriers can drift from both sides into the barrier. The electrons from the conduction band of the n-part and holes from the valence band of the p-part inject into the transition where the migrant holes and electrons recombine. With an appropriate choice of semiconductor and appropriate doping one can achieve optical transitions, so that the energy E_G can be released in the form of a photon with frequency E_G/h. The line width Δ_k of this spontaneous transition is generally around 100 cm^{-1}, since the transition is not between two discrete levels but between two energy bands.

The diode laser is an almost ideal four step system: The pumping process takes place on the dumping of electrons in the conduction band on the edge of the active zone. They then switch during a time period of a few pico-seconds by the electron management process into the metastable level inside the conduction band in the active zone. The lifetime of this state is in order of nanoseconds. From there, they fall down into the valence band of the active zone emitting radiation. After

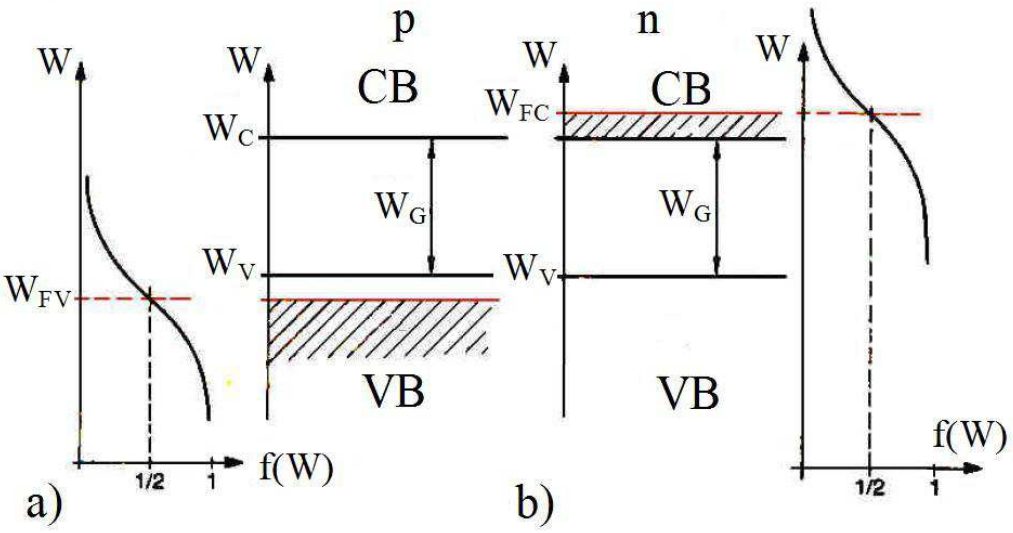

Figure 2.2: Degenerated semiconductors: a) p type and b) n type. The Fermi energy W_{FV} and W_{FC} are within the valance band or conduction band.

that they will be very quickly emptied by recombination process with holes.

The injections of electrons into the conduction band and holes into the valance band reduces the barrier voltage, and more carriers are able to cross the narrowed depletion region, many of electron-hole pairs combine radiatively and generate spontaneous emission. Therefore at an appropriate current density j_{thr} (threshold current density) the stimulated emission in the diode can prevail spontaneous emission and laser radiation is emitted in the active zone (perpendicular to the current direction).

In a diode laser, at relatively low energy input, already a high population inversion can be achieved. The output achievement over a wide area is linearly proportional to the current $I - I_{thr}$ (see figure (2.5)). The laser diode wavelength can range from the far infrared (60 μm) to the ultraviolet.

The mode distance of a laser, in which the crystal is used as a resonator, is about 10^{10} Hz due to the small longitudinal dimension of the semiconductor crystal ($\delta k \sim c/(2nL)$). Therefore single mode operation can easily be guaranteed. The small and asymmetric transverse dimensions of the active zone which lead to

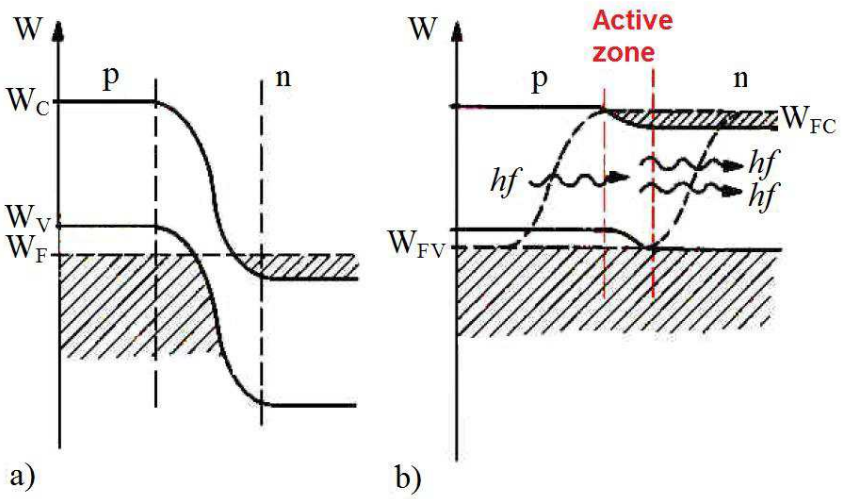

Figure 2.3: Energy band diagram of a p-n conjunction with a degenerate semiconductor: a) thermal equilibrium and b) polarity in the direction of flow.

an asymmetric and relatively high beam divergence, can be resolved with an appropriate collimator lens [51].

2.1.2 Polarization of the laser diode radiation

Light emitted by a laser above the threshold is linearly polarized. The polarization direction (E-vector) is parallel to the active zone (lateral), while the spontaneous radiation is unpolarized. Therefore the degree of polarization increases with increasing radiation power of the laser diode.

2.1.3 Beam quality

Because of the small emitting area (lateral: 6 μm $< d_{\parallel} <$ 100 μm) and transversal: 0.15 μm $< d_{\perp} <$ 1 μm), as a result the diffraction aperture angle is expected to be large (figure (2.4)). The half-widths of the divergence angle $\Theta_{\parallel}$ and $\Theta_{\perp}$-depending on the type of laser diode can reach up to 20° and 60°. The radiated wave is not a spherical wave. The curvature centers $M_{\perp}$ and $M_{\parallel}$ the wave fronts

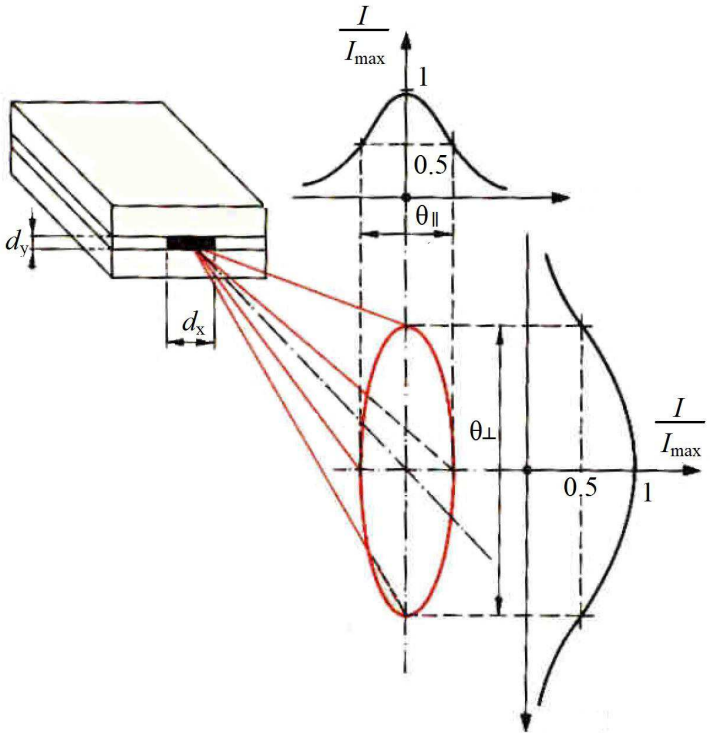

Figure 2.4: Beam divergence perpendicular and parallel to the level of active zone.

are not perpendicular and parallel to the active zone. $M_{\perp}$ lies in the exit area of the laser diode. In the plane parallel to the active zone of the curvature center $M_{\parallel}$ is about 5 μm and up to 50 μm behind the mirror level. These different curvatures in two vertical planes are called astigmatism. A cylindrical lens is used in order to correct this problem. The index guided laser diodes emit a basic mode. Due to the different divergence, the power density distributions are Gaussianly in the two planes distributed. These different divergences may be eliminated with a pair of anamorphic prisms

2.2 Structure and effectiveness

As mentioned above, an electron in the conduction band can recombine with a hole in the valence band. Released energy from the recombination process can be emitted as a photon. This radiant recombination process occurs essentially

only in the so-called direct semiconductors, including GaAs. These recombination processes without the aid of another particle fulfil the energy and momentum conservations. Ge and Si are among the indirect semiconductors, where the recombination energy is transmitted as thermal energy in the crystal lattice. These materials are inappropriate for light emitted diodes (LED) and laser diode (LD).

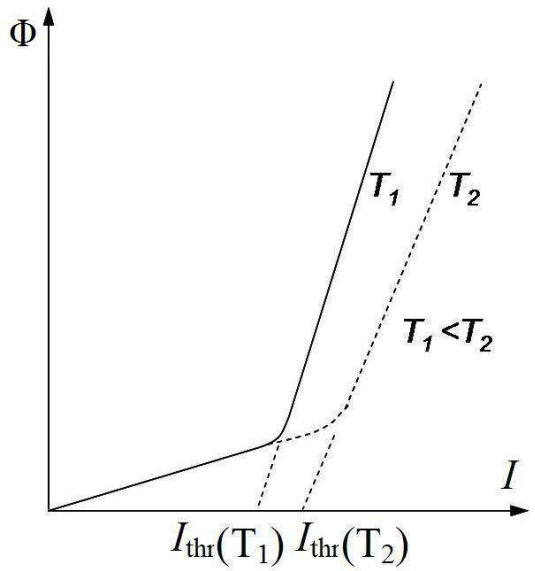

Figure 2.5: Output power as a function of current and temperature.

The population inversion of a laser diode can be achieved in the so-called degenerate semiconductors. Here the dopings are so high (the acceptor density or donator density $> 10^{18}$ cm^{-3}) that the Fermi level range within an allowance band e. g. the Fermi level W_{FV} in the degenerate p-side moves into the valence band and the Fermi level W_{FC} in a high n-doping side moves into the conduction band (see figure (2.2)).

The figures (2.1), (2.2) and (2.3) show the building principle of a homojunction diode laser (two sides of the diode made from the same semiconductors - GaAs in this case). The active zone is the inversion zone. The two ends of the crystal are cleaved to form perfectly smooth, parallel edges, forming a Fabry-Perot resonator. The refractive index of GaAs is 3.6. Compared with an optical medium (air) with n = l.0 it is sufficient to form a resonator without extra mirror. By applying a threshold current I_{thr}, (pumping threshold) the diode changes from an incoherent

radiator (equivalent to luminescence diode LED) to a coherent one (laser diode LD). It is found that for lasing the densities of the electrons and holes in the conduction band and valence band, respectively, must be significantly greater than 10^{-18} cm^{-3}. The threshold current density j_{thr} is therefore very high (about 1000 A/mm^2 at room temperature) for this type of semiconductor laser. It is impossible for a continuous operation at room temperature. The threshold current increases with the temperature and is an indication of the losses. The threshold current density is high in the homojunction diode laser due to two losses:

- Part of charge carriers injected into the active zone arrived as minority carriers in the other area. The spatial dimensions are smallers than the diffusion lengths L. For GaAs diodes, L is about three times the thickness of the active zone.
- The resonator is in lateral direction. In transversal direction there is only small refractive index step, so that total reflection only weakly dominate the optical waveguide.

The heterojunction was used in order to eliminate these losses. Each of the junctions between different bandgap materials is called a heterostructure, hence the name "double heterostructure laser" or DH laser is for the diode laser which is made by adjacent semiconductor crystals with different band gaps. For example, using the mixing crystal $Ga_{1-x}Al_xAs$ (see figure (2.6)) with a larger band gap than GaAs gives the first successful continuous working diode laser at room temperature [52]. Since the refractive index decreases with increase band gap, in the heterostructure, a refractive index jump occurs provide a better carrier confinement and optical field to prevent the inversion creation charges to diffuse from the active zone into the adjacent area as minority carriers with a potential barrier. All injected charge carriers in the active zone must then recombine. The recombination radiation is high enough to trigger stimulated emission. Following the reflective index the light wave is totally reflected in transversal direction as in a waveguide. The light wave penetrates very little into the adjacent p and n areas. In lateral direction the light wave is limited by the gain profile within the active zone, ie by the power distribution of injected charge carriers. Thus, for

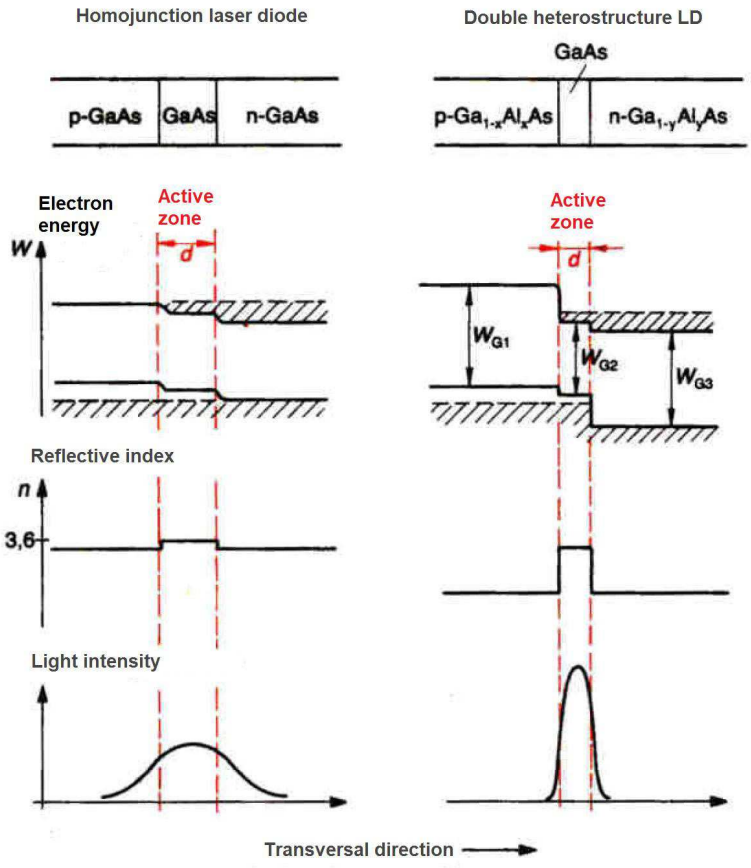

Figure 2.6: Comparison of Homojunction and Doublehetero structure in relation to the band characteristic, the refractive index n and the light intensity in the active zone.

example through oxide strip, the distribution of electricity in the active zone can be controlled. The fiber is then gain-controlled in lateral direction. If the active zone is surrounded by GaAlAs layers both in transverse and lateral directions, then the light wave is confined in both directions by a refractive index jump. The threshold current density can be practically reduced to values of $j_{thr} = 5$ A/mm^2.

For each recombination process an electron must be injected. The internal quantum efficiency is the ratio of the number of photons per unit of time generated by the number of electrons injected per unit of time. It may reach up to almost 100%. Losses occur as not all created photons reach the outside world. Important

for the application of laser diodes is the differential efficiency. It is the ratio of increase in radiation optical performance and increase of pumping capacity above the lasing threshold. This efficiency can be up to 45% per mirror surface.

2.3 Tuning and mode structure

A light source with a frequency of interest that can be adjusted continuously is required in order to cover the vicinity to a resonance of an atomic spectrum. This source is called a tunable light source. The wavelength of a tunable diode laser is tuned by varying the temperature of the active region. The active zone temperature is adjusted by:

- Variation of the temperature of the cold stage on which the diode is mounted
- Variation of the laser drive current, which varies the Ohmic heating of the active region.

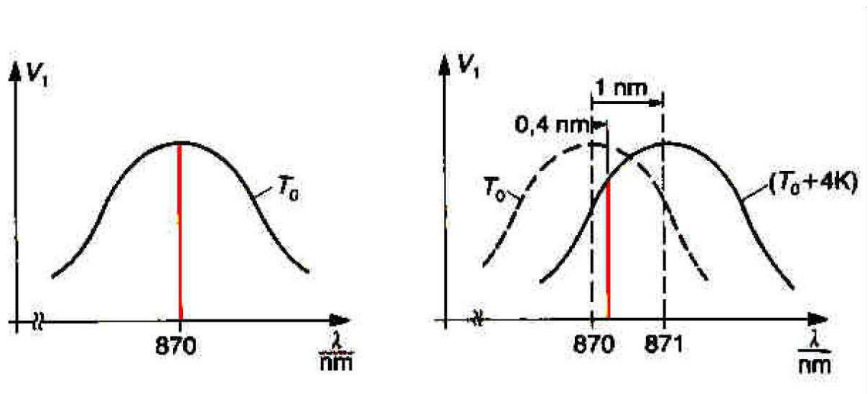

Figure 2.7: Adjustment of the gain curve and longitudinal modes in relation with temperature increase.

A variation of the drive current gives a more restricted tuning range, but allows high frequency modulation of the laser frequency. In practice, these two methods are used in combination.

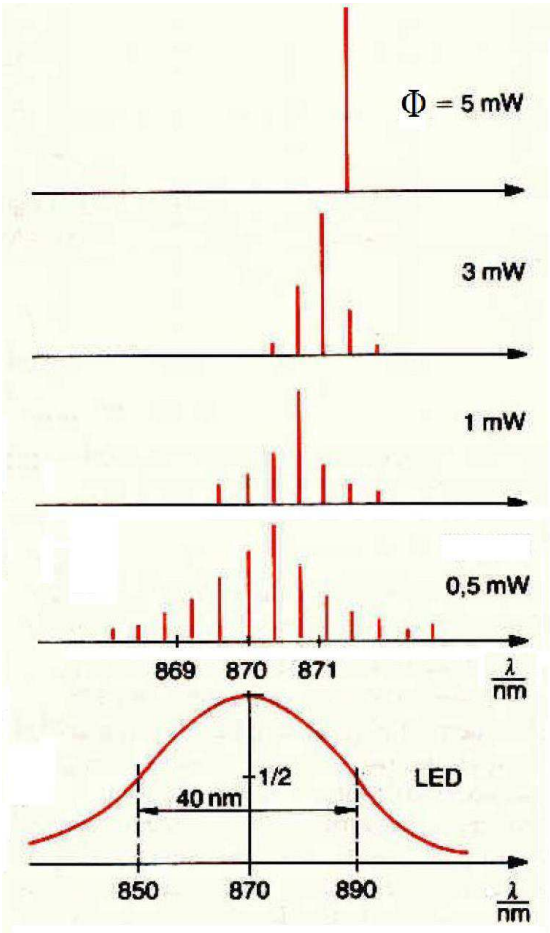

Figure 2.8: Adjustment of the spectrum and suppression of adjacent modes with increasing output power compared to the spectrum of an LED.

It can be seen in figures (2.7) and (2.8) that the modes are approximately contained within an envelope; the maximum of which tunes with the temperature-dependent energy gap of the semiconductor. The band gap shrinks with the temperature which corresponds to the increase in wavelength (with a rate of about 0.24 nm/K for GaAs). The modes themselves tune at a different and slower rate through the temperature dependence of the refractive index, n, and also through the dependence of n on carrier-density, which varies with the laser drive current. At low modulation frequencies the temperature variation of n dominates, but at high frequencies (>1 MHz) thermal inertia reduces the ampli-

tude of the temperature-modulation and carrier-density modulation takes over. The refractive index $n(T)$ increases with the temperature, for GaAs $dn/dT = 4{\cdot}10^{-4}$/K. It follows for a defined mode an increase of $\Delta\lambda/dT = 0.1$ nm/K where the temperature dependence of the resonator length L can be neglected.

An ideal continuously tunable single mode laser is one with an output that can be tuned smoothly over the whole gain bandwidth without any significant reduction in output power. The important factors for a tunable diode laser include the tuning range and speed, side-mode suppression ratio, spectral purity, output power and reliability [53]. There are at least four configurations of tunable lasers in the application of telecommunication networks, and other fields. All of these are promising to replace the current commonly-used distributed feed back (DFB) [54] lasers.

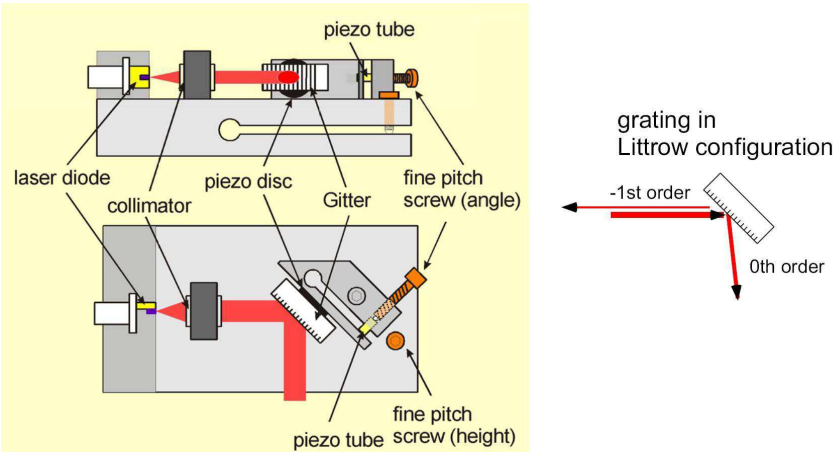

Figure 2.9: Littrow configuration [55].

One practical approach for wavelength tuning of semiconductor diode lasers from those is tunable external cavity diode lasers (ECDLs). An ECDL system consists primarily of a semiconductor diode laser with or without antireflection coatings on one or two facets, collimator for coupling the output of a diode laser, and an external mode-selection filter. In general, the features of a diode laser in an external cavity can change greatly, depending on the length of external cavity, feedback strength, optical power, and diode laser parameters. Littman-Metcalf and Littrow cavity configurations are typical examples of ECDL source in which

gratings are used to provide optical feedback, select single-mode operation, and tune the wavelength over the whole range of gain bandwidth by moving and rotating the grating position.

In our case, a so-called Littrow configuration (figure (2.9)), a grating is used as an external resonator mirror. Since only the diffraction maximum of first order from the grating is coupled back, the grating angle can be targeted to select the frequency. For raw adjustment, the diode temperature is used to get the laser frequency into the right area. For finer tuning, a so-called feed-forward circuit of the grating angle and the diode current are changed continuously to reach the frequency of interest [51].

Chapter 3

Plasma sources and Diagnostics

3.1 Plasma sources

3.1.1 Radio frequency discharge

Capacitively driven radio frequency (rf) discharges are commonly used for materials processing. A typical scheme of a symmetrically driven discharge is shown in figure (3.1). The operating principle for this type of discharges is reasonably well understood. The mobile plasma electrons respond to the instantaneous electric fields produced by the rf driving voltage. They therefore oscillate back and forth within the positive space charge cloud of the ions. Meanwhile, the massive ions only react with the time-averaged electric fields. The oscillation of the electron cloud creates sheath regions near each electrode. The sheath region contains a net positive charge in average over an oscillation period. The excess appears within the sheaths producing a strong time-averaged electric field which directed from the plasma to the electrode. Under the driving of this field, ions flowing out of the bulk plasma near the center of the discharge are accelerated to high energies as they reach the substrate, leading to energetic-ion enhanced processes. The ion-bombarding energies E_i can be as high as $V_{rf}/2$ for symmetric systems (figure (3.1)) and as high as V_{rf} at the powered electrode for asymmetric systems [30].

Positive ions continuously flow out of the plasma over an rf cycle. In contrast, electrons are lost to the electrode only when the oscillating cloud closely ap-

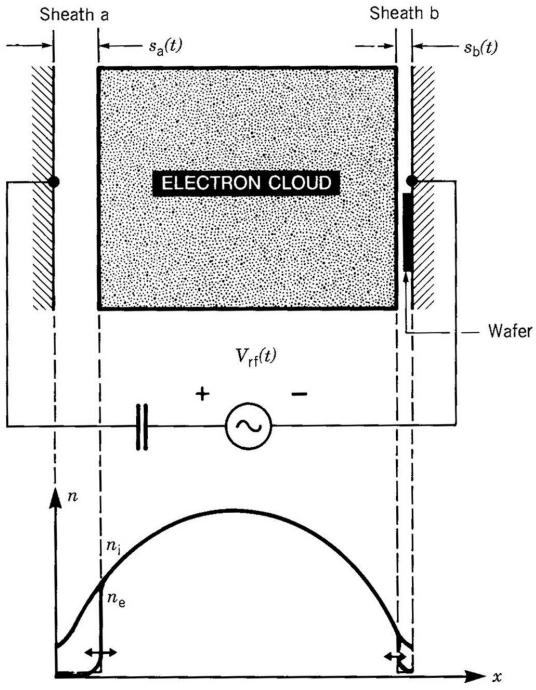

Figure 3.1: The physical model of an rf diode. (From "Design of High-Density Sources for Materials Processing" from the work "Physics of Thin Films," Vol. 18, by Academic Press, Inc., Publisher in Press)

proaches the electrode. During that time, the instantaneous sheath potential collapses to near zero, allowing sufficient electrons to escape to balance the ion charge delivered to the electrode. Except for such brief moments, the instantaneous potential of the discharge must always be positive with respect to any large electrode and wall surface; otherwise the mobile electrons would quickly leak out. Electron confinement is ensured by the presence of positive space charge sheaths near all surfaces.

The dust particles only feel the period averaged electric field like ions but cannot react to the brief moment when the instantaneous sheath potential collapses like electrons. Therefore the negatively charged heavy particles are confined permanently in the plasma. The possibility for dust particle to escape occurs only after glow, e.g., in the off phase of a pulsed rf discharge.

3.1.2 The PULVA1 reactor

In this section, the experimental setup of the PULVA1 reactor which specially designed for a study of dusty plasmas will be discussed including the detail configuration of the discharge chamber including its vacuum system and power supply and the dust injection and confinement units as well.

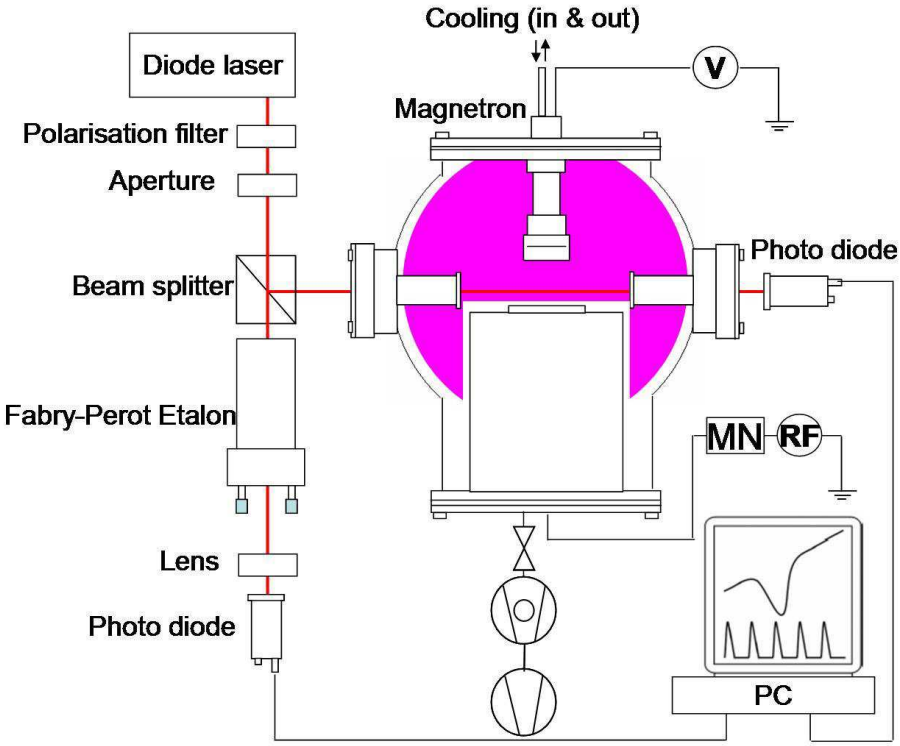

Figure 3.2: Experimental set-up (schematic).

The discharge chamber

Our experiments were performed in the PULVA1 reactor [44, 56, 57]. It consists of a vacuum chamber with 40 cm diameter. The bottom electrode has a diameter of 13 cm and is situated near the center of the chamber; the chamber's wall serves as the other electrode. A copper ring with radius of 4 cm or 6 cm was placed on the powered electrode to confine injected dust particles.

The chamber is pumped by a turbo molecular pump (TMP) with a pumping

speed of 260 l/s that is backed by a membrane pump. The residual gas pressure is 10^{-4} Pa. An adjustable butterfly valve is mounted between TMP and chamber to control the working pressure. The buffer (Ar, Ne, or N_2) and processing (CH_4, C_2H_2, or C_3H_6) gases are introduced into the vacuum chamber by two separate flow controllers. Measurements were carried out at working pressures of 1-20 Pa.

The dustshaker

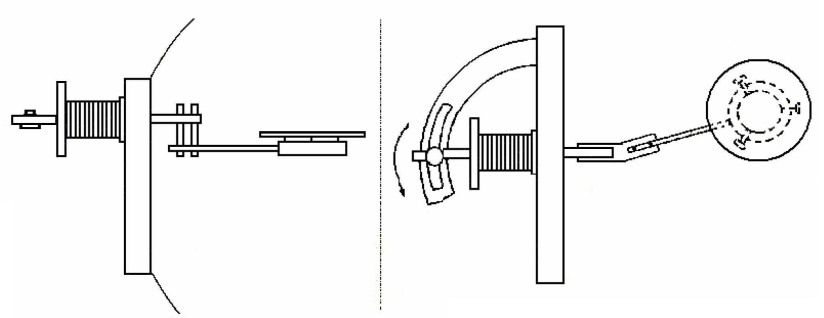

Figure 3.3: Schematic setup of the dustshaker: side view (left) and top view (right).

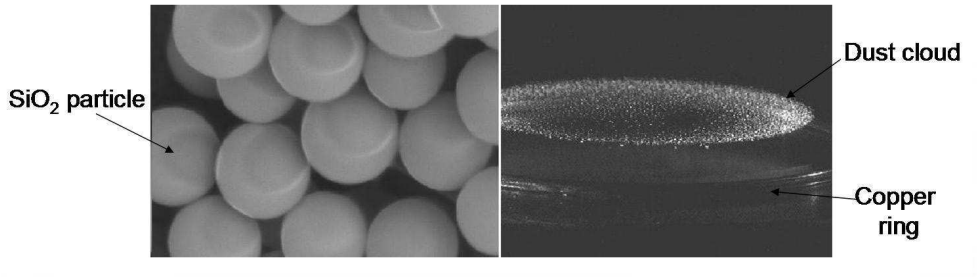

Figure 3.4: SiO_2 particles and their trapping in plasma.

Dust particles were introduced into plasma by a "dustshake" mounted on the side of the plasma chamber. The head of the dustshaker which was used as powder container as well as powder dropper is schematically drawn in figure (3.3). The powder lies on a sieve with 50 μm holes. This head was connected to the chamber via a movable handle with which one can move the dust container to the position where powder particles were injected. By shaking the handle the powder particles

fall down through the sieve. After the particles have been injected, the dustshaker will be displaced to the position where it does not affect the plasma.

The particles used in our experiments are spherical SiO_2 particles with a diameter of 10 μm. The injected particles were confined in the sheath region by the potential well generated by the copper ring (see figure (3.4))

RF-Power-supply

The discharge is driven at 13.56 MHz by a rf generator Cesar from Dressler (figure (3.5)) coupled to the bottom electrode by a matching network. The input power can vary from 0 up to 300 W. The rf generator can work in both pulsed and continuous modes. In pulsed mode, the pulsed frequency ranges from 100 Hz to 30 kHz.

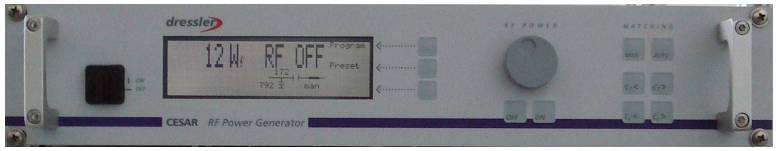

Figure 3.5: RF generator Dressler.

3.1.3 Principle and setup of planar magnetron discharge

A typical planar magnetron sputtering system consists of a planar cathode (sputtering source or target) parallel to an anode surface (usually grounded), which serves as a substrate holder [58, 59]. The cathode assembly consists of the source material, dependent on the deposited layer, directly connected with the backing power electrode. Magnets are placed below the backing electrode. The structure of the magnetron is shown in figure (3.6). The important parts of magnetron are numbered as: 1 magnets, 2 magnetic circuit and target clamp (iron), 3 coolant chamber, 4 shielding (ground), 5 insulator, 6 target (Ti), 7 cooper meant, 8 water tube cooling, 9 substrate [60].

If a negative voltage is applied to the cathode and the pressure is low enough, a glow discharge is formed. Negative particles (mainly electrons) of a dc glow

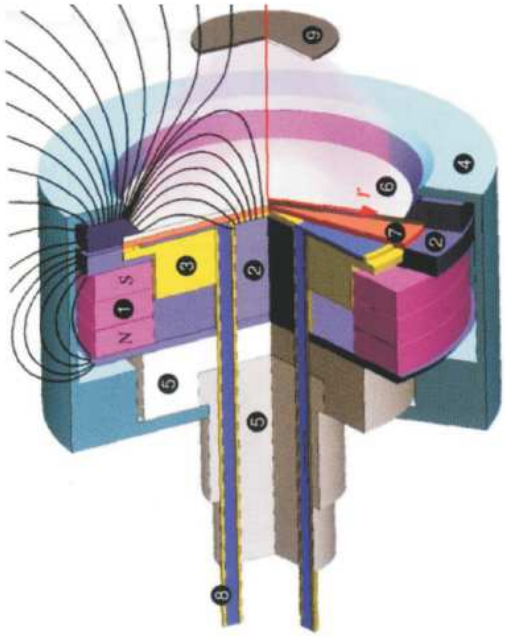

Figure 3.6: The cross-section of a magnetron [60].

discharge are trapped by the magnetic field, which in a certain region above the cathode runs parallel to the cathode surface. Such a configuration increases the electron density in a localized zone. The increased electron concentration leads to higher ion production through ionization collisions. Radial current distribution is peaked at the radius at which the magnetic field is parallel to the cathode plate [61]. The strong electric field between the positive glow plasma and the cathode accelerates ions towards the cathode, where they sputter the cathode material. The most intensive sputtering of the target is visible as an erosion rill called race-track [62].

3.2 Diagnostics

Tunable diode laser absorption spectroscopy (TDLAS) is our main means of diagnostics. In this section, we will first describe the optical principle of absorption spectroscopy, the TDLAS setup with tunable diode laser system from Toptica and the method of measuring. Descriptions of other diagnostic methods used in

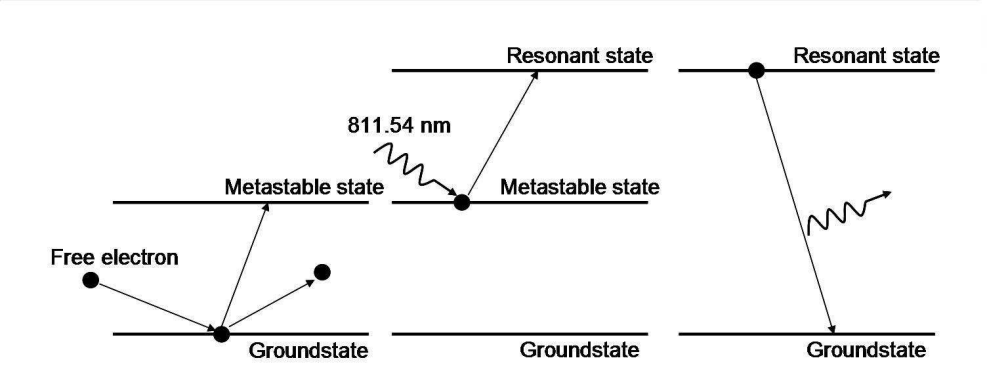

Figure 3.7: Illustration of the principle of absorption spectroscopy.

our study can be found in references cited in corresponding sections.

3.2.1 Principle of Tunable Diode Laser Absorption Spectroscopy

Absorption spectroscopy

The density of a atomic plasma species can be measured by means of absorption spectroscopy: light of a wavelength corresponding to a transition between the interested state and an excited state of a gas atom is send through the discharge. For example, as Ar metastable is interested, the photons excite metastable states to a higher resonant state (see figure 3.8), as a result the intensity transmitted through the discharge I is smaller than the incoming intensity I_0. The difference in these intensities is a measure for the number of absorbed photons, which in turn is a measure of the atom density.

The relation between I_0 and I is described by Lambert-Beer-law:

$$I(\nu) = I_0(\nu) \exp\left(\tau_{ab}(\nu)\right) \tag{3.1}$$

in which τ_{ab} is the optical depth. τ_{ab} is equal to the integral of the absorption

coefficient, κ_z, over the optical path through the discharge:

$$\tau_{ab} = \int_l \kappa_z dz \tag{3.2}$$

where κ_z is a function of the density n of the absorbing particle, described by:

$$\kappa_z = n \cdot \sigma \tag{3.3}$$

in which σ is a cross-section constant. This method is unsuitable for measuring the density at an arbitrary point on the line of absorption but the line-integrated density n over the length l.

Using the line-integrated density and regarding equation (3.3), equation (3.2) is rewritten as follow:

$$\tau = n \cdot \sigma \cdot l. \tag{3.4}$$

The relation between the measured intensities and the average particle density is therefore expressed as:

$$I(\nu) = I_0(\nu) \cdot \exp(-n\sigma l) \tag{3.5}$$

In order to calculate the absolute metastable density one needs the expression for σ [63].

$$\sigma(\nu) = \frac{c^2}{8\pi\nu^2} B \frac{g_k}{g_i} \left(1 - \frac{g_i}{g_k}\frac{n_k}{n_i}\right) \phi(\nu) \tag{3.6}$$

σ depends on both the density of the lower and higher levels, n_i and n_k respectively, and on their statistical weights g_i and g_k, as well as on the transition probability B for spontaneous emission and the central wavelength λ_0 of the transition. $\phi(\nu)$ is the absorption profile of the transition. The area of $\phi(\nu)$ is normalized to the unity. The second term in parenthesis represents stimulated emission and can be neglected if the density of the upper level is small compared to the density of the interested level which is of ground state (Al ground state) and metastable (Ne and Ar metastables) state for our investigations.

At our low temperature low pressure plasma condition beside the natural line broadening which is negligible we consider only the Doppler broadening which caused by the Brownian motion of atoms. The ensemble has a distribution according to of Maxwell and emits light with a line profile in the form of a Gaussian function:

$$\phi(\nu) = \frac{1}{\triangle\nu_{1/e} \cdot \sqrt{2\pi}} \cdot \exp\left\{-\frac{1}{2}\left(\frac{\nu - \nu_0}{\triangle\nu_{1/e}}\right)^2\right\} \tag{3.7}$$

where $\triangle\nu_{1/e}$ is the full 1/e width:

$$\triangle\nu_{1/e} = \frac{1}{\lambda_0}\sqrt{\frac{k_B T}{m_a}} \tag{3.8}$$

where m_a is atomic mass of interested atom. Therefore

$$\phi(\nu) = \frac{2\sqrt{ln2}}{\sqrt{\pi}\Delta\nu_D} \cdot \exp\left\{-\left(\frac{2\sqrt{ln2}(\nu - \nu_0)}{\Delta\nu_D}\right)^2\right\} \tag{3.9}$$

where $\Delta\nu_D$ is full width at half maximum:

$$\Delta\nu_D = \frac{2\sqrt{ln2}}{\lambda_0}\sqrt{\frac{2k_B T}{m_a}} \tag{3.10}$$

Inserting equation (3.10) and the expression for σ into equation (3.5) one obtains:

$$I(\nu) = I_0(\nu) \cdot \exp\left\{-n_i\sigma_0 l \cdot \exp\left[-\left(\frac{2\sqrt{ln2}(\nu - \nu_0)}{\Delta\nu_D}\right)^2\right]\right\} \tag{3.11}$$

where

$$\sigma_0 = \frac{c^2}{8\pi\nu^2} B \frac{g_k}{g_i} \frac{2\sqrt{ln2}}{\sqrt{\pi}\Delta\nu_D} \tag{3.12}$$

Using Ladenburg's formula:

$$B = \frac{1}{4\pi\varepsilon_0}\frac{8\pi^2 e^2 \nu^2}{m_e c_0^3}\frac{g_i}{g_k} f_{ik} \tag{3.13}$$

one gets the relation for the cross section constant σ_0, the absorption coefficient κ_0, and the optical depth at the central profile as:

$$\sigma_0 = \frac{1}{4\pi\varepsilon_0}\frac{\pi e^2}{m_e c_0}\frac{2\sqrt{ln2}}{\sqrt{\pi}}\frac{f_{ik}}{\Delta\nu_D} \tag{3.14}$$

$$\kappa_0 = \frac{1}{4\pi\varepsilon_0}\frac{\pi e^2}{m_e c_0}\frac{2\sqrt{ln2}}{\sqrt{\pi}}\frac{n f_{ik}}{\Delta\nu_D} \tag{3.15}$$

$$\tau_0 = \frac{1}{4\pi\varepsilon_0}\frac{\pi e^2}{m_e c_0}\frac{2\sqrt{ln2}}{\sqrt{\pi}}\frac{n_i f_{ik} L}{\Delta\nu_D} \tag{3.16}$$

The width of the absorption signal is related to the gas temperature T as:

$$T = \frac{\lambda_0^2 m_a}{8k \ln 2}\Delta\nu_D^2 \tag{3.17}$$

The atom density n_a is related to the integrated absorption profile $\kappa(\nu)$ [64]:

$$n_a = \frac{4\pi\varepsilon_0 m_e c}{e^2 f_{ik}\lambda_0}\sqrt{\frac{2kT}{\pi m_a}}\kappa_0 \tag{3.18}$$

where κ_0 is the absorption coefficient in the center of the profile, ε_0 the dielectric constant, c the speed of light, m_e and e electron mass and charge, respectively, m_a the atomic mass, k is the Boltzmann constant, λ_0 is the central wavelength of the investigated transition and f_{ik} the optical oscillator strength for the investigated transition.

3.2.2 Optical setup of TDLAS

The laser system consists of tunable single-mode diode laser and a control unit for diode temperature and diode current (Toptica DL 100) [65]. The diode laser utilizes an external cavity laser set-up with optical feedback into the laser diode

from the first order of a spectrally selective grating (figures (2.9) and (3.8)). The laser light transverses a polarization filter and is directed onto a beam splitter. The transmitted light is registered by a photo diode behind a Fabry-Perot etalon to monitor the light frequency [66]. The second light beam traverses the plasma chamber and is detected by a second photodiode.

The diode laser system Toptica Photonics DL 100

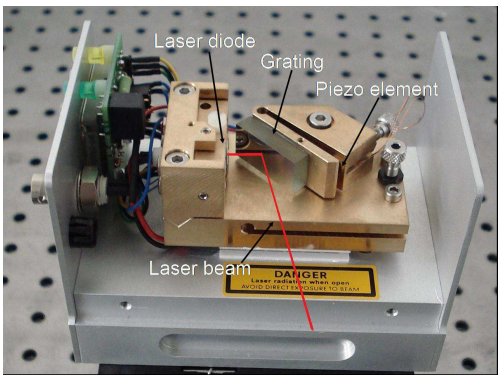

Figure 3.8: DL 100 laser head using Littrow configuration.

The control unit is a 19-inch panel which encloses different slots. The DC 110 monitor unit is used for control of the laser system. On a small digital display, all current, nominal and off limit parameters are monitored. Diode temperature is controlled by the DTC 100 unit. The DTC controls a Peltier element, which itself controls the temperature of the laser diode and thus the laser wavelength. The power control unit DCC 110 serves to adjust and to control the diode current. The last slot in the control unit is a SC 110 (scan control). It is used to control the piezoelectric crystal voltage which controls the angle of the Littrow grating. The Littrow angle is determined by the following equation:

$$\sin(\alpha) = \frac{k\lambda}{2d} \tag{3.19}$$

where α is the angle of the incident laser beam on the grating normal, k the diffraction order (in this case $k = 1$), d the lattice constant (in this case, $d = 278$ nm) and λ is the wavelength. A reduction of the angle leads to smaller wavelengths and vice versa.

The piezo control voltages can also be used as a trigger signal for absorption measurements.

Perot-Fabry-Etalon

A Fabry-Perot etalon is the simplest form of a Fabry-Perot interferometer. The primary optical property of a Fabry-Perot etalon is that only a monochromatic light ray which travels back and forth between two mirrors has the back-and-forth optical distance between the mirrors equals an integral number of wavelengths (λ, 2λ, 3λ etc.), can pass through the etalon.

There are two types of etalon:

a. Planar etalon consists of two very flat, very parallel mirrors.

b. Confocal or spherical etalon is made from two identical spherical mirrors with their concave sides facing each other, the distance between the mirrors equal to each mirror's radius of curvature.

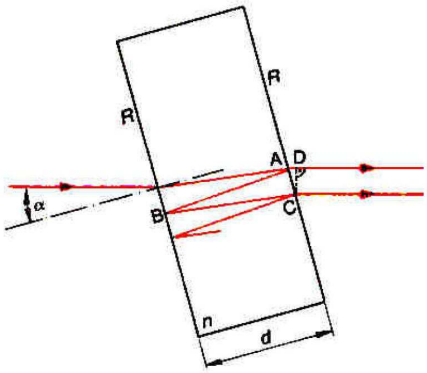

Figure 3.9: A partly mirrored plane parallel quartz plate is an Etalon.

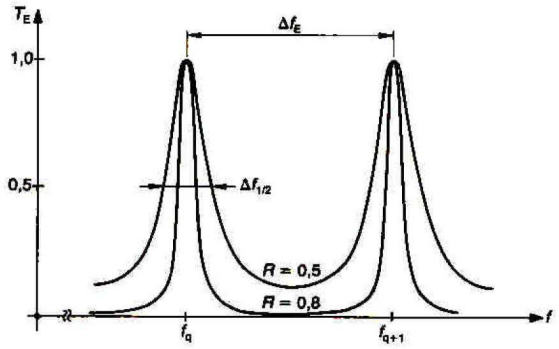

Figure 3.10: Transmission of ideal Etalon with reflectivity R = 0.5 and R = 0.8.

Planar Etalon Theory

The equation for the transmission of an ideal etalon, an Airy Function, is

$$T_E = \left[1 + \frac{4R}{1-R^2}\sin^2\left(\frac{\phi}{2}\right)\right]^{-1} \tag{3.20}$$

where T_E is the transmission, R is the reflectivity of the mirrors, and ϕ is the roundtrip phase change of the light ray.

If any phase change at the mirror surfaces is ignored then

$$\phi = \frac{2\pi}{\lambda} 2nd\cos\theta \tag{3.21}$$

where:

λ = the wavelength of the light

n = the index of refraction of the material between the mirrors

d = the distance between the mirrors

θ = the angle of the incoming light beam

Figure (3.10) shows the etalon spectral transmission. The Free Spectral Range (Δf_E) is determined by the distance between adjacent peaks. The width (FWHM) of each peak is the resolution ($\Delta f_{1/2}$). The Free Spectral Range in frequency unit can be written in the following way:

$$\Delta f_E = \frac{c}{2nd} \tag{3.22}$$

Another useful concept for etalons is the finesse (**F**). This dimensionless parameter is the ratio between the free spectral range and the peak width.

$$\mathbf{F} = \frac{\Delta f_E}{\Delta f_{1/2}} \tag{3.23}$$

For an ideal etalon, the finesse is determined only by the mirror reflectivity.

$$\mathbf{F} = \mathbf{F}_R = \frac{\pi\sqrt{R}}{1-R} \tag{3.24}$$

Confocal Fabry-Perot Interferometer

The FPI 100 used in TDLAS experiments with Ar is a confocal Fabry-Perot Interferometer with high finesse (**F**) and ease of alignment as well as stable reference cavity. Its mirror radius is 75 mm which gives a free spectral range (FSR) of 1

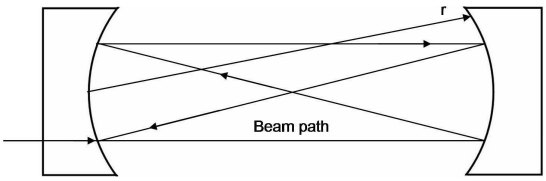

Figure 3.11: Confocal interferometer configuration.

GHz.

When illuminated by monochromatic light rays close to the axis, a multiple beam interference pattern is produced near the center of the interferometer. At precisely the confocal spacing, each mirror images the other back upon itself so that a paraxial ray is re-entrant, i.e. falls back upon itself after four traversals of the interferometer (figure (3.11)). This is not strictly true for real rays, where successive traversals of the interferometer are not perfectly re-entrant but for paths close to the axis multiple reflections will continue to intersect at the beam waist, creating an interference pattern. Four traversals of the cavity means that the transmitted spectrum is reproduced with every quarter wavelength ($\lambda/4$) change in the mirror separator. Consequently the free spectral range is also given by equation (3.22).

The etalon makes use of spherical mirrors whose radius of curvature r is equal to the spacing d between the minors. Therefore, Δf_E of a confocal etalon is fixed by the choice of mirrors. This is a disadvantage when compared to a plane parallel Fabry-Perot Interferometer, which can be used at any mirror spacing. On the other hand, the spherical mirror interferometer is much less sensitive to mirror alignment because it is not necessary to maintain mirror parallelism. In addition, the focusing effect of curved mirrors results in a mode with a small diameter on the mirror surface, minimizing the possible finesse degradation due to the mirror surface imperfections. Only the mirror separation and alignment with incident light beam are critical for the performance of a spectrum analyzer, which makes the confocal spectrum analyzer extremely simple to use.

The spectral resolution of any Fabry-Perot interferometer $\Delta f_{1/2}$ for a given Δf_E becomes higher for higher reflectivity mirrors. At high reflectivity the surface

quality of the mirrors may also limit the resolution. Therefore, there are practical limits in the quest of arbitrarily high resolution. One is that the surface quality is bounded by the limitations of mirror polishing. Another is that higher reflectivity produces lower etalon transmission, as coating absorption and substrate scattering losses become magnified by a factor of $(1 - R)^{-1}$. Finesse as high as 10^{-5} has been reported for super-polished substrates with low-pass coatings. However, such mirrors ore environmentally sensitive, and are usually mounted in hermetically sealed housings.

Measuring Method of TDLAS

To perform a measurement the lenses and the mirrors needed to be aligned. After every optical part was set in position the RF discharge was spatially analyzed in different plasma conditions. Three types of experiments were carried out:

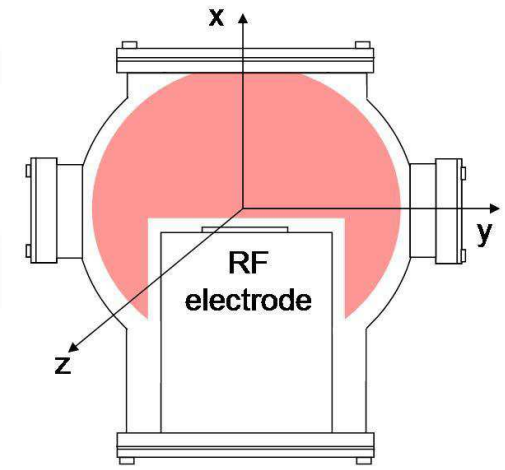

Figure 3.12: Coordinates in Pulva 1.

First, laser beam shining along the y direction (figure (3.12)) was scanned horizontally (along z direction) at 2 fixed heights above the rf electrode: 10 mm (position of plasma sheath); 20 mm (inside the plasma bulk). During the measurement all external conditions like plasma power, pressure and gas flow were kept constant. From the measurement the radial distribution of neon metastable atom density $n_m(x, z)$ and temperature is obtained. Similarly, in order to monitor the axial metastable atom distribution $n_m(x)$, the laser beam was fixed at $z = 0$ and moved along the x direction.

The second type of measurement examines the relation between plasma and working pressure with metastable density and temperature. The laser beam is fixed in one position ($z = 0$, $y = 0$, and at different heights x) while the plasma conditions

were varied.

And finally, in order to study the influence of injected particles on the plasma, particles were injected into or grown inside the plasma. Relative large SiO_2 particles (10 μm) were injected. They were confined in the sheath boundary, about 15 mm above the rf electrode. The laser beam was placed at this height and moved left to right to monitor the radial metastable density with the presence of dust particles or placed at center and moved along x direction to measure the axial density. In the case of grown dust particles the laser was fixed in the center while the plasma power and its modulation were varied.

Chapter 4

Al density in Magnetron discharge with TDLAS

Magnetron discharges are of frequent use in thin film deposition processes, particularly in metal and metal oxide films for commercial use [67, 68]. Despite a large number of previous investigations the fundamental aspects have not yet been fully understood. In this chapter, we report new results of blue tuneable diode laser absorption spectroscopic studies of aluminium atoms in a direct current (dc) and pulsed magnetron discharge, where the density as well as the temperature of sputtered metal atoms are of particular interest.

Laser absorption spectroscopy (LAS) has become a versatile tool in plasma diagnostics [69 – 74]. It offers the opportunity of controlling a relevant plasma parameter like the atom density of selected species and thus may be useful in process control, e.g. in the deposition and etching process. Aluminium atoms are well suited for LAS. The atomic levels of interest are the Al $^2P_{1/2}$ and $^2P_{3/2}$ ground states (separated by 13.9 meV), and the first excited $^2S_{1/2}$ state (figure (4.1)). Ground and first excited states are connected via optical transitions at 394.40 and 396.15 nm which are within the reach of available diode lasers [75, 76]. A further advantage of aluminium is that only one stable isotope exists, thus avoiding complications arising from isotope splitting. There is also some disadvantage as only a fraction of all the ground state atoms is accessible with a single transition. In the present experiment, we made use of the 396.15 nm line, connecting the $^2P_{3/2}$ ground state with the first excited $^2S_{1/2}$ state. In addition,

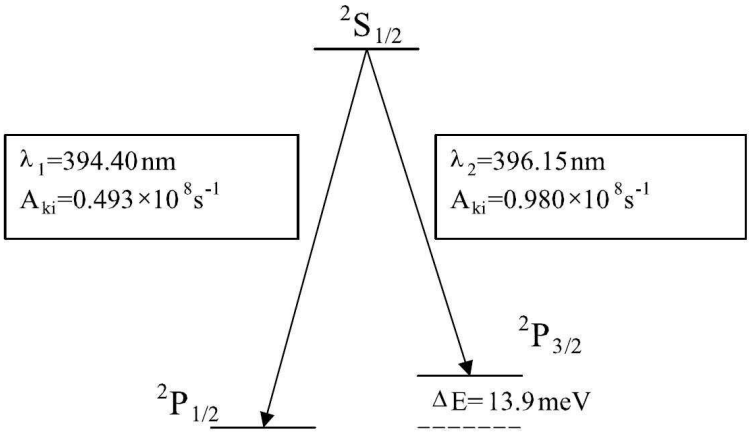

Figure 4.1: Aluminium term diagram of ground and first excited levels (after [75]).

hyperfine interaction needs to be taken into account, giving rise to a splitting of the 396.15 nm transition into six components [64]. Therefore the transmitted photodiode signal was fitted with a sum of six Doppler line profiles.

$$I(\nu) = (a + b\nu + c\nu^2) \cdot \exp\left\{-\kappa_0 l \sum_{i=1}^{6} k_i \exp\left[-\left(\frac{\nu - \nu_0 - \Delta\nu_i}{0.6\Delta\nu}\right)^2\right]\right\} \qquad (4.1)$$

The parameters a, b, and c represent the baseline of the signal, i.e., the transmitted signal without plasma, approximated by a second order polynomial. ν_0 is the central frequency, taken as a free fit parameter, k_i and $\Delta\nu_i$ are the relative intensity and the frequency shift of the ith component of the hyperfine-split transitions with respect to κ_0 [64]. Fitting algorithm [77] was used for selecting the best fit function. The program is based on least squares method with utilization of Nelder-Mead algorithm and it is completely written in Matlab [78]. A typical fit result together with measured data is displayed in figure (4.2). The accuracy of extracted temperature and atom density derived from equations (3.18) and (4.2) depends on the accuracy of the fit function and on the accuracy of the oscillator strength f (about 25%), and the absorption length l inside the plasma

(approximately 5 – 10%). Typical computing error is in case of temperature less than 10 K and in case of aluminium atom density is about 30%.

Measurements of sputtered Al atoms density and temperature were performed for three different gas mixtures: pure argon, argon/oxygen and argon/nitrogen (or argon/methane in pulsed mode). The absorption length $l = 14$ cm was used for determination of parameters a, b, c, ν_0, κ_0, and $\Delta\nu$ in equation (4.2). The obtained results were calculated providing uniform Al atom density inside the vacuum chamber. Different absorption profiles for six different magnetron powers in dc mode are depicted in figure (4.2). Al atom densities derived from these absorption profiles represent only population of ground state $^2\mathrm{P}_{3/2}$. Assuming a Boltzmann distribution for populations of two ground state levels n_1 and n_2

$$\frac{n_1}{n_2} = \frac{g_1}{g_2}\exp\left(\frac{E_2 - E_1}{kT}\right) \tag{4.2}$$

λ (nm)	A_{ki} (10^8 s^{-1})	f_{ik}	E_i (eV)	E_k (eV)	Transition ($i \rightarrow k$)	g_i	g_k
394.401	0.493	0.115	0.0000	3.1427	$^2S_{1/2} \rightarrow ^2 P_{1/2}$	2	2
396.152	0.980	0.120	0.0139	3.1427	$^2S_{1/2} \rightarrow ^2 P_{3/2}$	4	2

Table 4.1: Spectroscopic data of the studied Al transition.

where g_1 and g_2 are statistical weights of the particular levels and E_1 and E_2 are energies of these levels (see table (4.1)), we can find the correction factor. For example with gas temperature $T = 500$ K, the correction factor is 1.69, that means about 59.2% of Al atoms are in state $^2\mathrm{P}_{3/2}$ and 40.8% in state $^2\mathrm{P}_{1/2}$. The densities reported below have been corrected accordingly using the experimentally determined temperature.

4.1 Continuous magnetron plasma

4.1.1 Argon

The measured Al atom density for pure argon as working gas is displayed in figure (4.3) as a function of discharge power and for different working pressures ranging

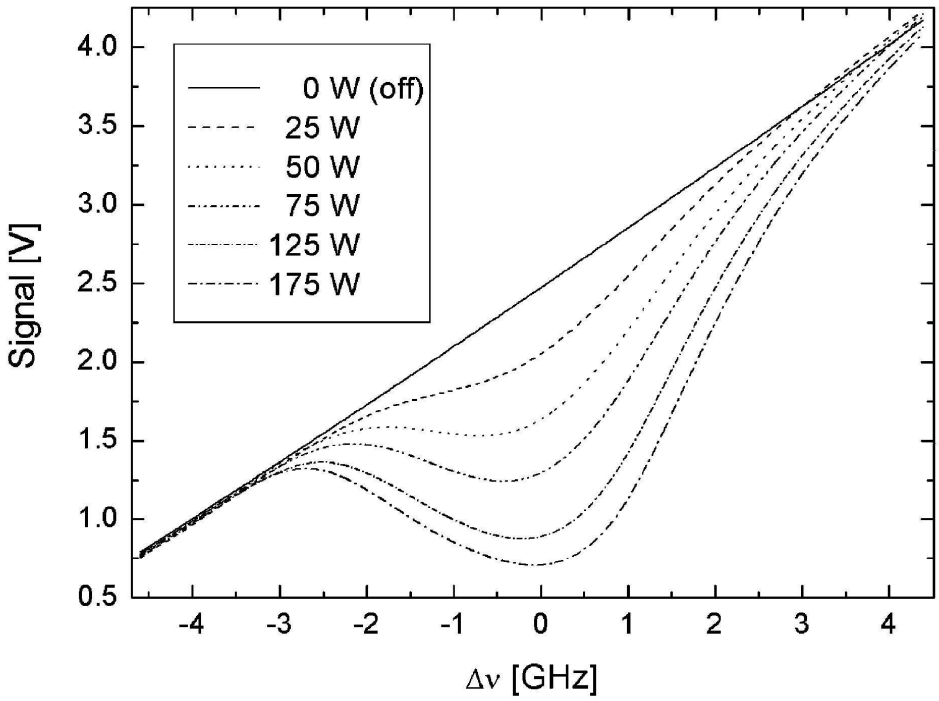

Figure 4.2: Measured absorption profile for various discharge powers in DC mode and for argon as a working gas.

from 3 – 9 Pa. Over the investigated range, the density increases approximately linearly with magnetron power. In addition, some variation with Ar gas pressure is observed: a pronounced increase with pressure up to 7 Pa followed by a moderate decrease (figure (4.4)). The measured temperature versus discharge power is displayed in figure (4.5). The temperature moderately increases with increasing discharge power, from about 330K at 20W to 420K at about 250W.

The measured Al density is in reasonable agreement with estimates based on the sputtering theory. Aluminium atoms are produced by Ar^+ ions impinging on the target; the production rate $\dot{R}_{Al}$ of aluminium atoms is, therefore, related to the rate $\dot{R}_+$ of argon ions hitting the target multiplied by the sputtering yield Y. Relating the discharge current I at the target of the impinging Ar^+ ions, and neglecting emission of secondary electrons which, at energies of interest here, are believed to contribute not more than a few percent [79], we write

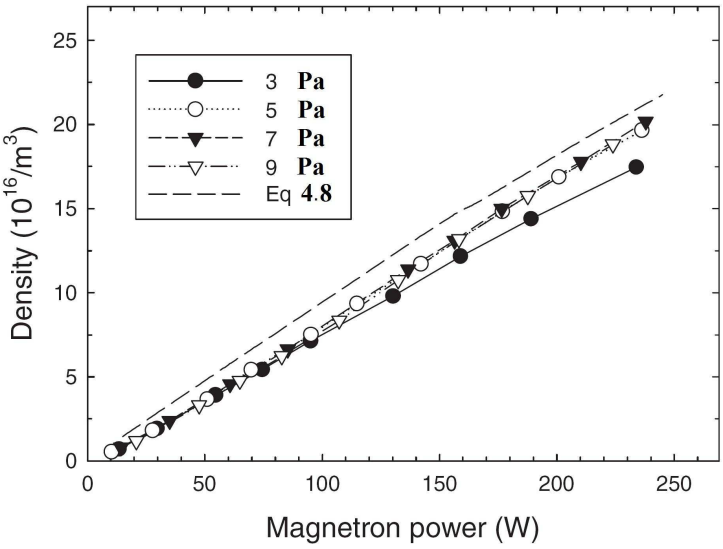

Figure 4.3: Measured Al atom density versus discharge power for different discharge pressures and with argon as working gas. Solid lines are to guide the eye only. Dashed line calculated according to equation (4.8) (see text).

$$\dot{R}_{Al} = Y\dot{R}_{+} \approx \frac{YI}{e_0} \tag{4.3}$$

where e_0 is the elementary charge. In the kinetic energy range $E_{kin} \approx 200$ – 400 eV of interest here, the sputtering yield as obtained from our own transport of ions in matter (TRIM [80]) calculations is approximately given as

$$Y = c_s E_{kin} = c_s e_0 U \tag{4.4}$$

with $c_s = 0.00143$ atoms eV^{-1}. The sputtered Al atoms at the neutral gas densities of interest here thermalize within 2 to 3 cm mainly through collisions with gas (Ar) atoms; the mean velocity $\bar{v}$ is given as follows:

$$\bar{v} = \sqrt{\frac{8kT}{\pi m_a}} \tag{4.5}$$

where k is the Boltzmann constant and m_a the aluminium atom mass. In the

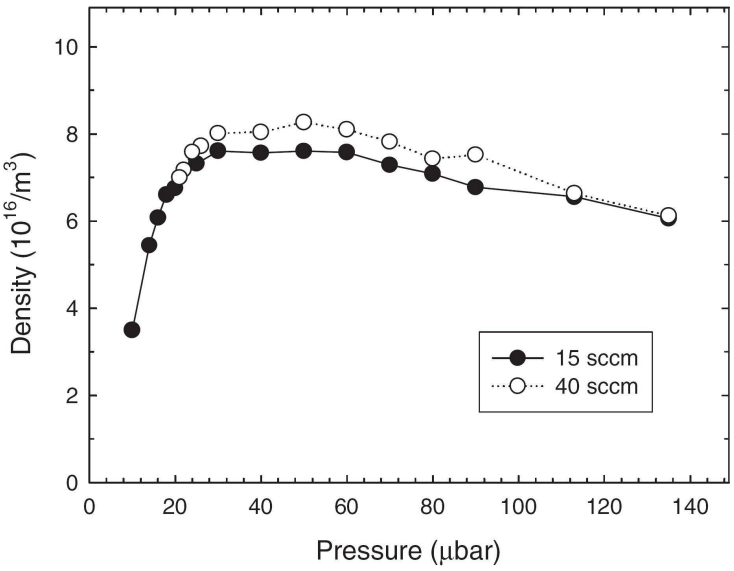

Figure 4.4: Measured Al atom density versus argon gas pressure. Discharge power 100W, gas flow 15 sccm (solid dot) and 40 sccm (opened dot). Solid lines are to guide the eye only.

following we assume a constant aluminium density inside the plasma chamber. The crude assumption appears reasonable since the magnetron dimensions are comparable with the chamber diameter. Loss of aluminium atoms occurs at the chambers walls, where the flow density j_{Al} of Al atoms to the walls,

$$j_{Al} = \frac{1}{4} n_{Al} \bar{v} = \frac{1}{4} n_{Al} \sqrt{\frac{8kT}{\pi m_a}} \tag{4.6}$$

multiplied by the inner surface area $A = 4\pi r^2$ (with $r = 7.5$ cm) of the chamber equals the aluminium atom production rate,

$$j_{Al} A = \bar{R}_{Al} \tag{4.7}$$

from which the aluminium atom density is obtained as follows:

$$n_{Al} = \frac{4 c_s P_M}{A} \sqrt{\frac{8kT}{\pi m_a}} \tag{4.8}$$

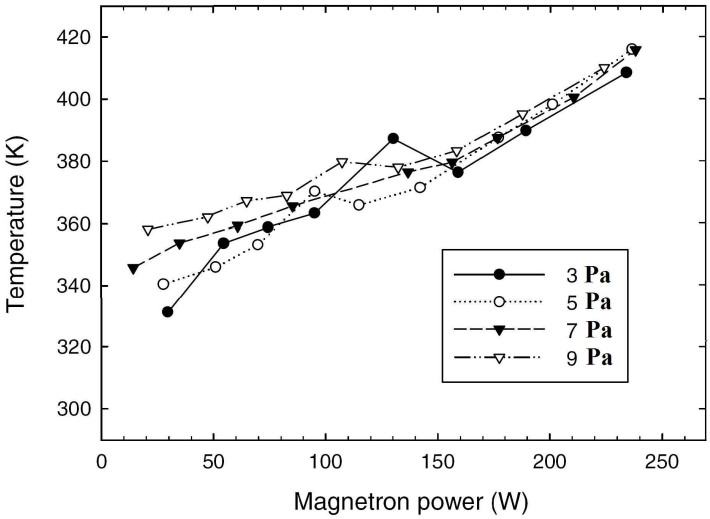

Figure 4.5: Measured Al atom temperature versus discharge power for different discharge pressures and with argon as working gas.

Evidently, the aluminium density is almost linearly depending on the magnetron power P_M. The aluminium density calculated with the help of equation (4.8) is shown in figure (4.3) for an argon pressure of 7 Pa. Similar curves obtained for argon pressures of 3 and 9 Pa deviate less than 10% from this curve. The predicted aluminium atom density is in excellent agreement with the experimental results. However, in the light of the crude approximations used here, this should be considered fortuitous. For example, the experimentally observed pressure dependency is not properly predicted by the present model. Possible reasons are the deviations from the underlying assumption of a linearly depending sputtering yield on ion energy (equation (4.4)) and/or by not properly taking into account the transport (diffusion) of aluminium atoms in the working gas.

4.1.2 Argon/nitrogen gas mixture

Figure (4.6) shows the measured Al atom density for argon with nitrogen admixtures as working gas versus nitrogen gas flow, at a constant argon gas flow of 40 sccm corresponding to a gas pressure of 5 Pa. The nitrogen admixture leads to

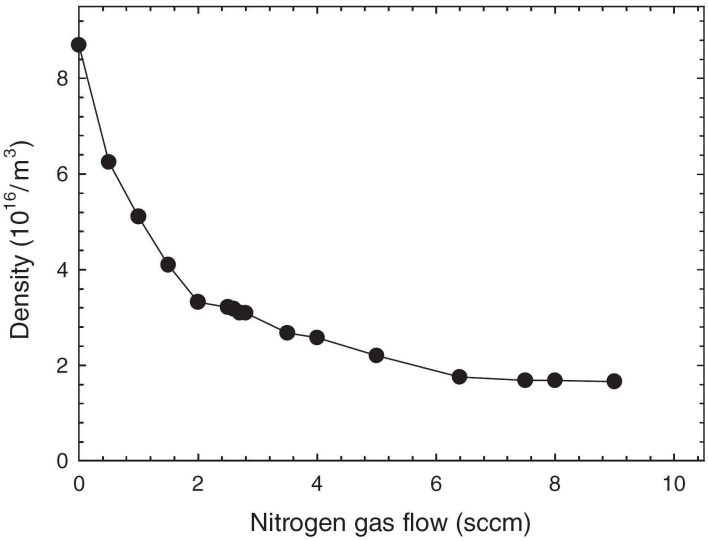

Figure 4.6: Measured Al atom density versus nitrogen gas flow. Working pressure 50×10^{-3} mbar, Ar flow 40 sccm, discharge power 100W.

a pronounced decrease of the measured Al atom density. At a nitrogen gas flow of approximately 8 sccm, the absorption signal drops to about 19% corresponding to a decrease of the Al density by 81%. The decrease may be explained by the sputtering theory which, for a stoichiometric Al_3N_4 layer, predicts a rather similar reduction to 22 – 26% for bombarding energies of 200 – 400 eV, as was corroborated by our own TRIM [80] simulations.

4.1.3 Argon/oxygen gas mixture

Figure (4.7) shows the measured Al atom density for argon with small oxygen admixtures as working gas versus oxygen gas flow, at a constant argon gas flow of 40 sccm corresponding to a gas pressure of 5 Pa. At a magnetron power of 200 W, a small admixture of oxygen already leads to a significant decrease of the measured Al atom density. At an oxygen gas flow of approximately 1 sccm, corresponding to an oxygen admixture of only 2.5%, the absorption signal completely disappears, indicating almost zero Al atom density. This drastic effect is due to a poisoning (oxidation) of the magnetron aluminium target as a result of the formation of a

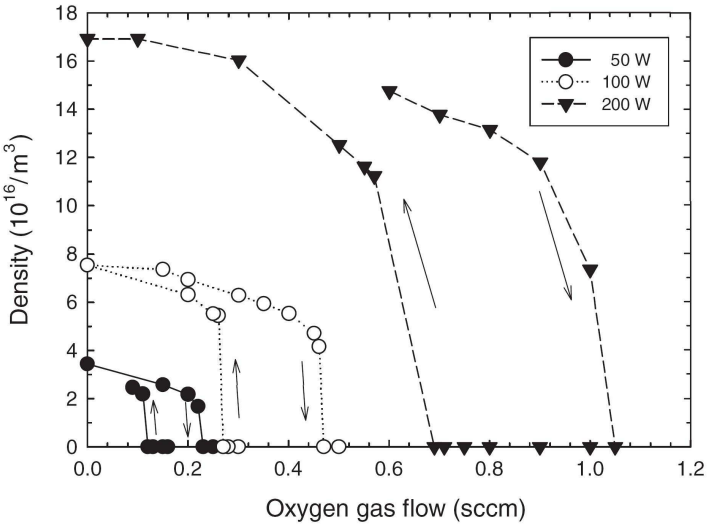

Figure 4.7: Measured Al atom density versus Oxygen gas flow. Arrows indicate increasing or decreasing oxygen flow. Working pressure 5 Pa, Ar flow 40 sccm, discharge power 50 W, 100 W, and 200 W.

compound surface layer, and has been noticed before [82]. It goes along with a change in the current-voltage characteristics of the magnetron, e.g. in our case a sudden voltage drop by about 20 V and a simultaneous current increase by about 60 mA. Reduction of the oxygen flow leads to a hysteresis type dependence with the absorption signal reappearing below 0.6 sccm. Similar curves are observed at discharge powers of 50 and 100 W. However, the complete disappearance of the signal and, therefore, of the Al atom density comes as somewhat of a surprise. We confirmed this result by optical emission spectroscopy studies at a discharge power of 100 W. The unresolved 394/396 nm lines of Al beside lines from neutral Ar dominate the emission spectrum. For an oxygen flow exceeding 0.5 sccm the Al signal rather completely disappears as it drops by a factor of about 30. At the same time, the Ar lines remain more or less unaffected and an increased intensity of molecular bands of AlO at wavelengths of 484.21 and 486.61 nm [81] was noted. This result is further confirmed by deposition experiments which yield a reduction of the aluminium oxide deposition rate as compared to the aluminium deposition rate without oxygen by a factor of ≈ 25. The sputtering theory would explain a reduction by a factor of about 2 only, as was corroborated by our own

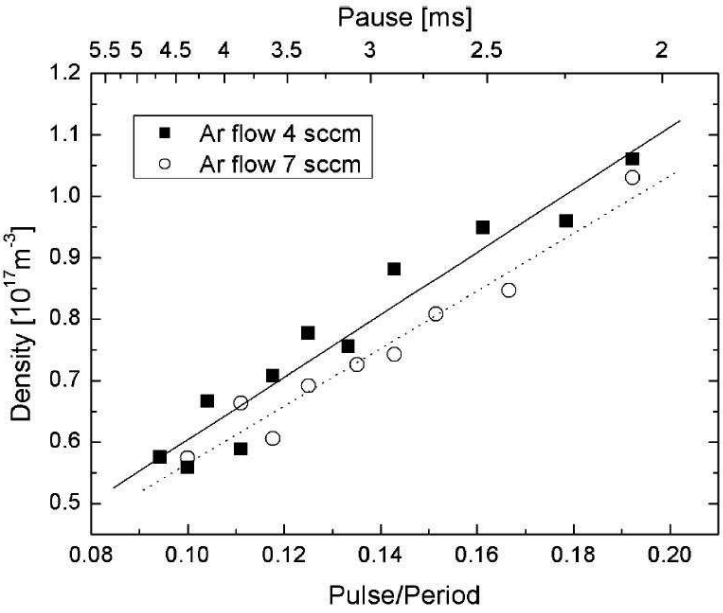

Figure 4.8: Apparent Al density as a function of pulse timing under constant length of active part of the pulse (0.5 ms) and constant current in the pulse (5 A) measured for two different Ar gas flows. Working pressure was 3 Pa.

TRIM simulations. Hence, other effects like a change of the secondary electron and negative ion yields are believed to contribute to this effect [82, 83].

4.2 Pulsed magnetron plasma

Interpretation of results in case of pulsed magnetron discharge is not as simple as in the previous case. As the sampling frequency of the used photodiode is significantly lower than the frequency of pulse source and on this account we can observe only the total integrated absorption signal. In order to find a relation between measured signal, real density of Al atoms and timing of pulse excitation we performed measurement of apparent Al atom density as a function of pause duration (see figure (4.8)). Pulse duration (0.5 ms) and discharge current during pulse (5A) were kept constant. On that account the density of sputtered Al atoms during the active part of the pulse was assumed to be uniform while the appar-

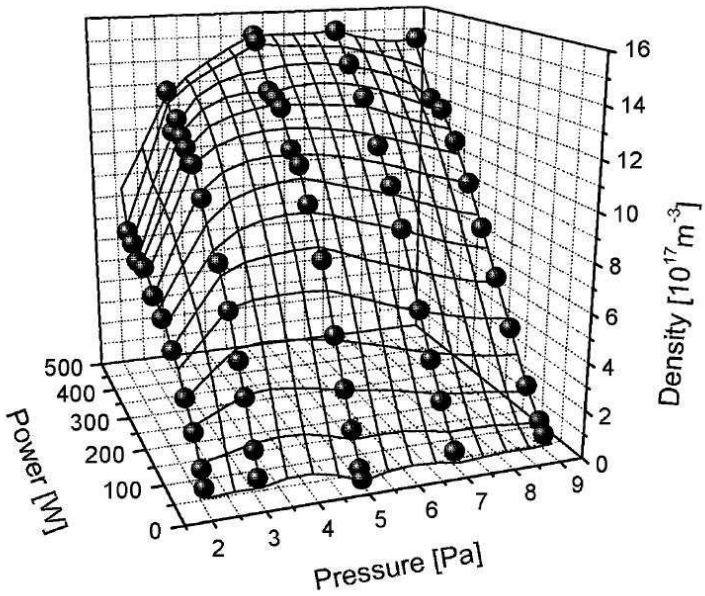

Figure 4.9: Measured Al atom density in pulse as a function of argon gas pressure and magnetron power. Ar gas flow was 10 sccm, length of active part of pulse was 0.23 ms, length of space was 1.5 ms. Full lines to guide your eye only.

ent density calculated directly from equations (3.18) and (4.2) increased linearly with increasing ratio T_{pulse}/T_{period}. Therefore we determined an approximate correction factor 7.5 that expresses the relation between apparent density and real density during the pulse. All densities in pulsed discharge reported below have been corrected by this factor. It is obvious that the accuracy of results in pulsed magnetron is significantly lower than in dc mode.

4.2.1 Argon

Al atom density in the active part of pulse measured at mentioned values of T_{pulse} and T_{period} is displayed in figure (4.9) as a two-dimensional function of working pressure and magnetron power. The shape of resulting graph is similar to dc mode, but resulting values are approximately four times higher at the same value of absorbed power. Instantaneous value of discharge current in the pulse is approximately 7.5 times higher than in dc mode at the same absorbed power.

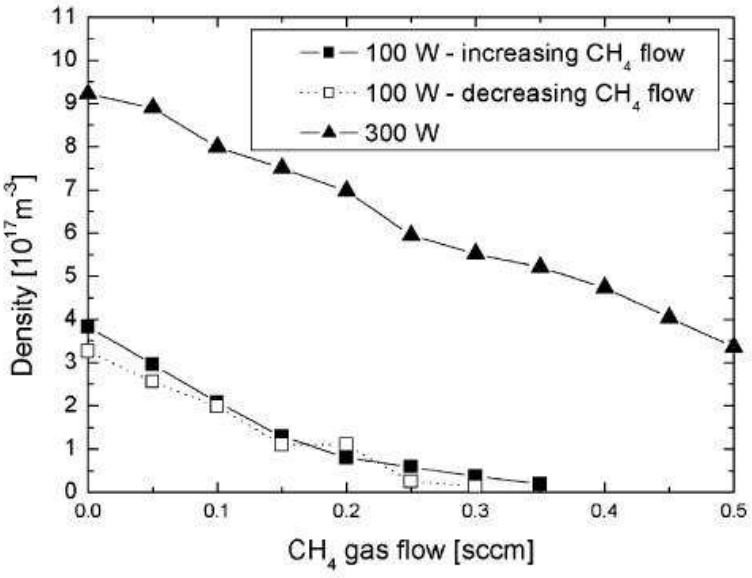

Figure 4.10: Measured Al atom density *versus* CH_4 admixture in pulsed mode for different power values. Working pressure was 3 Pa, Ar flow 10 sccm, pulsed timing: 0.23 ms (pulse) and 1.5 ms (pause).

It agrees with the above conclusion that for high power value the density of sputtered particles is not a simple linear function but displays some saturation effect.

4.2.2 Argon/Methane gas mixture

Figure (4.10) represents the measured Al atom density for argon/CH_4 gas mixture versus methane gas flow at constant argon gas flow of 10 sccm and constant working pressure 3 Pa in pulse mode for two different current values in the pulse. With the increasing methane gas flow the absorption signal significantly drops and once a critical value of methane gas flow is reached the absorption signal completely disappears. The same behavior can be observed in both dc mode and pulse mode. Reduction of methane gas flow (open symbols in figure (4.10)) leads to an increase of the absorption signal close to the previous curve for increasing methane gas flow (closed symbols) without the hysteresis behavior typical for

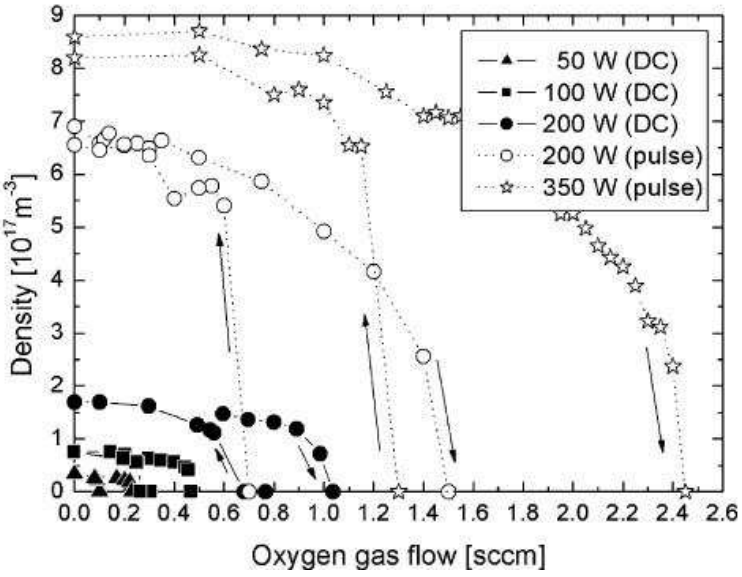

Figure 4.11: Measured Al atom density versus oxygen admixture in DC, and pulse modulated discharge for different values of power. Working pressure was 3 Pa. Arrows indicate order of measured points.

oxygen admixture (see below).

4.2.3 Argon/oxygen gas mixture

The Al density dependence versus oxygen gas flow for an argon/oxygen gas mixture is displayed in figure (4.11). The Ar gas flow was held at a constant value of 10 sccm; working gas pressure inside the chamber was 3 Pa. Curves represent powers of 50 W (dc), 100 W (dc), 200 W (dc), 200 W (pulse) and 350 W (pulse). In analogue to methane in the previous paragraph, a small admixture of oxygen leads to a significant decrease of the measured Al atom density and once a critical value of oxygen gas flow is reached the absorption signal completely disappears. At the same conditions, this critical value in case of pulse modulation is approximately 1.5 times higher than in dc mode. Reduction of the oxygen flow leads to a hysteresis-type dependence. For example at 350 W in pulse mode the absorption signal completely disappears at oxygen flow about 2.5 sccm. The Al signal reappears after the oxygen gas flow drops to a value of 1.3 sccm. Similar curves were

observed for all the other discharge powers. Difference between critical oxygen gas flow value in case of dc and pulsed modes can be explained by higher value of instantaneous current in the pulse.

Chapter 5

Dust formation and plasma behavior in hydrocarbon containing plasmas

In this chapter, we present an investigation of the growth dynamics of small molecules and of small carbon particles in radio frequency argon/methane, argon/acetylene, and argon/propene plasmas. Particular emphasis is put on the mass and energy distribution and the time dependence of forming molecules as well as Ar metastable density with respect to the formation of nano-size dust particles particularly in hydrocarbon-containing plasmas.

The experiments were performed in the PULVA 1 reactor. Energy dispersive mass spectrometry of positive plasma ions employing a Hiden plasma monitor (EQP 300) [84, 85] is mounted top down with its orifice 12 cm away from the powered electrode. The line averaged Ar metastable density was measured temporally resolved during the discharge by means of TDLAS system.

Dust particles in the discharge region are irradiated by a Nd:YVO_4 laser (Spectra Physics Millenia V) with a wavelength of 532 nm. Laser power is measured with a power meter (Spectra physics 407A). Scattered laser light is detected by a CCD camera (Teli CS8320BC) equipped with an interference filter to transmit the 532 nm laser light only. Pictures are recorded with a video recorder and stored on a personal computer.

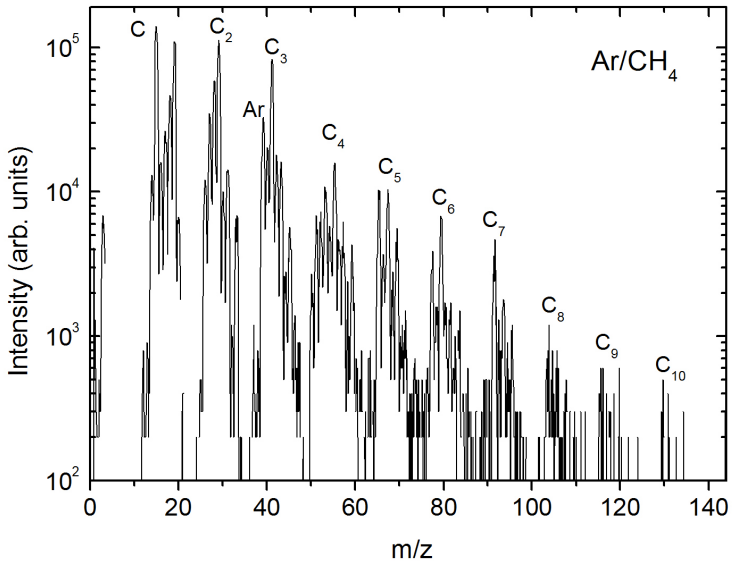

Figure 5.1: Ion mass spectra of Ar/CH_4 radio-frequency discharges. Ion energy 15 eV, discharge power 10 W, pressure 6 Pa.

5.1 Ion molecule formation in Ar/CH_4, Ar/C_2H_2 and Ar/C_3H_6 rf plasmas

5.1.1 Ion mass spectra

Typical ion mass spectra obtained for Ar/CH_4, N_2/CH_4, Ar/C_2H_2, and Ar/C_3H_6 radio-frequency discharges are displayed in figures (5.1) – (5.4).

Argon/Methane

The ion mass spectrum from Ar/CH_4 displays a large number of mass peaks (figure (5.1)) originating from fragmentation of methane (m/z = 14, 15), and from formation of larger $C_nH_m^+$ molecular ions, e.g, $C_2H_5^+$ (m/z = 29) and $C_3H_5^+$ (m/z = 41). The mass peak at m/z = 19 is attributed to formation of H_3O^+ ions. Rather large molecular ions containing up to 10 carbon atoms and an odd number of hydrogen atoms are detected, e.g., $C_5H_9^+$ (m/z = 69), $C_6H_7^+$ (m/z

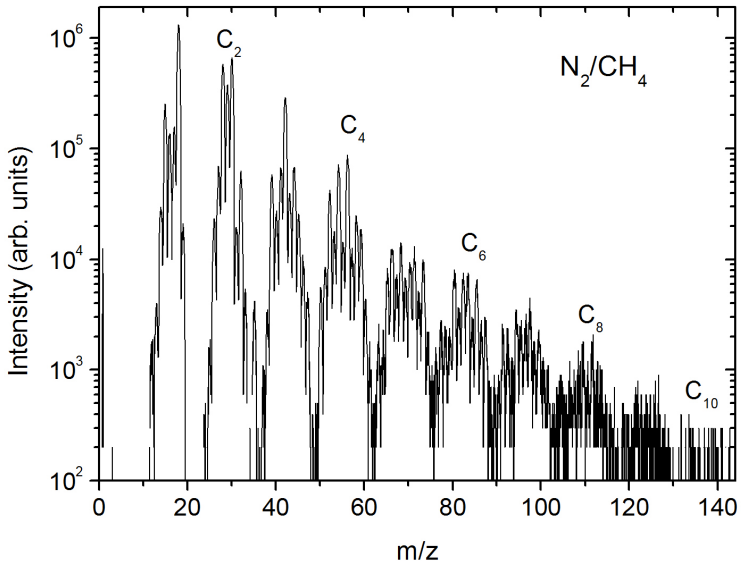

Figure 5.2: Ion mass spectra of N_2/CH_4 radio-frequency discharges. Ion energy 15 eV, discharge power 10 W, pressure 6 Pa.

= 79), $C_7H_7^+$ (m/z = 91), $C_8H_7^+$ (m/z = 103), and $C_9H_7^+$ (m/z = 115). There appears to be a tendency for the larger hydrocarbon ions to become more and more hydrogen-poor.

Nitrogen/Methane

The ion mass spectrum from N_2/CH_4 displays a large number of mass peaks originating from fragmentation of methane (m/z = 14,15) and formation of larger molecules (figure (5.2)). Distinct differences compared to Ar/CH_4 are to be noted. The grouping of peaks is less pronounced in N_2/CH_4 compared to Ar/CH_4 which presumably is due to the formation of nitrogen-containing molecules. Further support is provided by the pronounced appearance of even-numbered peaks in N_2/CH_4 compared to the preferentially odd-numbers peaks of Ar/CH_4 pointing to a replacement of e.g., a CH_2 group by a NH group. Formation of larger molecules is suppressed in N_2/CH_4 compared to Ar/CH_4, as can be noted from the C_{10} group that is barely observed in N_2/CH_4. For example, in Ar/CH_4 the intensity of the C_8 group is about two orders of magnitude smaller compared to

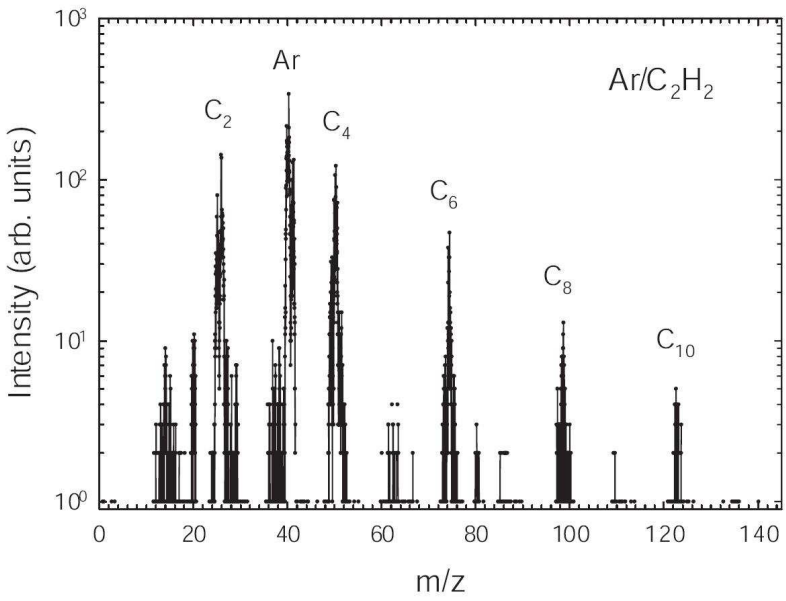

Figure 5.3: Ion mass spectra of Ar/C_2H_2 radio-frequency discharges. Ion energy 10 eV, discharge power 10 W, pressure 6 Pa.

the C_2 group while the difference amounts to four orders of magnitude in N_2/CH_4.

Argon/ Acetylene

The measured ion mass spectrum of Ar/C_2H_2 plasma is distinctly different from that of the Ar/CH_4 plasma, indicating some difficulty to break the carbon-carbon triple bond of acetylene (figure (5.3)). Hydrocarbon molecules in acetylene plasmas, hence, prefer to grow by addition of C_2-containing molecules as the presence of hydrocarbon molecular ions with even numbers of carbon atoms is much more prominent than with odd numbers. The observed ions are extremely hydrogen-poor, e.g., $C_6H_3^+$ (m/z = 79) or $C_8H_3^+$ (m/z = 99).

Argon/ Propylene

The ion mass spectrum from Ar/C_3H_6 plasma displays the richest number of mass peaks (Figure (5.4)). Molecular ions containing up to 12 carbon atoms are detected. The most prominent mass peaks are attributed to $C_3H_3^+$ (m/z = 39), $C_3H_5^+$ (m/z = 41), and $C_3H_7^+$ (m/z = 43). In comparison to the Ar/CH_4 plasma, higher mass peaks are more likely and there is also a larger chance for

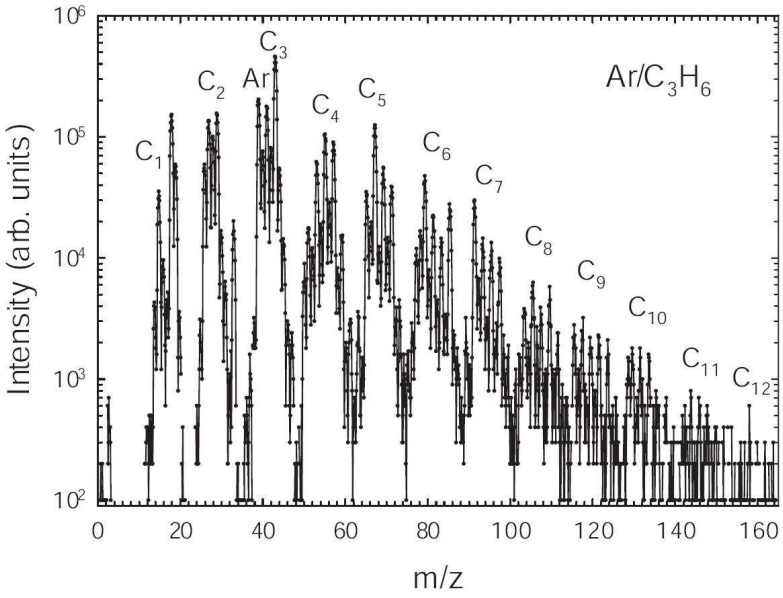

Figure 5.4: Ion mass spectra of Ar/C_3H_6 radio-frequency discharges. Ion energy 15 eV, discharge power 10 W, pressure 6 Pa.

such molecules to contain an even larger number of hydrogen atoms.

5.1.2 Ion energy distribution

The energy distribution of plasma ions in a radio-frequency discharge was investigated for Ar/CH_4, Ar/C_2H_2, and Ar/C_3H_6 gas mixtures. Figure (5.5) and (5.6) shows a sequence of energy distributions in Ar at different admixtures of CH_4, C_2H_2, or C_3H_6 at typical gas pressures of 4 – 9 Pa. The energy distributions of $C_xH_y{}^+$ hydrocarbon ions display pronounced maxima at high energies reflecting the plasma potential respectively the voltage drop between plasma and grounded electrode of the plasma process monitor. The energy distributions of Ar^+ ions display a double peak structure with maxima at small and large kinetic energies. With increasing pressure the low-energy peak increases while the high-energy disappears. Under the present experimental conditions, and taking into account the resonantly enhanced charge transfer ($Ar^+ + Ar \rightarrow Ar + Ar^+$) having a cross section of ~ 100 Å^2 [86], the mean free path for charge changing collisions is $\approx$

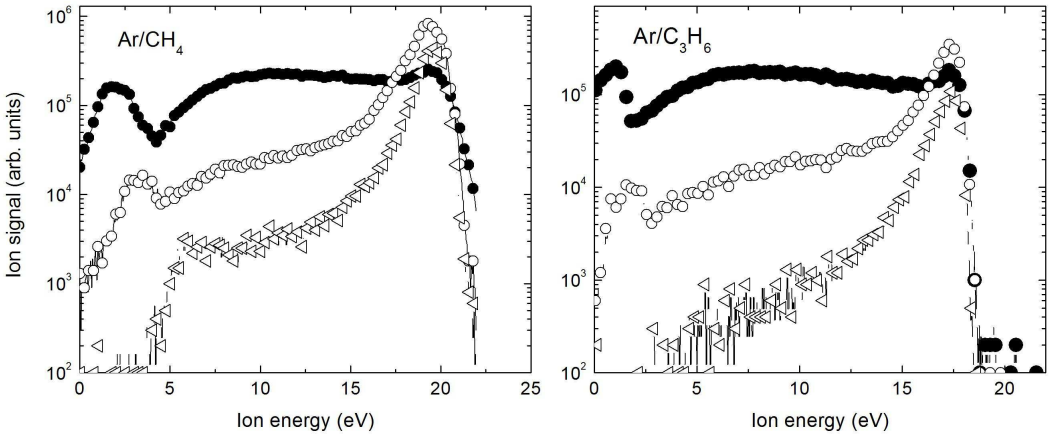

Figure 5.5: Ion energy distribution of Ar/CH_4 (left: • Ar^+, ○ $CH_3{}^+$, ◁ $C_2H_5{}^+$), and Ar/C_3H_6 (right: • Ar^+, ○ $C_3H_5{}^+$, ◁ $C_4H_7{}^+$) radio-frequency discharge. Discharge power 10 W, argon gas flow 4 sccm, hydrocarbon (Ar/CH_4, and Ar/C_3H_6) gas flow 1.5 sccm, total pressure 4 Pa (Ar/CH_4), and 3.6 Pa (Ar/C_3H_6).

0.1 cm. Thus, with increasing gas pressure a rapid neutralization of fast Ar^+ ions occurs and preferentially slow Ar^+ ions are detected. Charge changing collisions are of minor importance for $C_xH_y{}^+$ hydrocarbon ions as the relevant cross sections and/or the density of neutral C_xH_y molecules are significantly smaller.

Comparing the ion distributions from different gas mixtures we note that Ar/C_2H_2 produces energies up to 36 eV which is much larger than in Ar/CH_4 and Ar/C_3H_6. No simple explanation for this different behavior has been found yet. Obviously, the plasma potential is much larger in Ar/C_2H_2 compared to the other gas mixtures. As a possible explanation we mention the pronounced tendency of dust particle formation in Ar/C_2H_2 plasmas.

As we shall see later (chapter (7)), the growing dust particles by capture of electrons cause a higher electron temperature and thus an enhancement of the plasma potential [87].

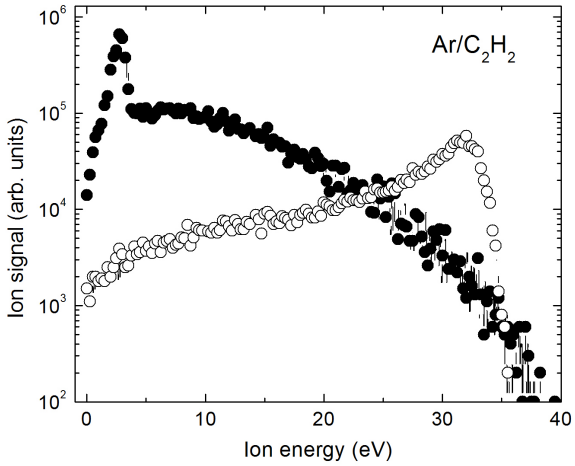

Figure 5.6: Ion energy distribution of Ar/C_2H_2 (• Ar^+, ∘ $C_2H_2{}^+$) radio-frequency discharge. Discharge power 10 W, argon gas flow 4 sccm, hydrocarbon (Ar/C_2H_2) gas flow 1.5 sccm, total pressure 9 Pa.

5.2 Dust particle formation and plasma behavior

5.2.1 Dust particle formation

Dust particle formation is investigated by shining a laser into the plasma and by observation of the transmitted and scattered laser light. In addition, dust particles are recorded with the help of a CCD camera placed at right angles to the laser beam. As a general trend, particle formation is more likely in Ar/C_2H_2 than in Ar/CH_4 plasmas, as was noted before by *Hong et.al.* [88]. In the argon/acetylene plasma a large amount of dust particles is effectively and continuously created and a large amount of small carbon dust particles ($\sim$ 100 nm) levitated inside the plasma by the action of electrostatic, ion drag and neutral drag forces can be observed. Dust particle size and density can reach large values resulting in a recognizable decrease of transmitted and a remarkable increase of scattered laser light. A dust void is subsequently formed in the center of the dust cloud due to the ion drag force which becomes significant once the dust particles reach a

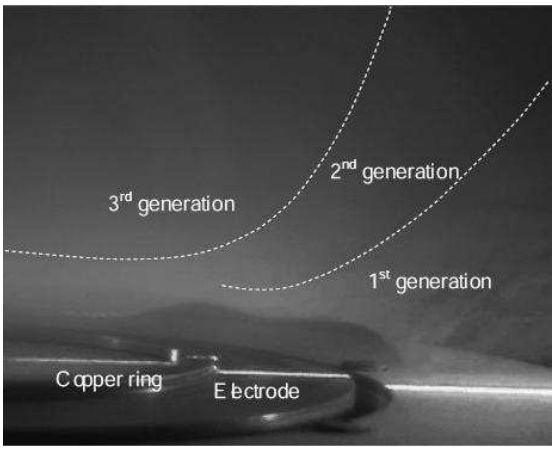

Figure 5.7: Dust formation in Ar/C_2H_2 radio-frequency plasma. Boundaries between first and second and second and third dust generations are indicated.

critical size (figure (5.7)). Meanwhile a new dust generation forms in the free space. The new generation grows both in size and number density until it is also pushed out due to ion drag forces and the void re-appears. In figure (5.7), a third particle generation is already growing inside the void of the second one while the first one still exists.

In order to quantify the temporal behavior of dust particle formation inside the plasma, the intensity of transmitted laser light through an argon/acetylene plasma was measured. Figure (5.8) displays the time dependence of transmitted laser intensity for different discharge powers. The pronounced decrease of the transmitted laser intensity due to the efficient dust particle formation is followed by a more or less pronounced periodical variation. After switching off the acetylene supply, the transmitted light intensity slowly partly resumes to its original value indicating a decreasing particle density.

The observed oscillation of dust particle density may be understood on the following grounds. Right at the beginning of a cycle, small molecules start growing into larger molecules by molecule attachment and ultimately into small particles as is inferred from the decreasing intensity of transmitted and the increasing intensity of scattered laser light. The growing particles lead to a rapid depletion of small molecules and particle growth eventually comes to an end. The grown particles

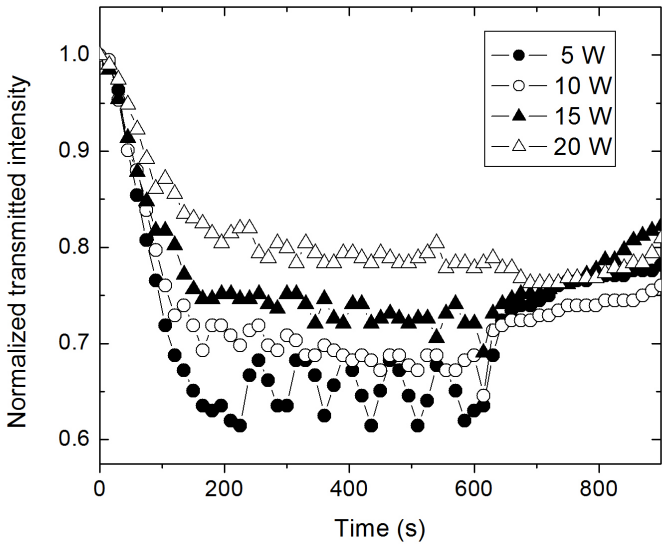

Figure 5.8: Transmitted laser intensity Time dependence of dust particle formation in Ar/C_2H_2 rf plasma.

are subsequently expelled from the center of the plasma by ion and neutral drag forces and a more or less particle-free void appears. Depletion of small molecules now also comes to an end and a new cycle can start. The oscillatory behavior can be seen in figures (5.8) and (5.2.1).

5.2.2 Time evolution of molecular ion formation

Some support for the above explanation of dust particle density oscillation is provided by the temporal behavior of small molecular ions in plasmas. Due to experimental limitations, e.g., a rapid closing of the entrance orifice of the plasma process monitor with a thick hydrocarbon layer, it was necessary to carry out these experiments in Ar/CH_4 rather that in Ar/C_2H_2 plasma. A pronounced temporal density variation of $C_xH_y{}^+$ (m/z = 15, 29, 41, 55, 67, and 79, identified as CH_3^+, $C_2H_5^+$, $C_3H_5^+$, $C_4H_7^+$, $C_5H_7^+$, and $C_6H_7^+$) ions formed within the plasma is observed which may provide information on the nucleation and growth processes

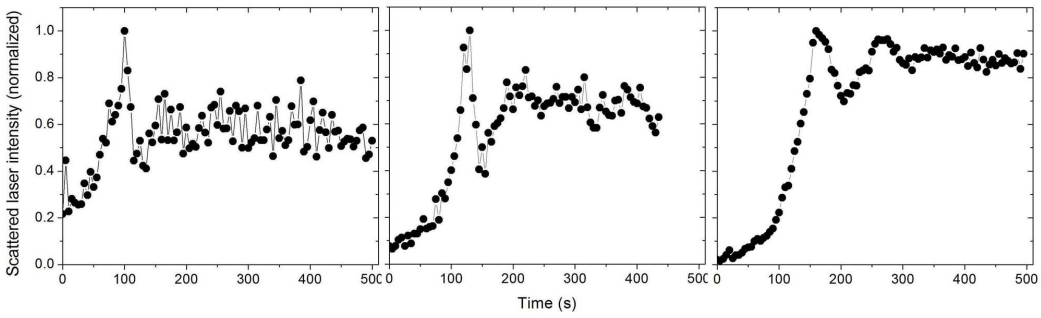

Figure 5.9: Scattered laser intensity at different positions in the dust cloud: center (left), 4 cm (middle), and 8 cm (right) away from the center in Ar/C_2H_2 radio-frequency plasma.

of larger molecules and of dust particles (figure (5.10)).

Dominating reactions are $CH_x{}^+$ (x = 1, 2, 3) ion formation in single collisions with methane molecules, e.g.,

$$e^- + CH_4 \rightarrow CH_3^+ + H + e^- \tag{5.1}$$

As a consequence, the formation rate of $CH_x{}^+$ molecular ions does not vary in time since the methane density is kept constant. The formed $CH_x{}^+$ ions further react with CH_4 to form $C_2H_5{}^+$ ions, e.g,

$$CH_3^+ + CH_4 \rightarrow C_2H_5^+ + H_2 \tag{5.2}$$

$C_2H_5{}^+$ ions again react with CH_4 to form still larger molecules, e.g.,

$$C_2H_5^+ + CH_4 \rightarrow C_3H_7^+ + H_2 \tag{5.3}$$

and so forth. Although it is not quite clear how dust particles exactly form and what role is played by negatively charged molecular ions like C_2H^- [88, 89], the forming dust particles will continue to grow by molecule attachment and eventually will become negatively charged once a critical size is exceeded. In order to explain the observed time variation of small molecular ions one may take into con-

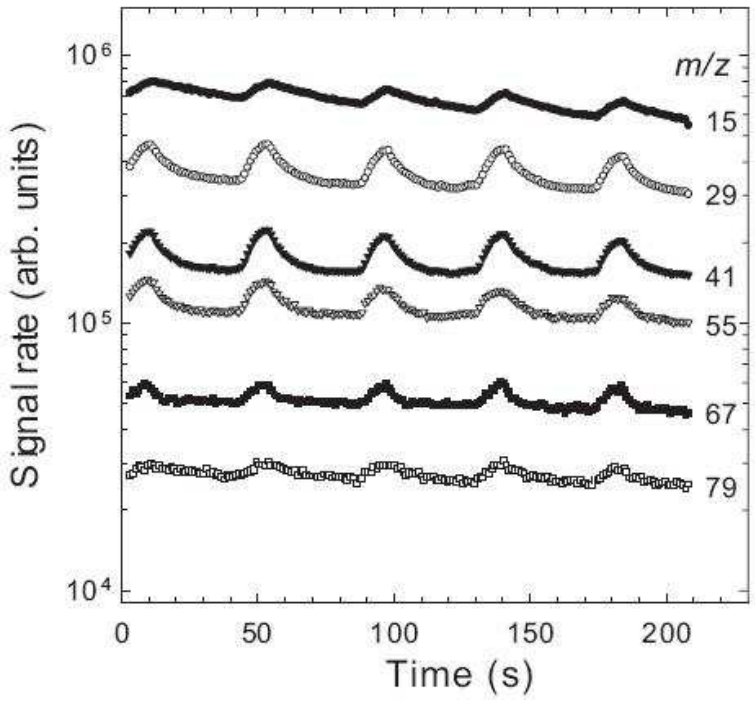

Figure 5.10: Time dependence of indicated ion mass peaks (m/z = 15, 29, 41, 55, 67, 79) in a Ar/CH_4 radio-frequency plasma. Ion energy 15 eV, discharge power 10 W, pressure 6 Pa.

sideration two enhancement effects: a negatively charged dust particle providing an enhanced attachment cross section for positively charged ions, and, eventually more important, an enhanced cross section due to the larger surface size of the growing dust particles. Both effects will lead to the observed depletion of small molecules. The rate coefficients depend on the size of the dust particle which grows with time by molecule and molecule ion attachment. The rate equation for, e.g., CH_3^+ ions thus may be written as:

$$\frac{dn_M}{dt} = c_1 - c_2 n_M - c_3 n_M n_d S_d \tag{5.4}$$

where n_M is the density of the considered molecule ion, n_d and S_d dust particle density and surface size, respectively, which both depend on time, and where the c_i ($i = 1 - 3$) are reaction coefficients. There first term describes the formation of

CH_3^+ according to reaction (5.1), the second term its loss according to reaction (5.2) or other reactions, while the last term describes the loss of CH_3^+ ions due to the growing dust particles. For simplicity, we may further assume a linear dependence of the product $n_d S_d$ with time t ($n_d S_d = a_1 t$). Equation (5.4) can be simplified to:

$$\frac{dy}{dt} + (a + bt)y = c \tag{5.5}$$

where $y \equiv n_M$, $a = c_2$, $b = a_1 c_3 \cdot n_M$, and $c = c_1$.

Equation (5.5) is nothing else than a first order linear differential equation which has general solution:

$$y = \frac{\int c \cdot u(t)dt + d}{u(t)} \tag{5.6}$$

where $u(t) = exp\left\{\int (a + bt)dx\right\}$. A preliminary evaluation of equation (5.6) yields a reasonable agreement with experiment.

5.2.3 Time evolution of metastable density

Metastable density is an important plasma parameter, since metastable atoms are abundant and energetic. Similar to small molecular ions [36], the temporal behavior of metastable density also follows the periodic variation of the plasma as well as particle density and size. As can be seen in figure (5.11), the metastable density drops instantly when C_2H_2 is inserted due to the reactions between metastable atom and processing gas producing reactive radicals that ignite the neutral growth channel for dust particles [90]:

$$C_2H_2 + Ar^* \rightarrow C_2H + H + Ar \tag{5.7}$$

$$C_2H + Ar^* \rightarrow C_2 + H + Ar \tag{5.8}$$

The formed radicals further react with C_2H_2 to form larger radicals e.g,

$$C_2H + C_2H_2 \rightarrow C_4H + H_2 \tag{5.9}$$

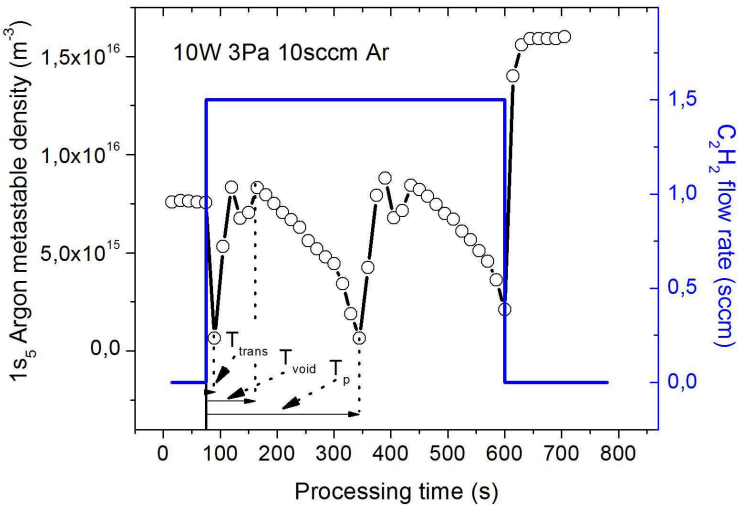

Figure 5.11: Time evolvement of metastable density in the processing plasma. The change of metastable density is the indication for the change of plasma parameters, especially the dust density and size.

and

$$C_2 + C_2H_2 \rightarrow C_4 + H_2 \tag{5.10}$$

and so forth. Shortly after the acetylene flow is added the metastable density drastically increases indicating the change in plasma mode namely a $\alpha - \gamma$' transition. The appearance of a dust void leads to a separation of the plasma into a dust-free plasma inside the void with low metastable density and a dusty plasma with high metastable density outside. Therefore the metastable density slightly decreases as the void starts to expand. At the end of the dust growth period when the outer dust cloud is pushed away the metastable density drastically drops again (figure (5.11)).

As explained above, the metastable density follows the time evolvement of the dust growth in processing plasma. From the temporal behavior of metastable density we can easily define the time periods T_{trans}, T_{void}, and T_p (see figure (5.11)). The metastable density can be used as an indicator for changes in the

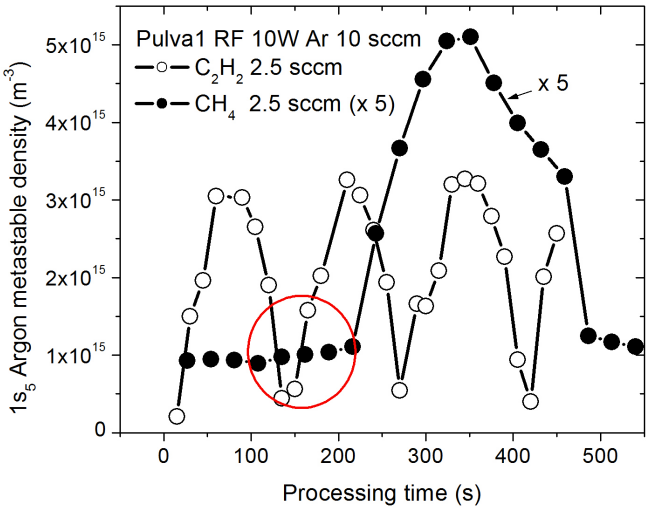

Figure 5.12: Time evolvement of metastable density in Ar/C_2H_2 (○) and in Ar/CH_4 (●) rf plasmas. The dust productivity of Ar/C_2H_2 plasma is higher than Ar/CH_4 plasma as the dust growth period is much shorter in Ar/C_2H_2 plasma ($T_p = 130$ s) compared to Ar/CH_4 plasma ($T_p = 540$ s).

plasma, especially electron temperature and density as well as to trace the phase transitions in processing plasma between nucleation, agglomeration, accretion, and dust expelling phases.

The dust productivity of Ar/C_2H_2 plasma is so high that only slow phases like accretion and dust expelling phases can be seen. In order to get insight into the nucleation phase, the Ar/CH_4 rf plasma was employed to enlarge T_{trans}. In the nucleation phase there exists a period where the metastable density only slightly increases (marked by a circle in figure (5.12)), implying a slight rise of electron temperature. This change in electron temperature can be explained by the appearance and growth of negative ions in this plasma. The dust growth process therefore can be associated with the growth of negative hydrocarbon ions.

In order to understand dust growth and the role of metastable atoms in processing plasma, the investigations of metastable density depending on the dust

particle influence is therefore highly demanded. Results from these studies will be presented in the following chapters which focus on the interactions between dust particles and metastable atoms in dusty plasma as well as the influence of dust particles on metastable density.

Chapter 6

Interaction of metastable atoms with injected particles.

Energetic metastables are involved in the particle surface modification process. So far, role and effects of metastables in dusty plasmas are not considered in a large extent. Few years ago, *Graves* and his coworkers has measured the dust particle surface temperature and proposed a model to explain the result but the heating channel by metastable was not taken into account [91]. There exists a lack in consideration of theses species in such plasma environment.

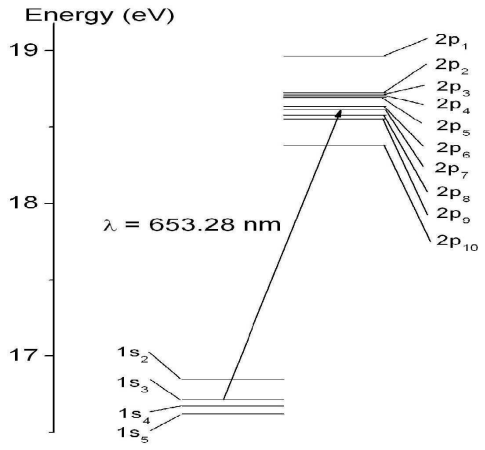

Figure 6.1: Neon term diagram of the 1s and 2p levels (in Paschen's notation). Values were taken from NIST data base

In this chapter we present results for a dusty plasma where the dust particles (silicon dioxide, 10 μm diameter) are injected from outside into the plasma. Neon was used as working gas. By the combined action of electrostatic and gravitational forces, the particles are trapped in the plasma sheath adjacent to the glow [92]. The radii of the confined dust clouds R_c are about 3 cm and 5 cm

for the 4 cm and the 6 cm ring, respectively. With the larger confining ring it is possible to capture a larger dust cloud with a higher dust density. Therefore, the effect of dust particles on the metastable atom density can be enhanced and becomes easier to observe.

The density and temperature of Ne ($1s_3$) metastable atoms (figure (6.1)) are measured by means of TDLAS in both pristine and dusty plasmas with injected SiO_2 micro-particles. A relatively small number of particles is confined in the sheath region in front of the powered electrode. The effect of dust particles on the plasma parameters (electron density and temperature) is negligible since the particles are situated outside the plasma and their density is relatively small.

In order to account for the isotope effect, the transmitted photodiode signal was fitted with a sum of two Doppler line profiles for the ^{20}Ne and ^{22}Ne components (see figure (6.2)),

$$\begin{aligned} I(\nu) &= (a + b\nu + c\nu^2)\exp\{-\kappa_0 l \exp\left[-\left(\frac{\nu-\nu_0}{0.6\Delta\nu}\right)^2\right] \\ &- \frac{\kappa_0 l}{9.326}\exp\left[-\left(\frac{\nu-\nu_0-\nu_{iso}}{0.572\Delta\nu}\right)^2\right]\} \end{aligned} \tag{6.1}$$

The parameters a, b, and c represent the baseline of the signal, i.e. the transmitted signal without plasma, approximated by a second order polynomial. ν_0 is the central frequency, taken as a free fit parameter, $\Delta\nu_{iso}$ is the isotope shift of the ^{22}Ne component.

6.1 Plasma characterization

6.1.1 Spatial distribution of metastable atom density and temperature

The Ne metastable atom density in PULVA1 was observed to be radially and axially inhomogeneous. Typical values are a few 10^{15} m^{-3} in the bulk and some 10^{14}

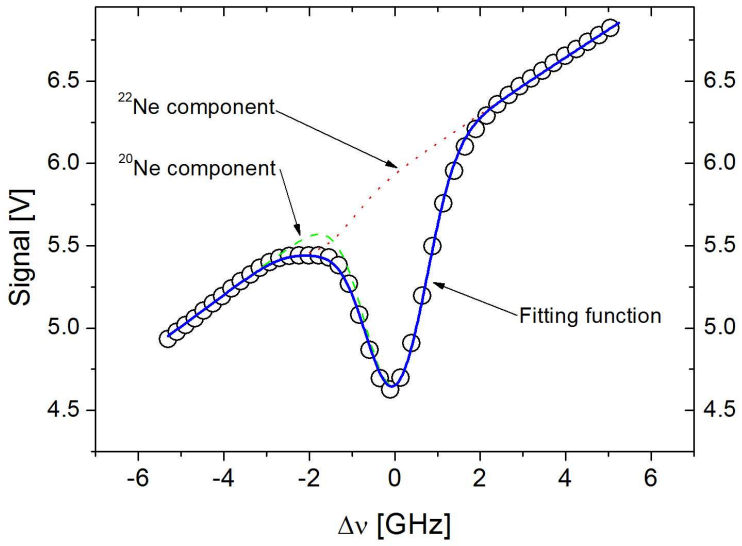

Figure 6.2: Sample of absorption profile and least-squares fit to this data.

m^{-3} in the plasma sheath. The radial distribution can be fitted by a Gaussian profile giving a full width at half maximum $w \sim 14$ cm (figure (6.3)). The axial density increases almost linearly from electrode to plasma bulk. The density gradually decreases toward the chamber wall. By comparing the axial distributions of neon metastable density at different pressures, we can clearly observe the expansion of the plasma sheath with decreasing plasma pressure (figure (6.4)) [93]. The gas temperature is, however, nearly constant in the entire plasma with a value of about 380 K, apart from a small increase of about 10 K near rf electrode.

Assuming that the metastable density distribution follows a Gaussian profile and accounting for the fact that the plasma is radially symmetric, the metastable density $n_m(x, y, z)$ at normalized coordinates x, y and z can be written as

$$n_m(x, y, z) = n_m(x, 0, 0) \exp\left(-\frac{y^2 + z^2}{2\sigma^2}\right) \tag{6.2}$$

where σ is related to the full width at half maximum w of the Gaussian distribution by

$$w = 2\sqrt{2 \ln 2}\, \sigma\,. \tag{6.3}$$

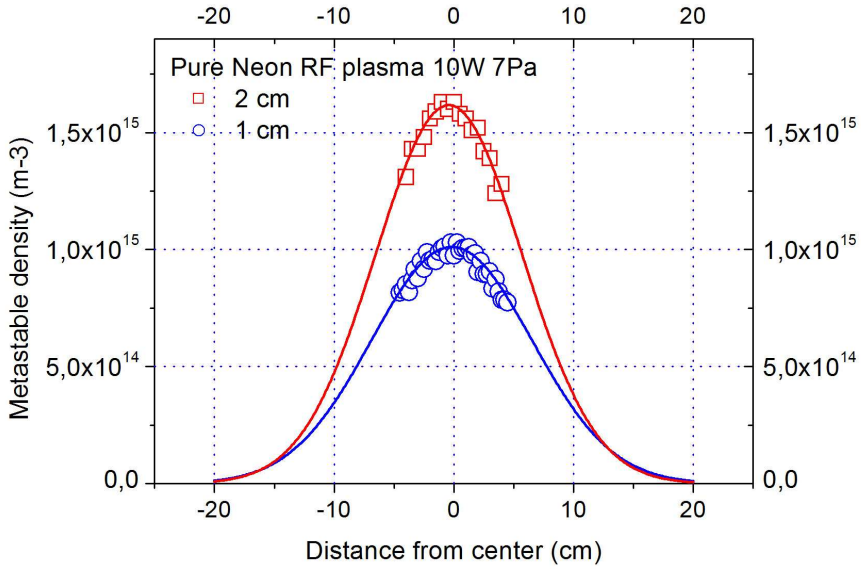

Figure 6.3: Measured radial distribution of neon metastable density and their Gaussian fits for two distances above the electrode.

The measured density at height x above the electrode and distance z from the plasma center $n_m(x,z)$, therefore, is equal to:

$$n_m(x,z) = n_m(x,0)\exp\left(-\frac{z^2}{2\sigma^2}\right) \tag{6.4}$$

where $n_m(x,0)$ is the measured metastable density in the center at height x. Since $\sigma < R_r$, we get

$$\int_{-R_r}^{+R_r} \exp(-\frac{y^2}{2\sigma^2})dy \approx \int_{-\infty}^{+\infty} \exp(-\frac{y^2}{2\sigma^2})dy = \sigma\sqrt{2\pi}, \tag{6.5}$$

where R_r is the chamber radius.

Combining the radial distribution of the metastable density (equation (6.4)) with the measured axial distribution $n_m(x)$, the spatial density distribution of the metastable atoms can be written as:

$$n_m(x,y,z) = \frac{2R_r n_m(x)}{\sigma\sqrt{2\pi}}\exp\left(-\frac{y^2+z^2}{2\sigma^2}\right) \tag{6.6}$$

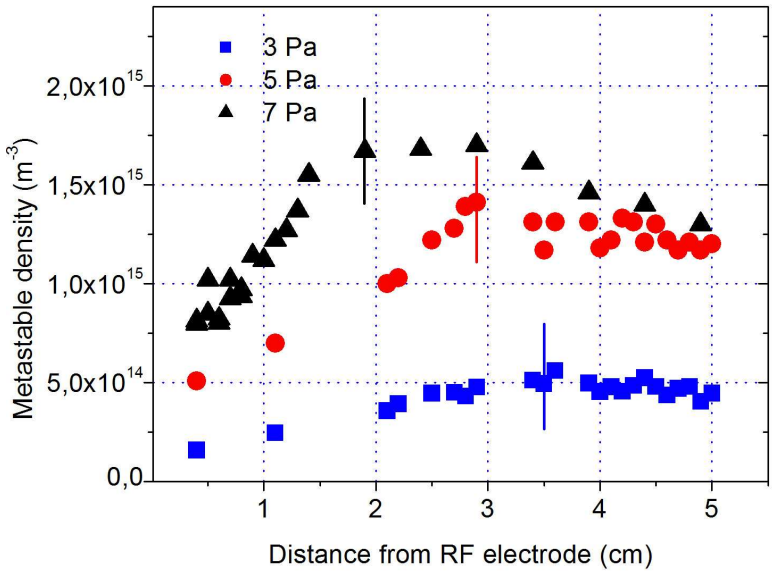

Figure 6.4: Axial distribution of neon metastable density at different pressures. The lines indicate the sheath boundaries.

The diffusive flow of metastable atoms in the plasma sheath deduced from the spatial distribution of metastable density is dominated by the flow towards the electrode, since the sheath length (about 1.5 cm) is much smaller than the width of the Gaussian distribution in y and z directions (about 14 cm).

6.1.2 Dependence of metastable density and temperature on plasma conditions

Neon metastable density and temperature were also characterized in relation with plasma power and gas pressure. The metastable atom density increases significantly with plasma power. This increase is more pronounced in the plasma center compared to the plasma sheath. At 7 Pa, it readily reaches a plateau of about 2.8×10^{15} m^{-3} (at 40 W power-input in plasma bulk), while it is still increasing in the sheath region.

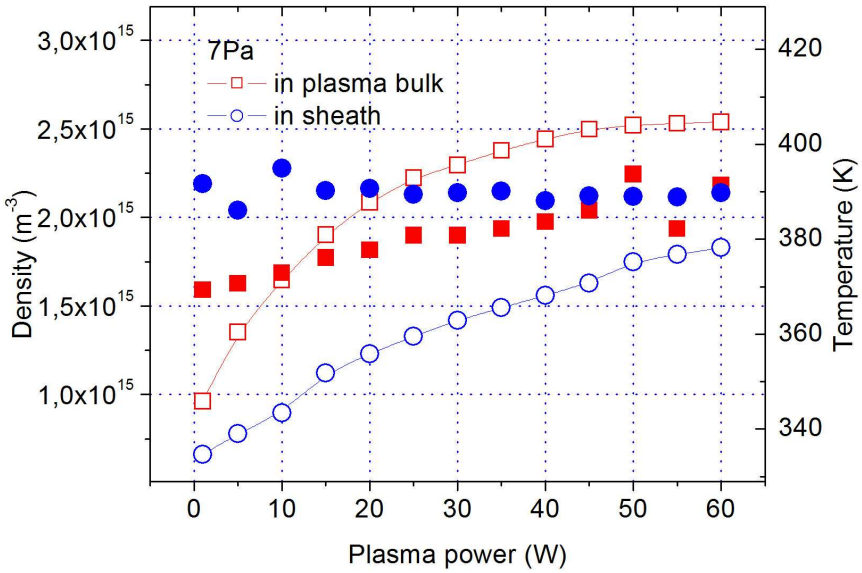

Figure 6.5: Dependences of neon metastabble density and temperature on plasma power. Full circles and squares represent the temperature, open circles and squares represent the density.

The temperature does not change significantly with plasma power, e.g., it increases from 370 K to 390 K in the plasma glow while it remains approximately constant in the plasma sheath (figure (6.5)). In the examined pressure range (2 – 10 Pa), the density of electrons which are responsible for the formation of metastable atoms increases with increasing pressure [94] and the metastable atom density, hence, also increases with pressure (figure (6.6)). The metastable atom temperature remains largely unaffected by a pressure increase.

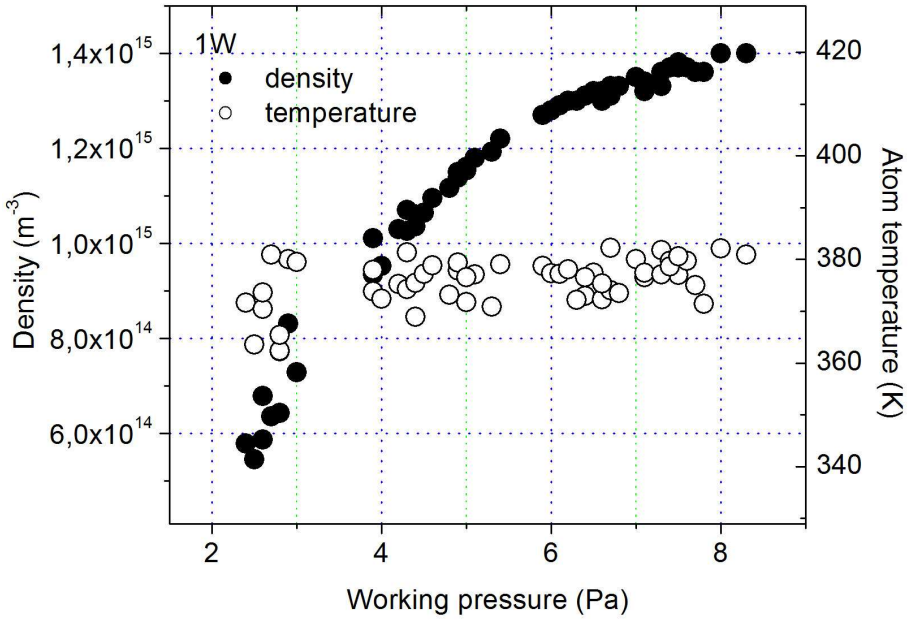

Figure 6.6: Dependences of neon metastabble density and temperature on gas pressure.

6.2 Influence of injected dust on metastable atom density

6.2.1 Quenching effect

The spatial distribution of metastable atoms in a dust-containing plasma was measured and compared to that of pristine plasmas under the same plasma conditions. It is believed that the metastable density in dusty plasma is higher in comparison to a pristine plasma [95]. However, when the dust density is low and the dust surface is large which is the case in the present work, the loss effect overcompensates the enhancement resulting in a lower metastable density in dusty plasmas. The line integrated metastable atom density within the dust cloud drops significantly (0.5×10^{14} m^{-3} for the small ring and 3.5×10^{14} m^{-3} for the large ring) in comparison to that of dust-free plasma at the same conditions

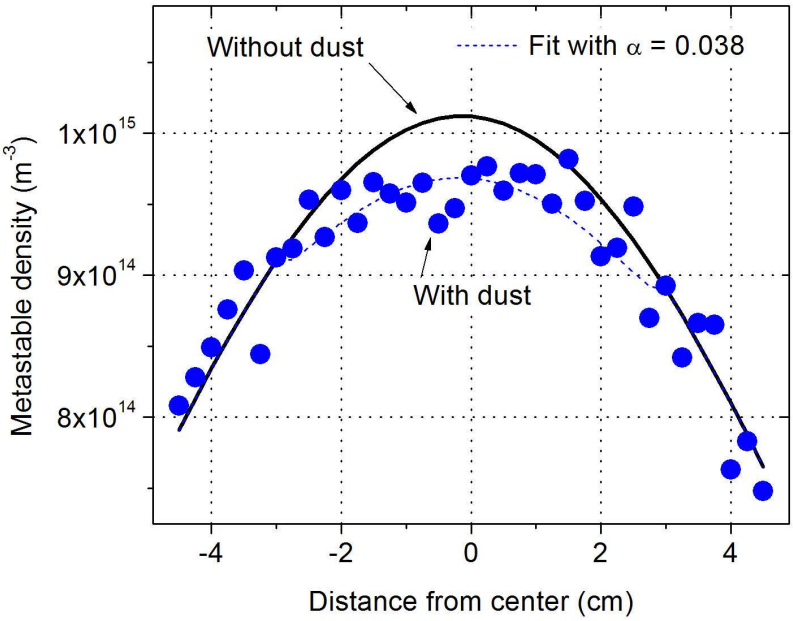

Figure 6.7: Radial Neon metastabble density of dusty plasma compared to that of pristine plasma at the same conditions and locations with small ring.

and positions (figure (6.7) and (6.8)).

The decreasing metastable atom (Ne*) density provides evidence for a significant interaction between metastable atoms and particles. The micro-particles act as quenching agents in the energy transfer process:

$$\mathrm{Ne}^* + \mathrm{particle} \rightarrow \mathrm{Ne} + \mathrm{particle(heated)} \tag{6.7}$$

Metastable atoms which carry an internal energy of about 16.715 eV should thus play a considerable role in the heating of dust particles confined by a plasma.

Considering a simple corona model, metastable atoms are generated by direct excitation of ground state neon atoms by impact of energetic electrons and are lost by diffusion to the electrodes and to the dust particles. The de-excitation of metastable in collision with cold electron is neglected since the electron density in the plasma sheath is small. The density of metastable atoms within the dust

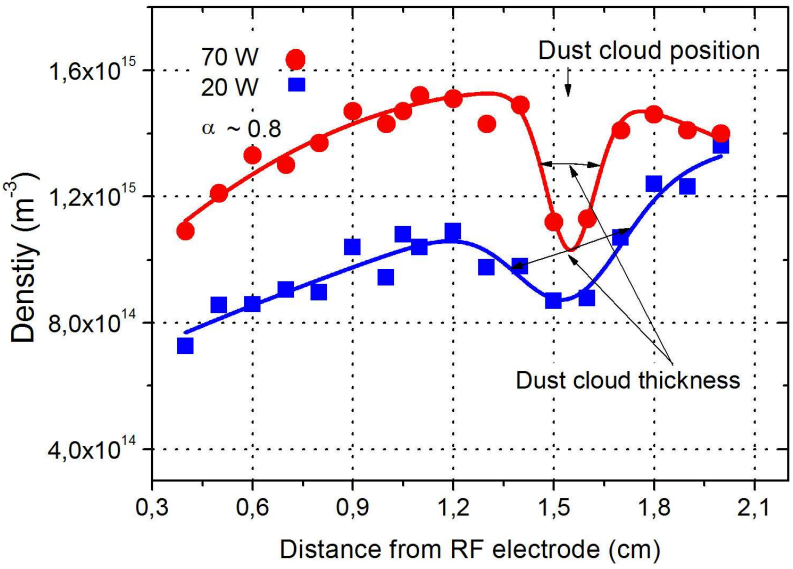

Figure 6.8: Axial Neon metastable density of dusty plasma with 6 cm ring.

cloud is therefore given by the relation:

$$\frac{\partial n_m(x,y,z)}{\partial t} = k_m n_0 n_e - \frac{2D_m}{l_{eff}^2} n_m(x,y,z) - \frac{2D_m}{l_D^2} n_m(x,y,z) \qquad (6.8)$$

Here n_0 and n_m are ground state and metastable state density, respectively, of neon atoms, n_e is the electron density, and k_m is the rate coefficient for electron impact excitation from the ground state to the metastable state. The second and third terms on the right hand side of equation (6.8) are the losses by diffusion to the chamber wall and to dust particles, respectively, with corresponding effective lengths l_{eff} and l_D, where D_m is the diffusion coefficient of metastable neon atoms in neon ground state atoms. The ground state atom density is approximately equal to the neutral gas density of neon and thus independent of the presence of particles.

For a dust-free plasma, the loss of metastable atoms by diffusion in the plasma sheath is dominated by the flow toward the electrode. Hence, the sheath length l_{sh} can reasonably be used as the effective length.

For a dust particle-containing plasma an additional loss of metastable atoms at the surface of particles occurs; the effective length is

$$l_D = \frac{V}{S} = \frac{N_d/n_d}{N_d S_d} = \frac{1}{n_d S_d} \tag{6.9}$$

where V is dust cloud volume, S is total dust surface area, N_d is total number of dust particles in the dust cloud, n_d is the dust density and S_d the surface area of one particle, respectively.

With this approach we obtain the following relation between the steady state density in the plasma sheath for the cases with (n_m^D) and without dust particles (n_m):

$$n_m^D(x,y,z) = \frac{1}{1+\alpha} n_m(x,y,z) \tag{6.10}$$

with

$$\alpha^{1/2} = l_{eff}/l_D = l_{sh} n_d S_d \tag{6.11}$$

The so-called quenching factor α accounts for the loss of metastable atoms due to the presence of dust particles; it becomes zero for a dust-free plasma, e.g. outside the dust particle cloud.

The quenching factor is estimated from the measured radial distributions in dust-free ($n_m(x,z)$) and dust-containing ($n_m^D(x,z)$) plasmas, together with the radius of the dust cloud R_c. The measured metastable density in the presence of dust particles can be written as:

$$\begin{aligned} n_m^D(x,z) &= \int_{-R_r}^{+R_r} n_m(x,y,z)dy - \int_{-\sqrt{R_c^2-z^2}}^{+\sqrt{R_c^2-z^2}} \{n_m(x,y,z) - n_m^D(x,y,z)\}dy \\ &= n_m(x,z) - \frac{\alpha}{1+\alpha} n_m(x,0) \exp\left(-\frac{z^2}{2\sigma^2}\right) \int_{-\sqrt{R_c^2-z^2}}^{+\sqrt{R_c^2-z^2}} \exp\left(-\frac{y^2}{2\sigma^2}\right)dy \\ &= n_m(x,z) - \frac{\alpha}{1+\alpha} K(z) n_m(x,0) \end{aligned} \tag{6.12}$$

The quenching factor is expressed as:

$$\alpha = \frac{\Delta n_m(x,z)}{K(z) n_m(x,0) - \Delta n_m(x,z)} \tag{6.13}$$

where $\Delta n_m(x,z) = n_m(x,z) - n_m^D(x,z)$ is the difference of measured metastable densities between dusty and dust-free plasma.

Since R_c is smaller than σ, we can use the following approximation for $K(z)$:

$$K(z) \approx \frac{1}{\sigma}\sqrt{\frac{2}{\pi}}\sqrt{R_c^2 - z^2}\left[\exp(-\frac{R_c^2 - z^2}{2\sigma^2}) + 1\right] \tag{6.14}$$

At different position within the dust cloud the calculated results give almost the same value of $\alpha = 0.038$ for neon dusty plasma of 10 W rf power, 7 Pa gas pressure and with 4 cm radius confining ring (figure (6.7)). In our experiments, l_{sh} is estimated from the axial distribution of metastable density of about 1.5 cm and S_d equals to 3.14×10^{-10} m^2 for 10 μm dust particles. The dust density n_d is, therefore, about 4.14×10^{10} m^{-3} which corresponds to 42 particles per cubic millimeter.

However, with increasing plasma power, the dust cloud thickness decreases due to the increase of wakefield attraction force [27] which compresses the dust cloud in x direction. The increase of the quenching factor is in agreement with the decreasing dust cloud thickness which is associated with an increasing dust particle density (figure (6.9)). The dust cloud thickness is deduced from the axial distribution of metastable density in the presence of dust particles (figure (6.8)). The estimated dust density using the calculated α (equation (6.11)) increases from 200 to 440 particles per cubic millimeter.

6.2.2 Particle heating by metastable atoms

In order to calculate the particle heating by metastable atoms, the metastable density n_m^D around the dust particles should be known. This quantity is calculated from equation (6.10) using the radial distribution of pristine plasma together with the quenching factor. Assuming the energy transfer probability of metastable to be unity, the power per unit area absorbed by dust particles due to the collision of metastable atoms with the dust particle surface P_m [96, 97] can be written as:

$$P_m = 0.25\varepsilon n_m^D(x,y,z)\sqrt{\frac{8k_BT}{\pi m_a}} = 0.25\varepsilon\frac{1}{1+\alpha}n_m^D(x,y,z)\sqrt{\frac{8k_BT}{\pi m_a}} \tag{6.15}$$

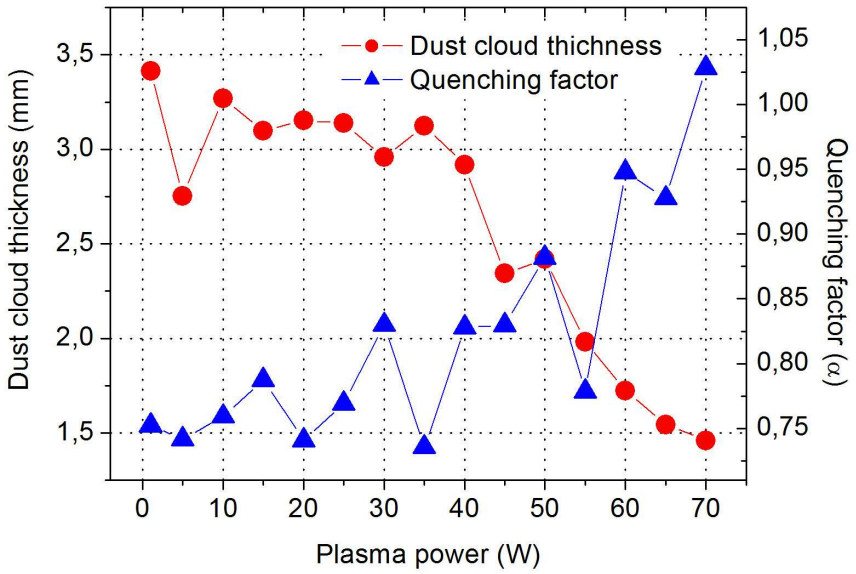

Figure 6.9: Quenching factor and corresponding dust cloud thickness with confining ring of 6 cm radius at different plasma power.

where ε is energy of the metastable level (16.715 eV for level $1s_3$ of Neon). At 10 W plasma power, within the dust cloud n_m is of the order of 2.66×10^{15} m^{-3} and T is of the order of 380 K, thus the energy influx is 0.04 W/m^2 in case of the small cloud and about 0.03 (W/m^2) in case of the large cloud where we have a lower metastable density. The energy transfer by metastables is in the same order as the contributions due to the kinetic energy of ions and electrons and the energy released by their recombination on the particle surface [96].

Chapter 7

Influence of dust particle size and density on metastable atom density.

As already mentioned in section (1.3), the presence of dust particles largely influences plasma parameters. Depending on the charge portion on dust particles, the plasma parameters change in a wide range. The particle charge portion in plasma depends on dust density and its size. Therefore it is worthwhile examining the respond of plasma in term of metastable density with the change of dust density and size.

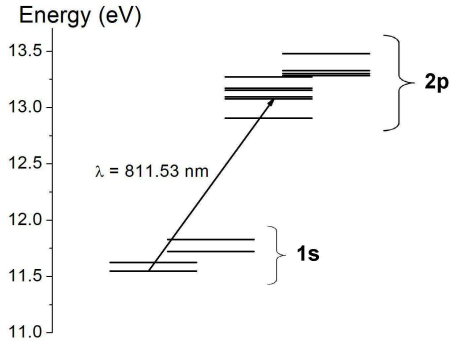

Figure 7.1: Argon term diagram of the 1s and 2p levels (in Paschen's notation). Energy values were taken from NIST data base [3].

In order to do so, argon metastables density in a dusty rf discharge with argon as working gas was measured by means of TDLAS. The experiments have been performed in the PULVA1. The nano particles were produced internally by adding a short pulse of acety-

lene to an argon plasma. Shortly after the acetylene flow was switched off the remained plasma is nothing else than an argon rf plasma containing grown dust particles. Because, all hydrocarbon species were either collected by dust particles or diffused to the pump. The drastic increase of metastable density at the acetylene pulse end implies a complete disappearance of hydrocarbon species (figure (5.11)).

Argon essentially consists of ^{40}Ar isotope (99.6%) with zero magnetic momentum, therefore, the transmitted photodiode signal can be fitted by one Doppler profile:

$$I(v) = (a + bv + cv^2) \cdot \exp\left\{-\kappa_0 l \cdot \exp\left[-\left(\frac{v - v_0}{0.6\Delta v}\right)^2\right]\right\} \tag{7.1}$$

The parameters a, b and c represent the baseline of the signal, i.e. the transmitted signal without plasma, approximated by a second-order polynomial. v_0 is the central frequency, taken as a free fit parameter.

7.1 Metastable density in pristine argon plasma and the quantitative treatment

The dependence of the argon metastable atom number density n_m on the input rf power have been obtained experimentally in a pure argon discharge (see figure (7.2)). As can be seen, the metastable density monotonically increases with power with the tendency to saturate before 50 W.

The behavior of the metastable atoms can be explained in the frame of a simple model. We use the balance equation for the metastable atoms:

$$\frac{\partial n_m(t)}{\partial t} = \sum_i G_i - \sum_j L_j \tag{7.2}$$

where G_i are the rates of different production processes, and L_j are the rates of losses. The spatial distribution of metastables is not uniform, and in our case n_m is a "line-of-sight" averaged quantity.

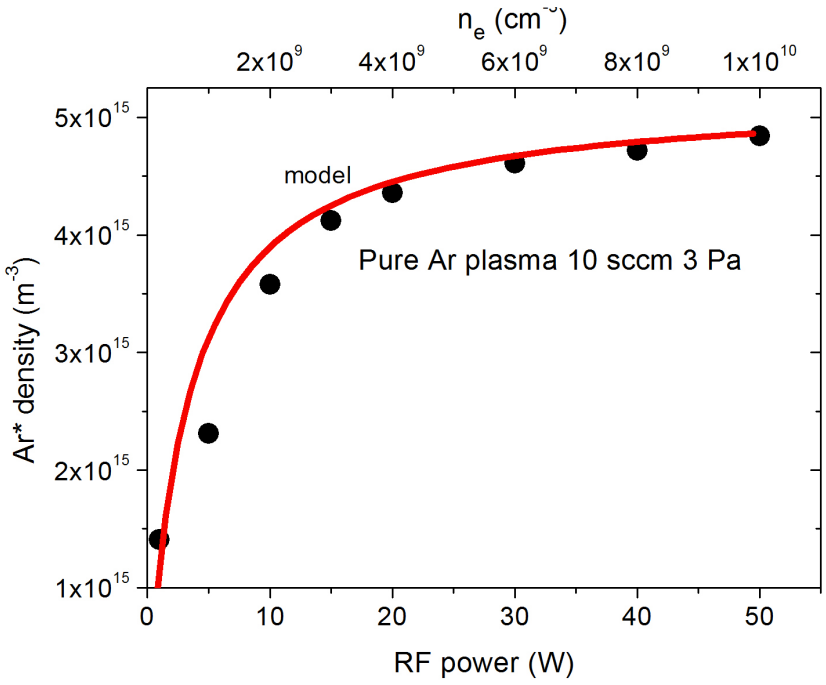

Figure 7.2: Input power dependence of metastable density in rf discharge and comparison with model.

As long as we are interested in a stationary solution ($\partial n_m/\partial t = 0$), the balance equation can be solved algebraically with respect to n_m. The production channels are independent of the density of metastables. Most of the loss rates are proportional to n_m: $L_j = n_m \cdot \nu_j$, where ν_j is the frequency of corresponding loss channel. The diffusion is also represented in this linear form. Metastable pooling, an essentially nonlinear loss channel, is negligible at our conditions. Thus the solution to equation (7.2) is given as:

$$n_m = \frac{\sum_i G_i}{\sum_j \nu_j}. \tag{7.3}$$

Among numerous channels, leading to population and depopulation of the metastable level, the radiative-collisional coupling to other excited states (for the most part to 1s- and 2p-states) is difficult to accurately take into account. For this purpose the whole system of balance equations for all excited states should be

solved. But the low-temperature, low-pressure conditions, which we have, allow us to make a simplifying assumption concerning the role of the excited states. We assume, that their densities are small and do not contribute to the population of metastables. The metastable atoms are quenched by electron impact to radiative 1s-states with a rate constant $k_{quench} = 2 \times 10^{-7}\mathrm{cm}^3\mathrm{s}^{-1}$, widely accepted in the literature [98, 99]. Collisions with electrons can also excite metastables into 2p-levels, the rate constant for this channel is estimated to be of about the same value $k^m_{exc} = 2 \times 10^{-7}\mathrm{cm}^3\mathrm{s}^{-1}$, which is consistent with the data in [98, 100].

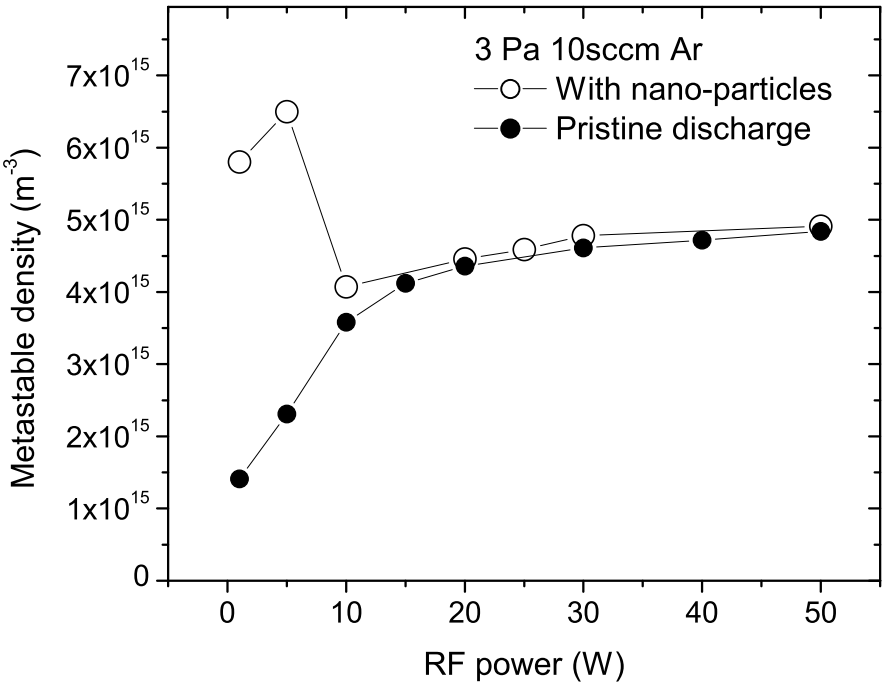

Figure 7.3: Metastable density in dusty (open circles) and pristine (filled circles) argon plasmas.

The frequency of diffusion loss (de-excitation due to collisions with walls) is accounted for by the term D_m/l^2_{eff}, where $D_m = 74.6$ cm^{2}s^{-1} [101] is the diffusion coefficient of metastable argon atoms in parent gas at 1 Torr, and Λ is the effective diffusion length.

We may drop the terms accounting for losses in two- and three-body collisions with background atoms, since they start to play role at pressures at least one order of magnitude higher [102].

The final result describing the dependence of n_m on plasma parameters is obtained as:

$$n_m = \frac{k_{exc} \cdot n_g \cdot n_e}{D_m/l_{eff}^2 + (k_{quench} + k_{exc}^m)n_e} \tag{7.4}$$

where n_g is the ground state density, n_e is the plasma density and k_{exc} is the rate coefficient for the ground state excitation into metastable level. The k_{exc} is defined as usual as a product of electron velocity and cross section, averaged over the velocity electron distribution function (EDF). We take the cross section for ground state excitation from the work [103], and make an averaging over an Maxwellian EDF. As a result, we get $k_{exc}(T_e^{eff})$ as a function of effective electron temperature T_e^{eff}.

With equation (7.4) we got a plasma density dependence of metastables. Now let us take advantage of the fact, that in low-pressure CCP discharges n_e is to a great extent proportional to input power P, while the mean electron energy does not change with power. This fact allows us to make a relation between the power and plasma density scales $n_e = k \cdot P$, with the proportionality coefficient $k = 2 \times 10^8$ cm^{-3}W^{-1} [93].

Finally, we have two fitting parameters T_e^{eff} and l_{eff} for the experimental curve. A good fit to the experimental data yield the values $T_{e0}^{eff} = 1.8\ eV$ and $l_{eff} = 3.0$ cm (see figure (7.2))

It is a well established fact in the literature, that for the low-pressure case of CCP discharge the EDF is bi-maxwellian. The majority of electrons have a temperature in the range of 0.3 – 1 eV, and 10 – 20 % are with a temperature 3 – 4 eV (see, for example [104, 105]). Thus the value of $T_{e0}^{eff} = 1.8\ eV$ appears reasonable. The value of l_{eff} is also realistic for our geometry. (In case of pure spherical or cylindrical geometry $l_{eff} = R_r/\pi$ or $l_{eff} = R_r/2.4$, where R_r is a corresponding radius).

The input power dependence of argon metastable number density can be under-

stood as follows. At low powers the diffusion loses are dominated by diffusion, and n_m rises almost linearly (with power or plasma density). Then the losses through electron collisions take over, and at higher powers n_m tends to a constant value. In between there is a transition region, where both loss channels play an equally important role.

7.2 Influence of grown dust particles on metastable density

Normally, in a void-free dust dense plasma, the metastable density is significantly higher than in pristine plasma (metastable density at plasma power lower than 10 W in figure (7.3)). However with presence of the dust void (plasma at power higher than 10 W) the plasma separated itself into 2 parts; a pristine plasma inside the void and a dusty plasma outside the dust void. The expansion of the dust void with increasing plasma power leads to a metastable density more and more closer to the value of pristine plasma (figure (7.3)).

Generally speaking, the presence of dust particles has both positive and negative effects on metastable density. On one hand, dust particles collect electrons from plasma. In order to sustain the plasma, the electron temperature has to increase. The increase of electron temperature results in an enhancement of excitation rate of metastable. On the other hand, the dust particles also act as quenching surfaces destroying metastable (see section (6.2.1)). Depending on the balance between these two effects which depend on dust size and density, the metastable density will be either higher in pristine plasma if the first effect is dominant and via versa.

Considering equation (7.4) under the influence of dust particles, the effective diffusion length has to be adjusted to include the diffusion of metastable to dust particles with the corresponding effective length l_{tot} [106];

$$\frac{1}{l_{tot}^2} = \frac{1}{l_{eff}^2} + \frac{1}{l_D^2} \tag{7.5}$$

where $l_D = 1/n_d S_d$ is the effective length for diffusion of metastable to dust particles with n_d and S_d are dust particle density and surface area, respectively.

The source term in equation (7.4) also changes due to the increase of electron effective temperature and consequently the excitation rate coefficient. Using the model in section (7.1) to fit the measured metastable density in dusty plasma giving a relatively high electron effective temperature, $T_e^{eff} \approx 25eV$. This extreme temperature suggests that other excitation channels e.g. cascade from higher levels should play a considerable role in metastable balance equation. Let's call the total rate of the cascade excitation k_{exc}^c, the metastable density in dusty plasma can be written as:

$$n_m^D = \frac{(k_{exc} + k_{exc}^c) n_g n_e}{(1/l_{eff}^2 + n_d^2 S_d^2) D_m + (k_{quench} + k_{exc}^m) n_e} \tag{7.6}$$

This equation will be used to evaluate the influence of dust particle size and density later on.

7.2.1 The influence of dust size on metastable density

As mentioned above, the dusty plasma with mono-dispersed grown particles were produced by argon rf plasma in continuous mode by adding a short pulse of acetylene. The length of C_2H_2 pulse, $\tau_{C_2H_2}$ was chosen to full filled $T_{trans} < \tau_{C_2H_2} < T_{void}$. This constrain ensures that the dust densities are the same for all chosen flow lengths. Because, after the $\alpha - \gamma$' transition, no new (or only few more) particles were created which guarantee that the total dust particle number remained. And, there was no dust void appear which means total volume occupied by dust also stays constant.

Meanwhile, longer flow length produced bigger particles. The size of particles produced by $\tau_{C_2H_2}$ acetylene flow is more or less the same as the size of dust particles in processing plasma at the time $t = \tau_{C_2H_2}$ after the acetylene flow was added. The dependence of dust size on the acetylene pulse length, therefore, can be regarded as the grow of dust particle size in precessing plasma.

By comparing the metastable density of the dusty plasmas prepared by different

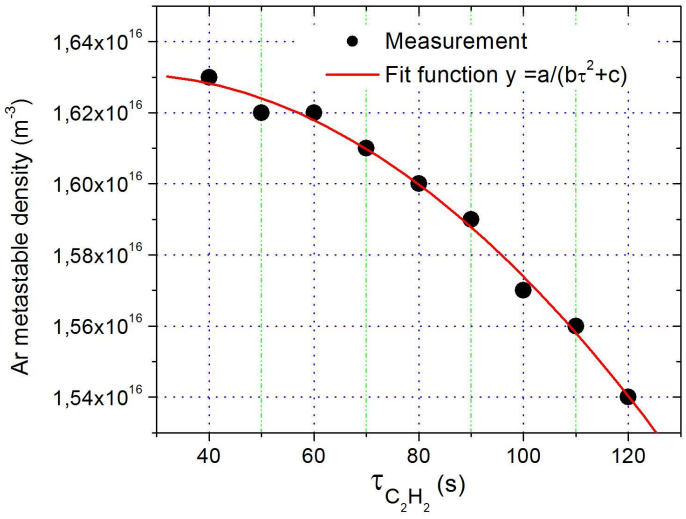

Figure 7.4: Metastable density of dusty plasma produced by different C_2H_2 pulse lengths.

acetylene flow lengths ($\tau_{C_2H_2}$) we have the relation between metastable density and dust particle size. Using equation (7.5) the relation between dust particle size and metastable density, in the case of constant dust density, can be expressed as the following:

$$n_m(\tau_{C_2H_2}) = \frac{A}{B \cdot S_d^2(\tau_{C_2H_2}) + C} \tag{7.7}$$

where $A = (k_{exc}+k_{exc}^c)n_g n_e$, $B = n_d^2 D_m$ and $C = D_m/l_{eff}^2+(k_{quench}+k_{exc}^m)n_e$. The metastable density in dusty plasma produced by different acetylene flow lengths was measured and is plotted in figure (7.4). The dependence of metastable density on acetylene flow length can be well fitted to the function $y = c_1/(c_2\tau_{C_2H_2}^2 + c_3)$. According to equation (7.7), the particle surface in hydrocarbon containing plasma after the $\alpha-\gamma$' transition is therefore proportional t. This result is also in agreement with the assumption we had made in section (5.2.2) that the product $n_d S_d$ is linear dependent on time (n_d is constant in this case). Therefore the particle radius must be proportional to square root of time:

$$r \propto t^{1/2} \tag{7.8}$$

Which also means:

$$\frac{dr}{dt} \propto t^{-1/2} \tag{7.9}$$

This particle size grow rate is a transition between ionic ($\propto t^{-2/3}$) and neutral grow (constant in time) rates [107] which suggests a combination of the two grow mechanisms in hydrocarbon containing rf plasma. The particle radius ($\propto t^{1/2}$) is also in agreement with the measurement of dust grow in argon/ silene plasma [108].

7.2.2 The influence of dust density on metastable density

It is more difficult to change the dust density of the dusty plasma generated by a processing plasma than to change the dust size. In continuous rf plasma mode, shortly after the acetylene flow was turned on, the plasma is ready to proceed to the γ' mode (figure (5.11)). The total number of dust particles does not change since then until the end of the dust generation growth.

We therefore employed pulsed rf plasma to create plasma of different dust densities. The dust density in pulsed rf plasma is determined by its dust confining ability. As can be seen in figure (7.5), after certain time the metastable density in pulsed rf plasma reach a steady state value implying that dust density in this plasma also reached equilibrium value. Consider the balance equation for dust particle:

$$\frac{\partial n_d(t)}{\partial t} = G_d - L_d \tag{7.10}$$

The density of dust confined in a pulsed plasma, beside the plasma power depends on two important parameters; the processing gas flow $\Gamma_{C_2H_2}$, and the duty cycle D. Dust generation rate G_d is obviously proportional to D and amount of processing gas density available in plasma which is determined by the C_2H_2 flow. Therefore G_d can be reasonably expressed as follow:

$$G_d = a_1 \cdot D \cdot \Gamma_{C_2H_2} \tag{7.11}$$

where a_1 is a parameter which takes into account the influence of plasma power. In this consideration, since the plasma power was fixed at 10 W, a_1 is a constant.

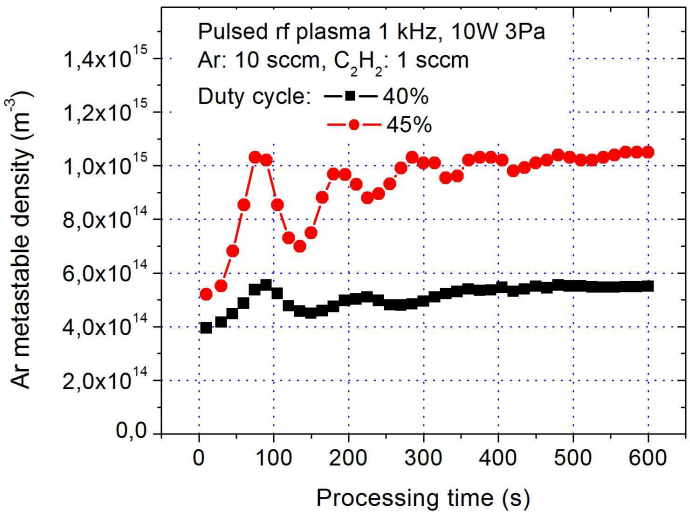

Figure 7.5: Metastable density of pulsed rf plasma at different duty cycles using Ar/ C_2H_2 gas mixture. The metastable density tends to reach a steady state value indicating an equilibrium dust density inside the plasma.

The loss rate L_d for dust particle is roughly proportional to the off time of the plasma when the particles lose their charge and some of them can escape to the chamber wall. L_d is therefore inversely proportional to the duty cycle. Meanwhile, L_d linearly depends on the dust particle density n_d since the uncharged dust is mainly driven out by diffusion in collision with background gas. L_d can thus be written as:

$$L_d = \frac{a_2 \cdot n_d}{D} \tag{7.12}$$

Similar to a_1, a_2 is also a constant with fixed plasma power. In steady state condition, the two rates are equal ($L_d = G_d$) giving the confined dust density.

Combining equations (7.11) and (7.12), we obtain the relation for the confined dust density in pulsed rf plasma:

$$n_d = \frac{a_1}{a_2}\Gamma_{C_2H_2} \cdot D^2 \tag{7.13}$$

However, interpretation of results in the case of pulsed rf discharge is not straight forward as in the continuous discharge. In order to compare measured metastable densities of plasma at different duty cycles, one has to adopt a new quantity which is the density ratio of dusty to pristine plasmas at the same duty cycle and plasma condition. This ratio is the representative of the dust population in the pulse modulated dusty plasma. The density ratio in relation with duty cycle of dusty plasma prepared by two different acetylene flows (5 sccm and 1 sccm) is expressed in figure (7.6). As already mentioned, the metastable density depends on the balance between two opposing effects associating with the presence of dust particles. The loss of metastable atom on dust particle surface is linearly proportional to the dust density. The metastable excitation rate is exponentially proportional to the electron temperature [100] which more or less quadratically depends on the charge portion on particles [33]. According to equation (7.13) with increasing duty cycle, the density of confined dust should increase quadratically. The metastable density ratio, however, should starting from unity decreases to a shallow minimum before increasing to a plateau at larger duty cycles (figure (7.6)).

The plateau appearing at large duty cycle is the consequence of the close parking effect which reduces the particle charge when particles are too close to each other. At hight particle density this effect becomes important, with increase dust density, the charge portion cannot increase any further and thus metastable density. The saturation occurs at 40 % for the case of 5 sccm flow while for 1 sccm flow this phenomenon appears at larger duty cycle (90 %) (figure (7.6)). The dust density of this two plasmas as calculated from equation (7.13) is relatively equal ($8100a_1/a_2$ for 1 sccm case at 90 % duty cycle and $8000a_1/a_2$ for 5 sccm case at 40 % duty cycle) which is a confirmation for our estimation of confined dust density in power modulated plasma.

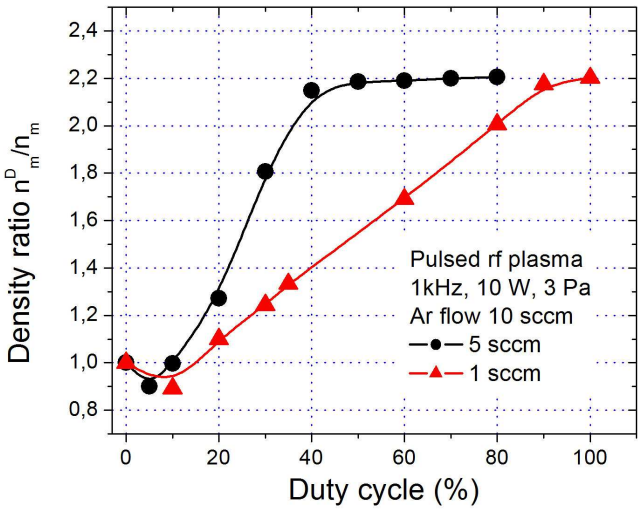

Figure 7.6: Metastable density ratio between dusty plasma and pristine plasma during the same duty cycle.

Chapter 8

Conclusion

The work done in the frame of the doctoral thesis was the investigation of dusty plasma by means of tunable diode laser spectroscopy. Special interest was focused on the interactions of dust particles and metastable atoms. The introduction to dusty plasma and the applications of fine dust particles produced or treated by plasma was brought at the beginning, see chapter (1). The tunable diode laser spectroscopy which is the main diagnostics method used to study plasma is described in section *Diagnostics* in chapter (3). The main results are summarized below.

1) Al density and temperature in dc and pulsed magnetron discharges

In order to test the possibility of TDLAS system, the diode laser absorption measurements of Al atoms produced in a dc and pulsed magnetron discharges have been performed.

The measured concentration reached 2×10^{17} m^{-3} in dc mode and was higher than 1.5×10^{18} m^{-3} in case of pulsed discharge during the active part of the pulse. Measurements with argon as working gas show an expected behavior of the measured atom density and temperature.

Decrease of absorption signal was observed in argon/oxygen and argon/methane mixtures. A small admixture of oxygen leads to a complete disappearance of the absorption signal indicating vanishing Al atom density. The effect is believed to be caused by the oxidation of the magnetron target. This decrease reveals typical hysteresis behavior caused by poisoning of the target. Significant difference

between critical oxygen flow value in dc and pulsed modes was registered.

2) Dust formation and plasma behaviors in hydrocarbon containing plasmas

The dust growing plasmas (Ar/C_2H_2, Ar/CH_4 and Ar/C_3H_6 rf plasmas) were characterized by laser transmission and scattering methods, ion energy distribution function and mass spectrum evolution by plasma processing monitor, and last but not least the spatial distribution in pristine plasma and the temporal behavior of the metastable atom density in processing plasma using TDLAS.

a) The mass spectra of investigated hydrocarbon plasmas show growth of molecules. The measured ion mass spectrum of Ar/C_2H_2 plasma is distinctly different from that of the Ar/CH_4 and Ar/C_3H_6 plasmas, indicating some difficulty to break the carbon-carbon triple bond of acetylene. Hydrocarbon molecules in acetylene plasmas, hence, prefer to grow by addition of C_2-containing molecules as the presence of hydrocarbon molecular ions with even numbers of carbon atoms is much more prominent than with odd numbers. The observed ions in Ar/C_2H_2 plasma are extremely hydrogen-poor, e.g., $C_6H_3^+$ or $C_8H_3^+$. Meanwhile in other plasmas, there is a larger chance for molecular ions to contain a larger number of hydrogen atoms e.g., $C_6H_7^+$ or $C_7H_7^+$.

b) Comparing the ion energy distributions from different gas mixtures we note that Ar/C_2H_2 produces energies up to 36 eV which is much larger than in Ar/CH_4 and Ar/C_3H_6. Obviously, the plasma potential is much higher in Ar/C_2H_2 compared to the other gas mixtures. It is believed that the growing dust particles by capture of electrons cause a higher electron temperature and thus an enhancement of the plasma potential.

c) Particle growth has been studied by recording the intensity of the transmitted and scattered laser light signal from the particle cloud. As a general trend, particle formation is more likely in Ar/C_2H_2 than in Ar/CH_4 plasma. In the argon/acetylene plasma a large amount of small carbon dust particles ($\sim$ 100 nm) is effectively and continuously created. An oscillation of the transmitted laser intensity was observed which is caused by periodic formation and expansion of a central void. This behavior can be explained by multi-generation dust cloud formation. Support for the given explanation of dust particle density oscillation

is provided by the temporal behavior of small molecular ions in plasmas.

d) The metastable density responds closely to the time evolvement of the dust growth in processing plasma. From the temporal behavior of metastable density we can identify the times T_{trans}, T_{void}, and T_p for the $\alpha - \gamma$' transition, the appearance of a the dust void and the dust particle growth period, respectively. The metastable density can be used as an indicator for changes in plasma, especially electron temperature and density as well as to trace the phase transitions in processing plasma between: nucleation, agglomeration, accretion, and dust expelling phases.

3) Plasma characterization in term of metastable density and temperature

a) The radial distribution of neon metastable atom density in capacitive coupled rf discharge can be approximated to a Gaussian profile with the width smaller than plasma chamber radius. The diffusion flow of metastable atoms deduced from their spatial density distribution gives the loss of metastable atom in the plasma sheath.

b) Argon metastable density was measured in rf plasma and compared with a simple model for metastable density. The model explains well the trend of metastable density with respect to the change of plasma input power. In order to apply this model for the case of dusty plasma, the excitation channel by cascade from higher levels has to be taken into account.

4) Interaction of metastable atom and dust particle

a) The experimental results of dusty plasma with injected SiO_2 particles trapped in plasma sheath by the confining ring (with its radius either 4 cm or 6 cm) were compared with that of pristine plasma. The quenching factor α which accounts for the interaction between dust particles and metastable atoms was estimated in the order of 0.038 for the case of small ring and the corresponding estimate dust density 4.1×10^{10} m^{-3}. In the case of the large ring with a confined higher dust density 3×10^{12} m^{-3}, the factor increases to about 0.8.

b) Particle heating by metastable atoms was strongly evidenced. The power absorbed by dust particles due to bombardment of metastable atoms onto a

dust particle surface in our experiments is about 0.04 Wm^{-2} for the low dust density case and lower for higher dust density which is in the same order as the contributions of kinetic energy of ions and electrons and the energy released by their recombination on the grain surface.

5) Influence of dust particle density and size on metastable density

The change of metastable density of dusty plasma in comparison with that of pristine plasma is the result of the balance between two effects depending on dust particle size and density. These are the loss of metastable atoms due to quenching at the dust particle surfaces and the increase of the excitation rate due to the increase of electron temperature. In a void-free dust dense plasma the metastable density is much higher in a dusty plasma than in a pristine plasma since the electron temperature in this plasma is significantly enlarged. Meanwhile at low dust density, the loss effect can outweigh the enhancement effect. The metastable density in the dusty plasma therefore is lower.

By comparing the metastable density in a dusty plasma with different dust sizes and densities produced by hydrocarbon containing plasma, one can conclude that:

(i) The dust particle radius growth rate after the $\alpha - \gamma'$ transition in hydrocarbon containing plasma is proportional to $t^{-1/2}$ which is the combination of neutral and ionic growths.

(ii) The confined dust density in pulsed processing plasma is proportional to the processing gas flow and to the square of duty cycle.

Through measuring metastable density, TDLAS therefore can be used as a tool to study the dust growth process in processing plasma.

Bibliography

[1] Tonks L, and Langmuir I, *Phys. Rev.* **33** 876 (1929).

[2] Green P G, Kinsey J L, and Field R W, *Journal of Chemical Physics* **91** 1 5160-5163 (1989).

[3] Martin W C et al.: *NIST Atomic Spectra Database* (National Institute of Standards and Technology, Gaithersburg) http://physics.nist. gov/PhysRefData/ASD/ (2005).

[4] Chen F F, *Introduction to Plasma Physics* **Plenum Press** (1974).

[5] Hippler R, *Low Temperature Plasma Physics* **Wiley-VCH** (2001).

[6] Melzer A, Goree J 2008 Fundamentals of Dusty Plasmas, In: *Low Temperature Plasmas*, Vol. 1 (R. Hippler, H. Kersten, M. Schmidt, K.H. Schoenbach, Eds.), **Wiley-VCH: Berlin**, p. 129

[7] Langmuir I, Found C G, and Dittmer A F, *Science* **60**, 392 (1924).

[8] Smith B A, Soderblom L, Batson R, Bridges P, Inge J, Masursky H, Shoemaker E, Beebe R, Boyce J, Briggs G, Bunker A, Collins S A, Hansen C J, Hunt G E, Norrison D, Owen T, Sagan C, Veverka J, Strom R, and Suomi V E, *Science* 215, 504 (1982).

[9] Hill C J, and Mendis D A, *Moon and Planets* **23**, 53 (1980).

[10] Goertz C K, and Morfill G, *Icarus* **53**, 219 (1983).

[11] Goertz C K, *Rev. Geophys.* **27** 271-292 (1989).

[12] Horanyi M, *Ann. Rev. Astron. Astrophys.* **34**, 383 (1996).

[13] Roth R M, Spears K G, Stein G D, and Wong G, *Appl. Phys. Lett.* **46**, 253 (1985).

[14] Selwyn G S, Singh J, and Bennett R S, *J. Vac. Sci. Technol.* **A7**, 2758 (1988).

[15] Kersten H, Deutsch H, E. Stoffels, W.W. Stoffels, and G.M.W. Kroesen, *Int. J. Mass Spectr.* **223**, 313 (2003).

[16] Hippler R, Kersten H 2008 Applications of Dusty Plasmas, In: *Low Temperature Plasmas*, Vol. 2 (R. Hippler, H. Kersten, M. Schmidt, K.H. Schoenbach, Eds.), **Wiley-VCH: Berlin**, p. 787

[17] Spears K G, Robinson T J, and Roth R M, *IEEE Trans. Plasma Sci* **14** 179 (1986).

[18] Gould R J and Salpeter J E, *Astrophys. J.* **138** 393-412 (1963).

[19] Whipple E C, *Rep. Prog. Phys.* **44** 1197-1250 (1981).

[20] Northrop T G, *Phys. Cripta* **45** 475-490 (1992).

[21] Garscardden A, Ganguly B N, Haaland P D, and Williams J, *Plasma Sources Sci. Technol.* **3** 239-245 (1994).

[22] Harnes O, Nitter T, Tsytovich V, Morfill G E, and Hartquist T, *Plasma Sources Sci. Technol.* **3** 448-457 (1994).

[23] Goree J, *Plasma Sources Sci. Technol.* A**10** 3540-3544 (1994).

[24] Boufendi L, and Bouchoule A, *Plasma Scources Sci. Technol.* **3** 262-267 (1994).

[25] Garrity M P, Peterson T W, Garrett L M, and O'Hanlon J F 1995 *J. Vac. Sci. Technol.* **A13** 2939 –2944

[26] Barnes M S, Keller J H, Forster J C, O'niel J A, and Coultas D K, *Phys. Rev. Lett.* **68** 313-316 (1992).

[27] Melzer A, Schweigert A V, and Piel A, Phys. *Scripta.*, **61**, 495 (2000).

[28] Vladimirov S V, and Nambu M, *Phys. Rev.* E**52** R2172-R2174 (1995).

[29] Vladimirov S V, Shevchenko P V, and Cramer N F, *Phys. Rev.* E**56** R74-R76 (1997).

[30] Liebermann M A, and Lichtengerg A J *Principles of Plasma Discharges and Materials Processing* **John Wiley, New York** (1994).

[31] Allen J E, *Plasma Phys. Control. Fusion* **27** 1343-1357 (1985).

[32] Riemann K U, *J. Phys. D: Appl. Phys.* **24** 493-518 (1991).

[33] Hori Y, Ostrikow K, Toyoda H, and Sugai H, *Proceed. XXV Intern. Conf. on Phenomena in Ionized Gases, Nagoya, Japan, July 17-22 2001*, v.**3**, p. 25-26 (2001).

[34] Takai M, Nishimoto T, Kondo M, and Matsuda A, *Appl. Phys. Lett.* **77** 2828-2830 (2000).

[35] Fridman A A, Boufendi L, Hbid T, Potapkin B V and Bouchoule A, *Appl. Phys.* **79** 1303-1314 (1996).

[36] Do H T, Thieme G, Fröhlich M, Kersten H, and Hippler R *Contrib. Plasma Phys.* **45 No.5-6** 1-8 (2005).

[37] Bouchoule A, *Phys. World* **6** 47 (1993).

[38] Stoffels E, Kersten H, Swinkels G H P M, and Kroesen G M W, *Phys. Scripta* **T89**, 168 (2001).

[39] Veprek S, *J. Vac, Sci. Technol.* **A17**, 2401-2420 (1999).

[40] Kogelshatz U, Eliasson B, and Egli W, *Pure Appl. Chem.* **71** 1819-1828 (1999).

[41] Kruis F E, Fissan H, and Peled A, *J. Aerosol Sci.* **29**, 511-535 (1998).

[42] Roco M C, Williams S, and Alivisatos P (Eds.), *Nanotechnology research directions: vision for nanotechnology research and development in the next decade*, **Kluwer Academic, Amsterdam.** (1999).

[43] Kersten H, Schmetz P, and Kroesen G M W, *Surf. Coat. Technol.* **108-109**, 507-512 (1998).

[44] Kersten H, Wiese R, Thieme G, Frölich M, Kopitov, Bojic D, Scholze F, Neumann H, Quaas M, Wulff H, and Hippler R, *New. J. Phys.* **5**, 93.1-93.15 (2003).

[45] Thieme G, Quaas M, Kersten H, Wulff H, and Hippler R, *3rd Intern, Conf. Physics of Dusty Plasmas (ICPDP-2002), Durban, Sourth Africa, 20-24 May 2002*, p.33 (2002).

[46] Uchida G, Iizuka S, and Sato N, *IEEE Trans. Plasma Sci.* **29** 274-278 (2001).

[47] Stoffels E, Stoffels W W, Ceccone G, Hasnaoui R, Keune H, Wahl G, and Rossi F, *J. Appl. Phys.* **86** 3442 (1999).

[48] Kersten H, Deutsch H, Stoffels E, Kroesen G M W, Hippler R, *Contrib. Plasma Phys.* **41**, 598-609 (2001).

[49] Boufendi L, and Bouchoule A, *Plasma Sources Sci. Technol.* **11** A211-A218 (2002).

[50] Wieman C E, and Hollberg L, *Rev. Sci. Instrum.* **62** 1.

[51] Franke S, *Dissertation*, **Universität Greifswald** (2001).

[52] Alferov Zh I, Andreev V M, Garbuzov D Z, Zhilyaev Yu V, Morozov E P, Portnoi E L, and Trofim V G, *Fiz. Tekh. Poluprovodn.* **4**, 1826 (1970).

[53] Kobayashi K, and Mito I, *IEEE J. Lightwave Technol.* **6** 1623-1633 (1988).

[54] Kogelnik H, and Shank C V, *Appl. Phys. Lett.* **18** 152-4 (1971).

[55] Meschede D, *Optics, Light and Laser*, **Wiley-VCH Verlag GmbH & Co. KGaA, Weinheim** (2007).

[56] Matyash K, Fröhlich M, Kersten H, Thieme G, Schneider R, Hannemann M, and Hippler R, *J. Phys. D: Appl. Phys.* **37** 2703 (2004).

[57] Kersten H, Thieme G, Fröhlich M, Bojic D, Tung D H, Quaas M, Wulff H, and Hippler R, *Pure Appl. Chem.* **77** 415-428 (2005).

[58] Ellmer V 2008, In: *Low Temperature Plasmas*, Vol. 2 (R. Hippler, H. Kersten, M. Schmidt, K.H. Schoenbach, Eds.), Wiley-VCH: Berlin, p. 675

[59] Kashtanov P V, Smirnov B M, Hippler R, *Magnetron plasma and nanotechnology Physics Uspekhi* **50**, 455-488 (2007)

[60] Kvasnica S, Adamek P, and Spatenka P, *IEEE Transaction on Plasma Science.* **33(2)** 364 (2005).

[61] Wendt A E, Lieberman M A, Meuth H, *J. Vac. Sci. Technol* **A6(3)** 1827 (1988).

[62] Bradley J W, *Plasma Sources. Sci. Technol.* **5** 622 (1996).

[63] Jonkers J, Bakker M, and van der Mullen J A M, *J. Phys. D: Appl. Phys.* **30** 1928 - 1933 (1997).

[64] Scheibner H, Franke St, Soleyman S, Behnke J F, Wilke C and Dinklage A, *Rev. Sci. Instrum.* **73** 378 (2002).

[65] Toptica Photonics AG: *DL 100 Diode Laser Manuel*, (2002).

[66] Wolter M, Do H T, Steffen H, and Hippler H, *J. Phys. D: Appl. Phys.* **38** 2390-2395 (2005).

[67] Hippler R, Steffen H, Quaas M, Röwf T, Tun T M, and Wulff H, *Advances in Solid State Physics* vol **44**, ed B Kramer (Heidelberg: Springer) p 299 and references therein (2004).

[68] Quaas M, Steffen H, Hippler R, and Wulff H, *Surf. Sci.* **454-456** 7905 (2000).

[69] Demtröder W, *Laserspektroskopie* **Berlin: Springer** (2000).

[70] Röpcke J, Davies P B, Käning M, and Lavrov B F, In: *Low Temperature Plasma Physics* ed. R Hippler **Berlin: Wiley-VCH** p 173 (2001).

[71] Wang W, Fejer, M M, Hammond, R H, Beasley M R, Ahn C H, Bortz M L and Day T, *Appl. Phys. Lett.* **68** 729 (1996).

[72] Niemax K, Zybin A, Schnürer-Patschan C, and Groll H, *Anal. Chem.* **68** 351A (1996).

[73] Niemax K, Zybin A and Eger D, *Anal. Chem.* **73** 134A (2001).

[74] Zybin A, Koch J, Wizemann H D, Franzke J, and Niemax K *Spectrochim. Acta* B **60** 1 (2005).

[75] Martin W C et. al., *NIST Atomic Spectra Database (version 2.0)* **National Institute of Standards and Technology, Gaithersburg, MD** *http://physics.nist.gov/asd* (1999).

[76] Franke S, Dinklage A, and Wilke C, *Rev. Sci. Instrum.* **72** 2048 (2000).

[77] Olejnicek J, Do H T, Hubicka Z, and Hippler R, *13th Int. Conf. Technical Computing*, **Prague 2005**, p95 (2005).

[78] MATLAB, *Users guide* **MathWorks, Inc., Natick, MA** (2000).

[79] Hippler R, Fundamental processes in plasmasurface interactions *Low Temperature Plasma Physics* ed. R Hippler *et al* **Berlin: Wiley-VCH** p79 and references therein (2001).

[80] Ziegler J F, Biersack J P, and Littmark U, *The Stopping and Range of Ions in Solids* **New York: Pergamon** (2003).

[81] Pearse R W B, and Gaydon A G, *The Identification of Molecular Spectra* **Whitefriars Press, London** (1963).

[82] Depla D, and De Gryse R, *Plasma Sources Sci. Technol.* **10** 547 and references therein (2001).

[83] Tucek J C, Walton S G, and Champion R L, *Phys. Rev. B* **53** 14127 (1996).

[84] Olthoff J K, Van Brunt R J, Radovanov S B, Flees J A, and Surowiec R, *J. AppL Phys.* **75**(1) 115 – 125 (1994)

[85] Zeuner M, Neumann H, and Meichsner, *J, J. Appl. Phys.* **81**(7) 2985 – 2994 (1997)

[86] Pullins S H, Dressler R A, Torrents R, Gerlich D, *Z. Phys. Chem.* **214** 1279 (2000).

[87] Boufendi L, Bouchoule A, and Hbid T, *J. Vac. Sci. Technol.* **A14** 572 (1996).

[88] Hong S, Berndt J, and Winter J, *Plasma Sources Sci. Technol.* **12** 46 (2003).

[89] Stoykov S, Eggs C, and Kortshagen U, *J. Phys. D: Appl. Phys.* **35** 2160 (2001).

[90] Riccardi C, Barni R, Fontanesi M, and Tosi P, *Czech. J. Phys.* 50/S3 (2000).

[91] Daugherty J E, and Graves D B, *J. Vac. Sci. Technol.* **A11** 1126 (1993).

[92] Vladimirov S V, Ostrikov K, and Samarian A A, *Physics and Applications of Complex Plasmas* **London: Imperial College Press** (2005).

[93] Kersten H, Stoffels E, Stoffels W W, Otte M, Csambal C, Deutsch H, and Hippler R, *J.Appl.Phys.* **87** 3637–3645 (2000).

[94] Tatanova M, Thieme G, Basner R, Hannemann M, Golubovskii Yu B, and Kersten H, *Plasma Sources Sci. Technol.* **15**, 507 (2006).

[95] Denysenko I, Berndt J, Kovacevic E, Stefanovic I, Selenin V, and Winter J, *J. Phys. Plasmas* **13** 073507 (2006).

[96] Swinkels G H P M, Kersten H, Deutsch H, Kroesen G M W, *J. Appl. Phys.* **88** 1747 (2000).

[97] Piejak R, Godyak V, Alexandrovich B, and Tishchenko N, *Plasma Sources Sci. Technol.* **7** 590 (1998).

[98] Czerwiec T, and Graves D B, *J.Phys.D: Appl.Phys.* **37** 2827-40 (2004).

[99] McMillin B K, and Zachariah M R, *J.Appl.Phys.* **77** 5538-5544 (1995).

[100] Baisova B T, Strunin V I, Strunina N N, and Khudaibergenov G Zh, *Tech. Phys.* **48** 969-71 (2003).

[101] Bogaerts A, Gijbels R, and Vlcek J, *J.Appl.Phys.* **84** 121-36 (1998).

[102] Tachibana K, *Phys. Rev. A* **34** 1007-15 (1986).

[103] Yanguas-Gil A, Cotrino J, and Alves L L, *J.Phys.D: Appl.Phys.* **38** 1588-1598 (2005).

[104] Turner M M, Doyle R A ,and Hopkins M B, *Appl Phys. Lett.* **62** 3247-49 (1993).

[105] Brzobohaý O, and Trunec D, *Proc. WDS'05 Part II* 306-12 (2005).

[106] Do H T, Kersten H, and Hippler R, *New Journal of Physics* **10** 053010 (2008).

[107] Haaland P, Garscadden A, and Ganguly B, *Appl Phys. Lett.* **69** 904-907 (1996).

[108] Dorier J L, Hollenstein Ch, and Howling A A, *J. Vac. Sci. Technol. A* **13** 918-926 (1994).

ACKNOWLEDGEMENTS

First and foremost, I would like to express my sincere gratitude to my supervisor Prof. Dr. R. Hippler for offering me the possibility to follow my interests in plasma physics. I thank him also for his questions, discussions, for his continuous guidance and valuable support during this study and for allowing a wide autonomy and responsibility. Thanks for everything you have done for me.

I also thank Prof. Dr. H. Kersten for his constant support, energy and numerous discussions. Thank you very much for your excellent suggestions, helpful advices and invaluable comments.

Many thanks to Dr. H. Testrich and Dr. M. Wolter for their supports in tunable diode laser spectroscopy.

I thank Dr. V. Vartolomei for his help, discussions and comments on this work.

I would like to thank all members of my working group Plasma-Wall Interactions: H. Bold, Dr. F. Herrmann, S. Ibrahimkutty, A. Knuth, D. Köpp, J. Kredl, A. Majumdar, Dr. H. Steffen, G. Thieme, R. Wiese, M. Wolter, and S. Wrehde for their helps and the friendly working atmosphere.

Next I would like to thank Dr. Z. Hubicka and his collaborators: Dr. P. Adamek, Dr. M. Cada, S. Kment, Dr. J Olejnicek, and P. Virostko (Institute of Physics, Academy of Sciences of the Czech Republic). It is a great opportunity to work with you.

I gratefully acknowledges the receipt of an International Max-Plank Research School for "Bounded Plasmas" granted by the German State of Mecklendburg-Vorpommern.

I am very grateful for the 3-year-financial support from Ministry of Education and Training of Vietnam (MOET) as well as all members of 322 project enabled me to do this Ph.D. work. I am also highly appreciated the organization for my Ph.D. work of Joint Graduate Education Program between Institute of Physics, Vietnam Academy of Science and Technology and University of Greifswald, especially Prof. Dr. Le Tran Binh, Prof. Dr. Nguyen Ai Viet, Ass. Prof. Dr. Le Thi Lai, Dr.

Luu Lan Huong, PD Dr. Jörn Kasbohm and other organizers of this program.

Finally, I express my heartfelt thanks to my family. To my wife An, who is always beside me every step of the way, for her love, her patience and care, for sharing thoughts with me and for helping me keep my life in proper perspective and balance.

Hoang Tung Do

Ernst Moritz Arndt University Greifswald
Faculty of Mathematic and Natural Science
Institute for Physics — Email: do@physik.uni-greifswald.de
Felix-Hausdorff-Str. 6, 17489 Greifswald — Phone: (+49) 3834-4784 (office)

RESEARCH INTERESTS

Growth and dynamics of dust particles in processing plasmas using plasma process monitor and advanced spectroscopic techniques

EMPLOYMENT

Graduate Research Assistant **03/08/2003–present**
Institute for Physics
Ernst Moritz Arndt University Greifswald
Supervisor: Prof. Dr. Rainer Hippler

Graduate Research Assistant **09/01/2001-02/28/2003**
Institute of Physics
Vietnam Academy of Science and Technology
Supervisor: Prof. Dr. Nguyen Ai Viet

EDUCATION

Ph.D. Physics, Institute for Physics **03/08/2003–present**
Ernst Moritz Arndt University Greifswald
Thesis Title: "Tunable Diode Laser Absorption Spectroscopy of Dusty Plasmas"
Thesis Advisors: Prof. Dr. Rainer Hippler

Diploma Equivalent **10/2001–10/2002**
Joint Graduate Educational Program held by Hanoi University of Science, Institute of Physics, Vietnam and University of Greifswald, Germany

B.Sc. Physics, Faculty of Physics **09/10/1997–06/20/2001**
Hanoi National University, Vietnam
Thesis Title: "Influence of laser radiation on the absorption coefficient of acoustic and optical phonons of quantum wires"
Thesis Advisors: Prof. Dr. Nguyen Quang Bau

List of publications related to this thesis

Presentations

[1A] H.T. Do and R. Hippler, "Tunable Diode Laser Absorption Spectroscopy of Metastable Atoms in Dusty Plasmas", *Poster*, 5^{th} International Conference on the Physics of Dusty Plasma, Azores (Portugal) **2008**

[2A] H.T. Do and R. Hippler, "Study of powder formation in pulsed and continuous rf processing plasmas using TDLAS", *Poster*, DPG Frühjahrstagung, Darmstadt **2008**

[3A] H.T. Do and R. Hippler, Tagung der DGaO, "Diode Laser Absorption Spectroscopy of Complex Plasmas", *Oral Presentation*, Tagung der DGaO, Heringsdorf **2007**

[4A] H.T. Do and R. Hippler, "Investigation of dusty plasma by means of tunable diode laser absorption spectroscopy", *Oral Presentation*, International Max Planck Research School on Bounded Plasmas, 09 May 2006

[5A] H.T. Do and R. Hippler, "Influence of dust particles on density of neon metastable", *Oral Presentation*, International Max Planck Research School on Bounded Plasmas, Greifswald **2006**

[6A] H.T. Do, G. Thieme and R. Hippler, "Energy Distribution of Ion Species in Ar/CH_4 and Ar/C_2H_2 Radio-frequency Plasmas", *Poster*, 4^{th} International Conference on the Physics of Dusty Plasma, Orleans (France), 13-17 **2005**

[7A] H.T. Do and R. Hippler, "Ion molecule formation and dust formation in hydrocarbon containing plasmas", *Oral Presentation*, International Max Planck Research School on Bounded Plasmas, Greifswald **2005**

[8A] H.T. Do and R. Hippler, "Dust particles formation in plasma process", *Oral Presentation*, International Max Planck Research School on Bounded Plasmas, Greifswald **2004**

[9A] H.T. Do, H. Kersten, "Particle formation in process plasmas", *Oral Presentation*, XI. Erfahrungsaustausch Oberflächentechnologie mit Plasmaprozessen, Mühlleithen, **2004**

Publications

[1B] H.T. Do, V. Sushkov, and R. Hippler, *Tunable diode laser absorption spectroscopy of argon metastable atoms in Ar/C_2H_2 dusty plasmas*, New Journal of Physics, Submitted.

[2B] H.T. Do, H. Kersten, and R. Hippler, *Interaction of metastable atom with injected dust particles in radio frequency discharge*, New Journal of Physics, **10**, 053010 (2008).

[3B] H.T. Do and R. Hippler, *Tunable Diode Laser Absorption Spectroscopy of Metastable Atoms in Dusty Plasmas*, AIP Conf. Proc., **1041**, pp. 225-226 (2008)

[4B] J. Olerjnicek, H.T Do, Z. Hubicka, R. Hippler and L. Jastrabik, *Blue Diode Laser Absorption Spectroscopy of Pulsed Magnetron Discharge*, Japanese Journal of Applied Physics, **45**, No. 10B, (2006)

[5B] H.T. Do, G. Thieme, and R. Hippler, *Energy distribution of ion species in Ar/CH_4, Ar/C_2H_2, and Ar/C_3H_6 radio-frequency plasmas* AIP Conf. Proc., **799**, pp. 375 – 378 (2005)

[6B] H.T. Do, G. Thieme, M. Fröhlich, H. Kersten, and R. Hippler, *Ion Molecule and Dust Particle Formation in Ar/CH_4, Ar/C_2H_2 and Ar/C_3H_6 Radio-frequency Plasmas*, Contrib. Plasma Phys., **45**, No. 5 – 6, 378 - 384 (2005)

[7B] M. Wolter, H.T. Do, H. Steffen and R. Hippler, *Aluminium atom density and temperature in a dc magnetron discharge determined by means of blue diode laser absorption spectroscopy*, J. Phys. D: Appl. Phys., **38** 2390 – 2395 (2005)

[8B] H. Kersten, G. Thieme, M. Fröhlich, D. Bojic, H. T. Do, M. Quaas, H. Wulff, and R. Hippler, *Complex (dusty) plasmas: Examples for applications and observation of magnetron induced phenomena*, Pure Appl. Chem., **77**, No. 2, 415 – 428 (2005)

Erklärung

Hiermit erkläre ich, dass diese Arbeit bisher von mir wieder an der Mathematisch- Naturwissenschaftlichen Fakultät der Ernst-Moritz-Arndt-Universitt Greifswald noch einer anderen wissenschaftlichen Einrichtung zum Zwecke der Promotion eingereicht wurde.

Ferner erkläre ich, dass ich diese Arbeit selbständig verfasst und keine anderen als die darin angegebenen Hilfsmittel benutzt habe.